Performance analysis of low jitter high-speed photonic analog-to-digital converters in silicon photonics

vorgelegt von
Herrn Edgar Krune, M.Sc.
geb. in Sauralowka / Kasachstan

Von der Fakultät IV - Elektrotechnik und Informatik - der
Technischen Universität Berlin
zur Erlangung des akademischen Grades
Doktor der Ingenieurwissenschaften
- Dr.-Ing.-
genehmigte Dissertation

Promotionsausschuss:

Vorsitzender:	Prof. Dr.-Ing. Stephan Völker
Gutachter:	Prof. Dr.-Ing. Klaus Petermann
Gutachter:	Prof. Dr. Franz X. Kärtner
Gutachter:	Dr.-Ing. Lars Zimmermann
Tag der wissenschaftlichen Aussprache:	04.09.2017

Berlin 2017

I would like to thank my elementary school teacher Mrs. E. Lutter. Only thanks to her strong commitment I was accepted at the gymnasium although my grades were not good enough, since I had only been in Germany for one and a half years and had just learned the language. Without her encouragement, I would not have trod the educational path which led to this thesis.

Abstract

The performance of electronic analog-to-digital converters (ADCs) is mainly limited by the sampling instant precision if high-frequency signals are sampled. Its uncertainty is called timing jitter. The electrical clock generation and its distribution on chip are limited to a jitter of $\sim$ 100 fs and no significant improvement was achieved in the last decade. Physical restrictions prevent its further decrease. But mode-locked lasers can provide optical pulse trains with orders of magnitude higher timing precision. This is exploited by photonic ADCs where the sampling instants are defined by an ultra-low jitter optical pulse train.
During the last three decades, silicon photonics has evolved to a CMOS compatible platform which enables the integration of optics and electronics on the same chip. This thesis addresses such photonic integrated ADCs in silicon photonics. Possible architectures are discussed and two principle sampling instants are identified, namely, the rising edge of the induced electrical pulses and the center of mass of the optical or the detected pulses. A quantum noise model is introduced enabling the performance analysis of both sampler types. It is shown that rising edge samplers can achieve jitter values down to $\sim$ 10 fs. Center of mass samplers can achieve even $\sim$ 1 fs jitter but the ADC resolution is limited by pulse-to-pulse energy fluctuations to $<$ 9 effective number of bits. It is shown that optical clock distribution networks induce only a small skew of $<$ 100 fs for delay lines up to 75 ps but its temperature dependence still necessitates its compensation. A rising edge triggered opto-electronic clock converter is shown which achieves a fundamental jitter limit of only 10 fs, confirming the superior characteristics of photonic ADCs.

Keywords: Analog-to-Digital Converter, Silicon Photonics, Jitter, Skew, Optical Clock Distribution

Zusammenfassung

Die Performance elektronischer Analog-Digital-Umwandler (ADU) hängt vor allem von der zeitlichen Präzession des Abtastzeitpunktes ab, wenn hohe Frequenzen abgetastet werden. Dessen Unsicherheit wird als zeitlicher Jitter bezeichent. Die elektrische Taktgenerierung und dessen Verteilung auf dem Chip ist beschränkt zu einem Jitter von $\sim 100\,\mathrm{fs}$ und eine Verbesserung ist in der letzten Dekade nicht erreicht worden. Physikalische Grenzen verhindern dessen weitere Reduktion. Jedoch können modengekoppelte Laser optische Impulszüge mit einer um Größenordnungen höheren Präzession liefern. Dies wird in photonischen ADU ausgenutzt, wo die Abtastzeitpunkte durch optische Impulszüge mit ultra-geringen Jitter definiert werden.

In den letzten drei Dekaden hat sich die Silizium-Photonik zu einer CMOS-kompatiblen Plattform entwickelt, die die Integration von Optik und Elektronik auf demselben Chip ermöglicht. Diese Dissertation untersucht derartige photonisch integrierte ADU in Silizium-Photonik. Mögliche Architekturen werden diskutiert und zwei prinzipielle Abtastzeitpunkte werden identifiziert. Diese sind die Anstiegsflanke der induzierten elektrischen Impulse sowie der Schwerpunkt der optischen oder der detektierten Impulse. Ein Quantenrauschmodel wird vorgestellt, welches die Performanceanalyse beider Samplerarten ermöglicht. Es wird gezeigt, dass Sampler, die durch Anstiegsflanken getriggert werden, einen Jitter bis zu $\sim 10\,\mathrm{fs}$ erreichen können. Schwerpunkt-Sampler können sogar $\sim 1\,\mathrm{fs}$ Jitter erreichen. In diesem Fall beschränken die Impuls-zu-Impuls-Energiefluktuationen die ADU-Auflösung jedoch zu < 9 effektiven Anzahl an Bits. Es wird gezeigt, dass optische Taktverteilungsnetzwerke nur einen geringen Skew von $< 100\,\mathrm{fs}$ verursachen für Verzögerungen bis zu $75\,\mathrm{ps}$. Jedoch erfordert dessen Temperaturabhängigkeit immer noch deren Kompensation. Ein durch die Anstiegsflanke getriggerter opto-elektronischer Taktwandler wird gezeigt, der eine fundamentale Jittergrenze von nur $10\,\mathrm{fs}$ aufweist und dadurch die überlegene Charakteristik photonischer ADU bestätigt.

Schlagwörter: Analog-Digital-Umwandler, Silizium-Photonik, Jitter, Skew, Optische Taktverteilung

Contents

Chapter 1

Introduction

The first transistor, built on germanium by William Shockley, John Bardeen and Walter Brattain at the Bell Labs in 1947, became the kick-off for a technology which affected the history of human kind in an unprecedented speed and scale. The inventions of the semiconductor planar process by Jean A. Hoerni [1] and of the integrated circuits (ICs) parallel by Robert N. Noyce [2] and Jack Kilby [3] filed for patent in 1959 enabled a fast evolution of silicon-based integrated electronic circuits. The integration of transistor-based logic on a single chip replaced the vacuum tubes technology and led to digital signal processing in computers. Here, a unique clock signal distributed over the silicon chip corresponds to a conductor in the synchronously switching orchestra of an enormous amount of transistors. The miniaturization-based trend of faster and more powerful electronics became famous as Moore's law. Based on his observation that the number of transistors in ICs was doubling approximately every two years, Gordon E. Moore published his projection for the future in 1965 [4]. This prediction became impressively accurate in the following decades. The most important technology for IC implementation became the complementary metal-oxide-semiconductor (CMOS) technology introduced by Frank Wanlass in 1963 [5]. The more and more dense very-large-scale-integration (VLSI) circuits working at higher switching frequencies led to high requirements for the clock signal and forced IC designers to face new challenges.

In the ideal case, a unique clock signal is switching between two voltage levels corresponding to the ON and OFF state of a logic device. The relation between the time period of the ON state to the clock period is called *duty cycle*. A square wave signal has a duty cycle of $50\,\%$. Providing this clock signal from a single position to all destinations on chip leads to a hierarchical splitting of electrical wires into multiple versions to support all logic devices. The amount of clock destinations seen from a source is called *fan-out*. To induce a switching process in a CMOS circuit, a threshold voltage at the gate of a transistor has to

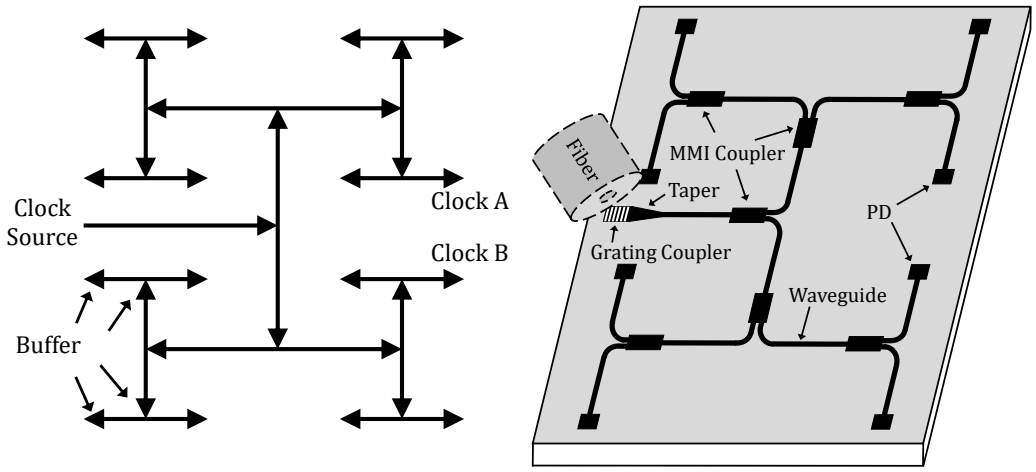

(a) (b)

Figure 1.1: CDN in H-tree based architecture: (a) An electrical clock signal from a single source is distributed by a symmetrical CDN across the die to 16 receivers. Buffers placed in front of the split wires serve for signal regeneration and to drive the fan-out. (b) An optical pulse train is distributed by waveguides across the die to synchronously clock eight electrical sub-circuits. The pulse train is coupled out of a fiber into a waveguide by a grating and an adiabatic taper. Multimode interference (MMI) couplers serve as power dividers. Photodetectors (PDs) convert the signal into an electrical pulse train.

be exceeded. In reality, the provided current and the gate capacity define a charging process and the higher the capacity or the smaller the provided current, the longer takes the charging time. Therefore, the huge amount of clock receivers requires numerous repeatedly inserted devices to drive these sinks. These are called *buffer* or *repeater* and can be realized by inverters. Starting with one clock source and ending up with a huge amount of sinks requires a clock distribution network (CDN) with several hierarchical levels. Numerous buffer stages are necessary for signal regeneration and to provide enough current for the fan-out to minimize the propagation delay [6]. These are placed where the load capacities are too high, such as in front of branches or within long wires.

CDNs are typically based on tree, spine or grid topologies or their hybrids [7]. In fig. 1.1(a) an H-tree based architecture is shown providing a global clock signal to 16 destinations symmetrically distributed across the die. Buffers are indicated as triangles. The CDN evolution is highly associated with timing uncertainty of the clock distribution. One basic performance characteristic is the *skew*. It corresponds to a static deviation of the clock arrival times between two CDN leaves. Such delay differences are indicated in fig. 1.2 for four CDN branches. It can be induced by unsymmetrical CDNs [6, 8]. Fabrication tolerances are responsible for wire dimension deviations and performance variations of each active component of the buffer stages or the sinks [6, 8, 9]. In the CDN design process, skew

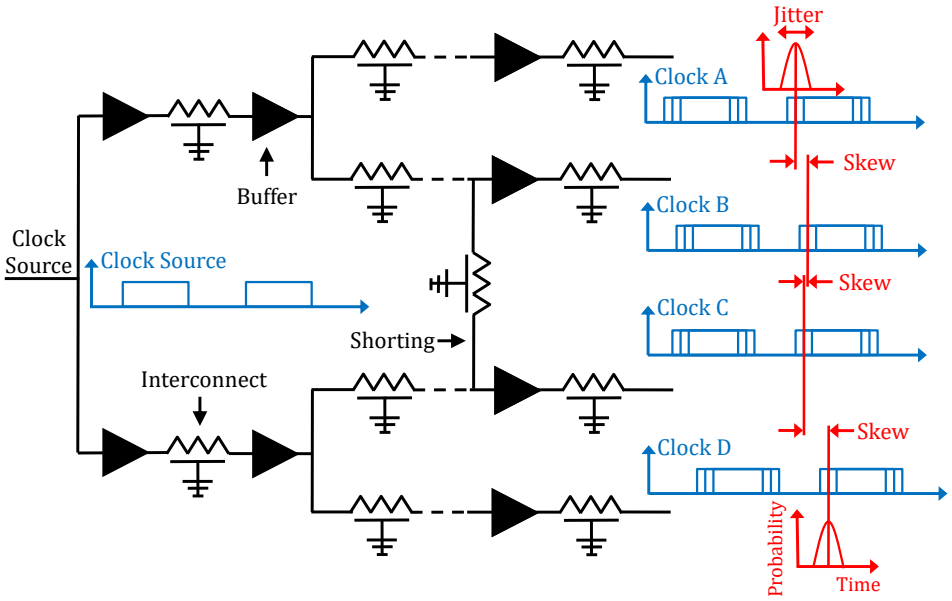

Figure 1.2: A clock signal is distributed to four destinations by different CDN branches. Buffer and interconnects induce a timing uncertainty of the clock arrival times. The static deviations between clocks A-D correspond to skew. Dynamic variations indicated by a probability distribution correspond to the jitter. Shorting at identical CDN hierarchy levels decreases the skew.

can be minimized by symmetrical delay lines. Delay variations due to fabrication tolerances can be decreased by shorting the clock paths at the clock buffers of identical CDN hierarchy levels [7, 10]. This is indicated in fig. 1.2. Periodic shorting of delay lines leads from a tree to a grid-based topology mitigating the skew [7, 10, 11, 12]. In addition, a variety of active skew compensation techniques have been introduced such as active clock deskewing systems, in-path clock correction with clock retimers and detailed design time clock buffer tuning [6, 7, 8, 9, 11]. It increased the design complexity of electrical CDNs.

Another basic performance characteristic is the *timing jitter*. It corresponds to the dynamic variation of the clock arrival times at a CDN leaf. In fig. 1.2, it is indicated by a probability distribution of the rising edge arrival times at the CDN leaves. Jitter results from temperature fluctuations across the die, crosstalk from nearby wires, noise-induced shifts in the voltage-controlled oscillator (VCO) operating frequency of the on-chip phase-locked loop (PLL), modulation of clock buffer delays due to power supply noise generated by random digital switching activities across the die and the number of buffer stages between the global clock source and the sinks [6, 7, 8, 9, 10, 11, 12, 13]. As the clock frequency and the number of repeaters increased, jitter became the dominant speed limit [8]. To avoid IC malfunctions, a timing margin is added to the clock period for the timing uncertainty degrading the performance. As a rough value, the fraction should not exceed $10\,\%$ of the clock period [7, 8, 9]. Furthermore, the power dissipation became an important issue for

microprocessors, especially for grid-based CDN topologies [6, 7, 11, 12]. The high amount of switched elements densely integrated on a die corresponds to a high capacity which is switched with the clock frequency between two voltage states. This represents directly the dissipated power which can be in the order of $50\,\%$ of the overall on-chip dissipated power [7, 11]. Hence, the goal of the CDN design is to enable the maximum operating frequency for a given IC by minimizing impacts of skew, jitter and dissipated power [8, 9, 11].
The microprocessor clock frequency increased from $108\,\mathrm{kHz}$ in 1971 to over $3\,\mathrm{GHz}$ in 2002 [9, 14]. At the beginning of this century, long-term prediction for the trend of technology scaling assumed an on-chip-local-clock frequency of $28.7\,\mathrm{GHz}$ for 2016 according to the international technology roadmap for semiconductor (ITRS) from 2001 [15]! An analysis of clock distribution systems showed that the high requirements on skew, jitter and power dissipation could not be provided by conventional electrical CDNs anymore [6, 9]. Moreover, the skin effect increases the effective wire resistance for higher switching frequencies and further deteriorates the CDN performance [8]. The number of repeaters required between the clock source and each CDN leaf increased to accommodate the rising clock speed [8]. CMOS scaling to the nanometer regime made long global wires an important design constraint [11]. These challenges forced researchers to look for alternative ways of clock distribution such as off-chip interconnection, package-level distribution, wireless microwave distribution, asynchronous distribution, distributed oscillator array networks [13], injection-locked oscillators as the local clock regenerators [13] and optical clock distribution [9, 11].
At first optical clock distribution was suggested by Joseph W. Goodman already in 1984 [16]. The emergence of mode-locked lasers (MLLs) [17], the theoretical [18] and experimental verification [19] of their low jitter characteristics and the simultaneous research on integrated optical devices on silicon [20, 21] aroused the interest of IC designers for this topic. Here, electrical wires are replaced by optical waveguides implemented directly on the silicon chip. Photodetectors (PDs) convert the optical pulse train into an electrical one at the CDN leaves. Multimode interference (MMI) couplers serve as power dividers, while light can be coupled out of a fiber into a waveguide by a grating and an adiabatic taper. An example is shown schematically in fig. 1.1(b). Here, the H-tree topology has been adapted for the optical CDN and the pulse train comes from an external MLL. Using optical methods for clock distribution eliminates a global electrical clock interconnect, distributed buffer stages and local multipliers [7, 9]. It is immune towards crosstalk from nearby electrical wires, has a high signal speed almost independent of waveguide variations, induces only low heat generation and is not sensitive towards power supply noise due to the lack of optical buffers [7, 11, 22]. Various studies have discussed the potential of optical CDNs

for VLSI circuits [9, 11]. Here, the unsolvable problem was the limited power of the optical sources and the huge fan-out across the die [8, 9]. In contrast to electronics, there is a lack of optical repeaters and, therefore, no signal regeneration is possible. To avoid arising problems for the clock precision, microprocessor designers have preferred to push the performance evolution by using local clocks embedded within local islands and locked by a local phase-locked loop (PLL) to a multiple frequency of a global clock [7, 9] since the projections of the 2000 ITRS [9]. Moreover, the performance enhanced by executing multiple instructions per clock cycle and by parallelization through multiple cores instead of higher clock rates.

The high potential of optical CDNs remained very interesting for analog-to-digital converters (ADCs) since their performance is highly dependent on the sampling instant precision if high frequency signals are sampled [23, 24]. ADCs represent the interface between the analog physical reality and the digital domain of signal processing. The accuracy of the mapping process between these domains depends, among others, on the clock precision. Here, the timing jitter became a major bottleneck on the way towards higher resolution of higher sampled frequencies [25]. Despite a continuous research effort, the jitter in pure electronic ADCs was not significantly decreased during the last decade [26]. A typical electronic jitter limit is often named as $100\,\mathrm{fs}$ [24, 25, 26]. The lowest measured jitter for electrical clock distribution in ADCs is $60\,\mathrm{fs}$ [27, 28]. But in this case, the clock signal was provided by a high-quality external signal generator what is barely appropriate for an actual device. Digitization of high radio-frequency (RF) signals is of special interest for electronic instrumentation, radar and satellite communication, medical sensing and imaging. New optical communication standards, such as ITU OTU-4 and $100/400\,\mathrm{Gb/s}$ Ethernet, require ADCs with sampling rates of $> 50\,\mathrm{GS/s}$ and resolutions of > 5 effective number of bits to enable complex equalization in the digital domain [27]. This is only possible if the timing jitter can be reduced to $\ll 100\,\mathrm{fs}$. Hence, these requirements represent the performance target for photonic ADCs. Low jitter MLLs in combination with optical CDNs became the most promising way to deal with this bottleneck [24, 25, 29]. Optical clock distribution with sub-femtosecond jitter was already shown for a $> 1\,\mathrm{km}$ fiber link [30] and serves for synchronization of several remote devices in X-ray free electron lasers [29].

In this thesis, optical CDNs are considered essential components for distribution of ultra-low jitter pulse trains for photonic time-interleaved samplers. Time-interleaving of several parallel ADCs is the preferred way to achieve high overall sampling rates despite the low operating frequency of individual ADCs [31]. Thanks to parallelization, the requirements on electronics are less strict and the digitization can still be performed by the well-established ICs. For example, a schematic of a photonic-assisted ADC is shown in fig. 1.3 where a

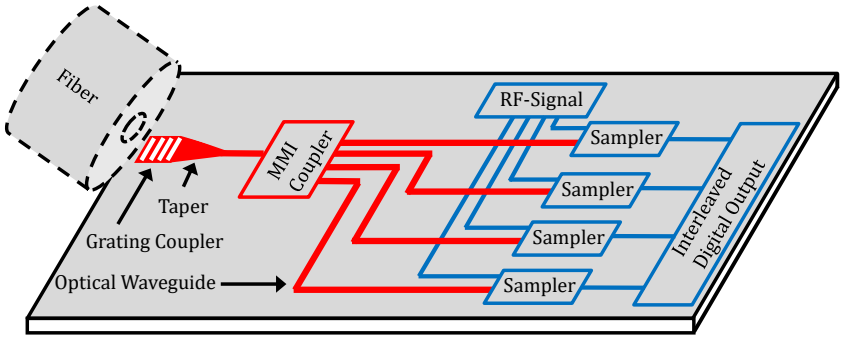

Figure 1.3: Schematic of a photonic-assisted time-interleaved ADC. A pulse train from an external MLL is coupled by grating out of a fiber into an optical waveguide integrated on a silicon die. The pulse train is split by an MMI coupler and distributed to several parallel electronic ADCs which sample the same RF signal. Time-interleaving of individual samplers is assured by different waveguide delays. Optical and electrical signal paths are highlighted in red and blue. The sampler outputs are interleaved to the digitized signal.

pulse train from an external MLL is coupled by a grating into an optical waveguide integrated on a silicon die. The signal is split into several pulse trains and distributed to each parallel sampler. The time-interleaving is warranted by different waveguide lengths. Photodiodes convert the optical pulse trains into the electrical domain. The following samplers exploit the timing precision of the resulting signal to sample an RF signal. The samplers' outputs are put together to the digitized output signal.

During the last two decades, various methods were published to use ultra-low jitter optical pulse trains to sample an RF signal and the results indicate its potential performance [9, 24, 25, 32, 33, 34, 35]. In this thesis, the term *photonic ADC* is used for all kinds of samplers which use the photonics for the digitization process of an RF signal. In the literature, there is no clear distinction of the actual photonics contribution for the use of the term photonic ADC [24]. The photonics can be used either for the sampling process [25, 32, 35], the quantization process [36] or both [34]. In fact, the photonic contribution can be reduced to clock the electronics [37, 38, 39].

This thesis investigates the performance limitations of photonic integrated ADCs where the quantization process is performed by electronics. The goal is to show that the performance of photonic integrated ADCs can be superior towards their pure electronic counterparts. Furthermore, an estimate of their full potential should be provided. The MLL remains the single non-integrated component providing the pulse train for the sampling process. The reason is the much better jitter characteristics of fiber or solid-state lasers compared to integrated semiconductor lasers. An integrated MLL on a III-V semiconductor together with silicon with sufficiently low jitter is not expected in the near future.

This thesis is organized as follows. In chapter 2, sampler basics are introduced. Several

errors in the sampling process and their impact on the ADC performance are discussed. The impact of timing errors will be introduced as the main performance limitation for high-speed ADCs. The concept of using ultra-low jitter optical pulse trains for the sampling process will be motivated as the most promising way for performance enhancement. In chapter 3, several conventional jitter definitions are introduced and their measurement are discussed. Here, the emphasis lies on jitter calculation from phase-noise measurements. In chapter 4, a silicon photonics platform will be introduced including the performance review of several components which are relevant for photonic ADCs. This technology platform was used for fabrication of several test structures to verify the analysis and discussion of photonic ADCs. In chapter 5, the potential of photonic ADCs and its realizations is discussed. A deep analysis of the MLL jitter characteristics is provided since it is the basic motivation for the research effort of photonic ADCs. The expected characteristics of optical pulse trains will be provided for the following jitter analysis of photonic ADCs in chapter 6. Here, a quantum noise model is derived able to describe the photodetection process including various fundamental noise sources. Two principle photonic sampling techniques will be identified and the noise impact on them discussed. By means of the introduced quantum noise model, formulas will be derived for the jitter performance regarding several noise sources. These enable an accurate comparison of both sampling techniques and the discussion of the full potential of photonic ADCs. The experimental results will be given in chapter 7. Limitations of optical CDNs, which affect the photonic ADC performance, will be shown experimentally. The jitter characteristics of a realized opto-electronic clock converter (OECC) serve for verification of the provided theoretical jitter analysis from chapter 6. Its characterization results will be discussed in detail. Finally, in chapter 8, the thesis results are summarized.

Chapter 2

Sampler Basics

In this chapter, the analog-to-digital converter basics are introduced. The sampling and quantization processes are described on the basis of electronic ADCs and the most important ADC architectures will be named. Their characteristics are discussed regarding amplitude and timing errors. Based on the presented performance limitations of high-speed electronic ADCs, the motivation for photonic ADCs will be provided. These will be discussed in chapter 5.

An electronic ADC has the two basic functions *sample-and-hold* and *quantization*. In the first step, the sampled input signal charges a capacity to a voltage level proportional to the input signal within a short time period. Afterwards, this induced value is held for the second step where it is mapped to one of the possible discrete levels. Finally, the quantized value is saved in a corresponding code word which can be processed in the digital domain.

The sample-and-hold process can be described mathematically by ideal sampling with subsequent widening of the sampled value for the hold time [40]. This principle is known as flat-top sampling. Here, an input signal $u(t)$, which is continuous in time and value, results in an output signal [40]

$$u_a(t) = [u(t) \cdot \delta_{T_s}(t)] * \sqcap_{\gamma T_s}(t), \tag{2.1}$$

which is discrete in time but continuous in amplitude. The multiplication with the Dirac comb

$$\delta_{T_s}(t) = \sum_{k=-\infty}^{\infty} \delta(t - kT_s) \tag{2.2}$$

corresponds to ideal sampling, where T_s is the sampling period and $\delta(t)$ is the Dirac function. The hold process is represented by convolution "$*$" of the result with the rectangular

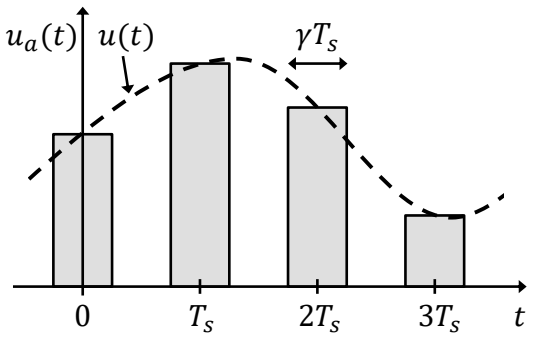

Figure 2.1: Principle of the sample-and-hold process: input signal $u(t)$ is ideally sampled with the sampling period T_s. The resulting value is held for a time period γT_s forming the time discrete output signal $u_a(t)$.

function

$$\sqcap_{\gamma T_s}(t) = \begin{cases} 1, & |t| < \gamma T_s/2 \\ 0.5, & |t| = \gamma T_s/2 \\ 0, & |t| > \gamma T_s/2 \end{cases} \tag{2.3}$$

where γ indicates the relative fraction of the sampling period T_s. The principle is shown in fig. 2.1. To illustrate the sampling impact on the output spectrum, the Fourier transform

$$U(f) = \mathcal{F}\{u(t)\}(f) = \int_{-\infty}^{\infty} u(t) e^{-j2\pi ft} \mathrm{d}t \tag{2.4}$$

of a time signal $u(t)$ is introduced. Here, j is the imaginary number and f is the frequency. The corresponding inverse transform is

$$u(t) = \mathcal{F}^{-1}\{U(f)\}(t) = \int_{-\infty}^{\infty} U(f) e^{j2\pi ft} \mathrm{d}f. \tag{2.5}$$

Using eq. (2.1) in eq. (2.4) results in the sampled output spectrum [40]

$$U_a(f) = \gamma \cdot \mathrm{sinc}\,(\pi\gamma T_s f) \sum_{k=-\infty}^{\infty} U(f - kf_s), \tag{2.6}$$

where $\mathrm{sinc}(x) = \sin(x)/x$. It corresponds to copies of the input spectrum $U(f)$ at multiples of the sampling frequency $f_s = 1/T_s$ whose amplitudes are scaled by the function $\gamma \cdot \mathrm{sinc}(\pi\gamma T_s f)$. This is illustrated in fig. 2.2. As can be seen in fig. 2.2(b), the original spectrum can be derived from the sampled values by using a low-pass filter with the cut-off frequency $f_s/2$. Unfortunately, higher frequencies of the base spectrum are attenuated in dependence on the hold time γT_s. The induced distortion of the original spectrum shrinks for shorter hold times. Furthermore, a low-pass filter in front of the sample-and-hold element is useful to limit the maximum sampled frequency to avoid *aliasing effects*. This

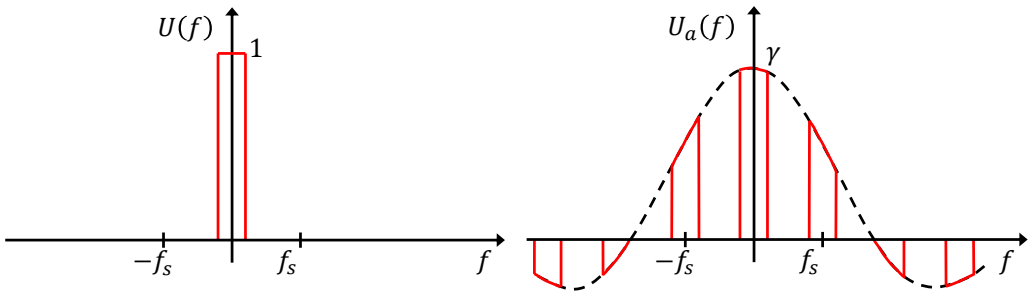

(a) (b)

Figure 2.2: Spectral impact of the sample-and-hold process: (a) input spectrum $U(f)$ (b) output spectrum $U_a(f)$

happens if the input signal bandwidth is larger than half of the sampling rate what is known as the *Nyquist theorem* [40]. In this case, the spectral components located at multiples of the sampling frequency would overlap in fig. 2.2(b) and the discretized signal would get distorted.

During the hold time, the sampled continuous amplitudes $u(kT_s)$ are mapped by a quantization operator [40]

$$Q[u(kT_s)] = v(kT_s) \qquad \text{if} \qquad u(kT_s) \in (u_j, u_{j+1}) \tag{2.7}$$

to discrete values $v(kT_s)$ which are usually the averages of the amplitude intervals (u_j, u_{j+1}). These result from the full scale input range $u_{rng} = u_{max} - u_{min}$ and the number of quantization levels. The quantization diagram of an $N = 3$ bit quantizer with $2^N = 8$ levels is shown in fig. 2.3. As an example, the amplitude interval (u_2, u_3) is illustrated. The zero value cannot be represented by the symmetrical quantization diagram. This form of a quantizer is called *mid-riser*. Shifting the blue characteristic curve in fig. 2.3 to the left or right by half of the quantization interval induces an asymmetry but allows the representation of a zero value. Such a quantizer is called *mid-tread*. Discretization is always accompanied by a quantization error

$$q(kT_s) = u(kT_s) - v(kT_s) \tag{2.8}$$

which is indicated by the red curve in fig. 2.3. Assuming equal probability distribution of the quantization error amplitude within every amplitude interval (u_j, u_{j+1}), the quantization noise variance can be calculated as [41]

$$\langle q^2 \rangle = \frac{\Delta_q^2}{12} \tag{2.9}$$

where $\Delta_q = u_{rng}/2^N$ is a quantization interval and $\langle ... \rangle$ denotes the expectation value. Δ_q is also called the *least significant bit* and is indicated in fig. 2.3. In general, the quantization

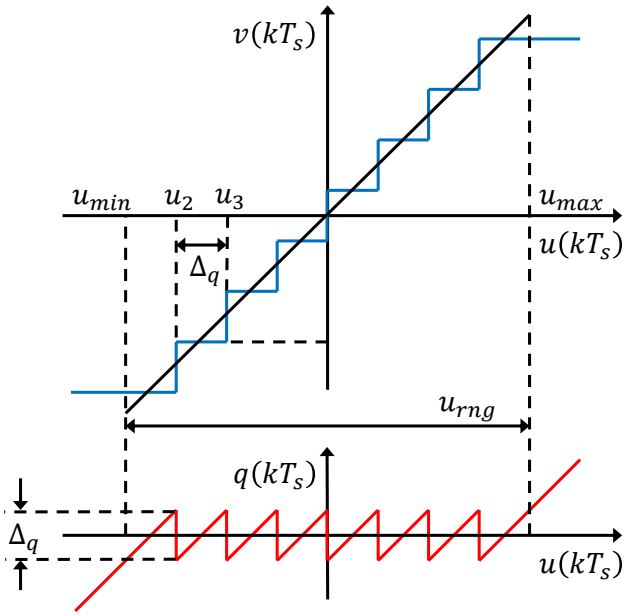

Figure 2.3: 3-bit quantization diagram of a mid-riser where continuous amplitudes $u(kT_s)$ are mapped to discrete values $v(kT_s)$. This is accompanied by a quantization error $q(kT_s)$.

intervals do not have to be uniform. If the probability distribution of the input amplitudes is known, it can be beneficial to choose different amplitude intervals in the quantization diagram so that the effective quantization error is minimized [41].

The ADC performance is often described by the signal-to-noise ratio (SNR) in dB. It is defined as the ratio of the root-mean-square (rms) signal power P_s to the rms noise power P_n. An ideal ADC with quantization as the single present noise source leads to [40, 41, 42]

$$\text{SNR} = 10 \cdot \log_{10}\left(\frac{P_s}{P_n}\right) = 6.02N + 1.76 \qquad \text{[dB]} \tag{2.10}$$

for an N bit ADC. Eq. (2.10) is valid for a sinusoid with minimum and maximum amplitudes u_{min} and u_{max} which exploits the full scale input range of the quantization diagram. Other signal forms affect eq. (2.10) by a different addend than 1.76 [41].

2.1 Amplitude and Timing Errors in the Sampling Process

In this section, errors in the sampling process are addressed which decrease the ideal ADC resolution to an effective number of bits (ENOB) $N_{eff} < N$. These errors can be categorized as amplitude and timing errors.

Thermal noise (or Johnson-Nyquist noise) within the signal path distorts the sampled signal amplitude and deteriorates the ADC resolution. It results from thermal carrier movement in electronic circuits. Usually, it is considered by an effective thermal noise resistance R_Ω at

temperature T at the input of a noise free ADC [23, 26]. Its power spectral density (PSD) $S_{n,th}(f)$ is considered white within the electronic circuit bandwidth B_w. The mean squared voltage noise of the effective resistance can be expressed as [23, 26]

$$\left\langle u_{n,th}^2 \right\rangle = S_{n,th}(f) B_w = 4 k_B T R_\Omega B_w \tag{2.11}$$

where k_B is Boltzmann's constant. The impact of thermal noise superimposed to the signal can be seen as equivalent to quantization noise. Therefore, an effective resolution can be calculated by equating eqs. (2.11) and (2.9) and solving for the bits. These decrease from the ideal ADC resolution N to an ENOB [23]

$$N_{eff,th} = \frac{1}{2} \log_2 \left(\frac{u_{rng}^2}{24 k_B T R_\Omega f_s} \right) \tag{2.12}$$

which is not an integer anymore. The relation $\Delta_q = u_{rng}/2^{N_{eff,th}}$ has been used where the bits N has been replaced by an effective value. In eq. (2.12), a Nyquist ADC with the circuit bandwidth $B_w = f_s/2$ has been assumed. Obviously, eq. (2.12) is only valid for the interesting case where the mean squared voltage noise in eq. (2.11) is much smaller than the squared full scale input range $\langle u_{n,th}^2 \rangle \ll u_{rng}^2$.

The relation (2.12) is derived for ideal sampling when the superimposed noise at the sampling instant corresponds directly to the sampled amplitude error. A real electronic circuit does not generate Dirac functions as the sampling function like assumed in eq. (2.1) but pulses with a finite duration and amplitude [42]. In an actual converter, the sampling is performed by turning on a switch for a time period γT_s around the sampling instants kT_s to charge a sampling capacity C_s with a voltage $u(kT_s)$ proportional to the input signal $u(t)$. This is illustrated in fig. 2.4(a). The switch is turned off during the hold time for the quantization process. An equivalent noise circuit is shown in fig. 2.4(b). Here, the thermal noise $u_{n,th}(t)$ described by the effective thermal noise resistance induces a noise signal $u_{n,C}(t)$ at the sampling capacity. The one-sided power spectrum of this voltage noise can be obtained from the spectrum of the thermal noise resistance $S_{n,th}(f)$ and the square of the transfer function of the $R_\Omega C_s$ low pass filter to [42]

$$U_{n,C}^2(f) = \frac{4 k_B T R_\Omega}{1 + \left(2\pi f R_\Omega C_s\right)^2}. \tag{2.13}$$

The corner frequency of the $R_\Omega C_s$ low pass filter is much larger than the Nyquist limit. Therefore, aliasing folds noise components from higher Nyquist zones into the baseband. The integrated noise power in the baseband results in [42]

$$\left\langle u_{n,C}^2 \right\rangle = \int_0^\infty U_{n,C}^2(f) \mathrm{d}f = \frac{4 k_B T R_\Omega}{4 R_\Omega C_s} = \frac{k_B T}{C_s} \tag{2.14}$$

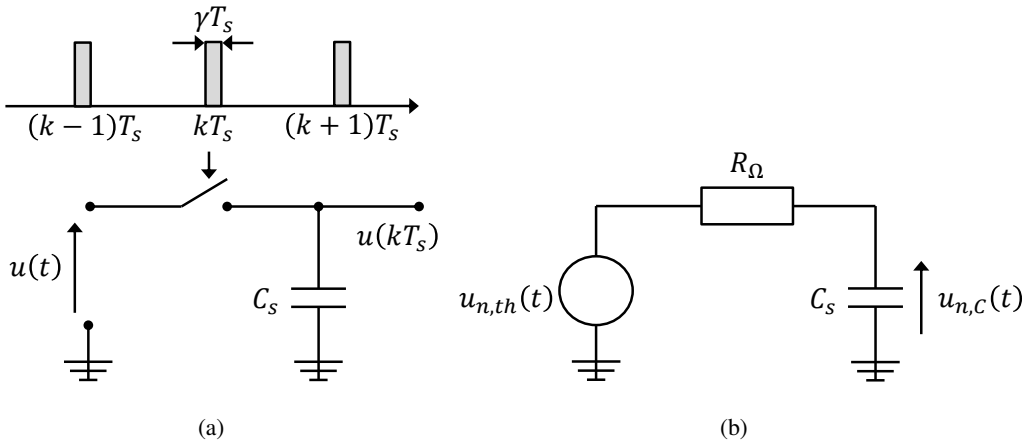

Figure 2.4: Thermal noise impact on sampling process: (a) principle sampler model (b) equivalent noise circuit

which corresponds to the variance according to Parseval's theorem. It should be noted that eq. (2.14) does not depend on the effective thermal noise resistance anymore. Higher R_Ω is raising the white noise floor while the low pass bandwidth is shrinking. These two effects compensate each other. The k_BT/C_s noise given by the sampling capacity and the temperature is another fundamental limit next to quantization noise [42]. It should be noted from the derivation that k_BT/C_s noise and thermal noise are equivalent. For example, using the 3 dB corner frequency of the $R_\Omega C_s$ low pass filter as the electronic circuit bandwidth $B_w = 1/4R_\Omega C_s$ transforms eq. (2.14) into the thermal-noise-induced variance of eq. (2.11).

Furthermore, *shot noise* resulting from the charge quantum nature is superimposed to the signal as well affecting the ADC resolution in a similar way. The mean squared current noise within an electronic circuit bandwidth B_w is proportional to the input current and can be expressed as

$$\left\langle i_{n,sh}^2 \right\rangle = 2qIB_w \tag{2.15}$$

where q is the electric charge. Since shot noise is not constant and depends on the time-dependent signal current I, a general derivation for the ENOB for arbitrary input signals is difficult. Lower amplitudes are more distorted than higher amplitudes.

Another source for amplitude errors is the *comparator ambiguity*. This effect stems from the finite transistor speed in the comparators able to respond to a voltage change at the input and is, therefore, dependent on the transition frequency of the semiconductor technology [23]. It is defined as the frequency f_T at which there is unity current gain. Comparator ambiguity limits the ENOB to [23]

$$N_{eff,comp} = \frac{\pi f_T}{6.93 f_s} - 1.1. \tag{2.16}$$

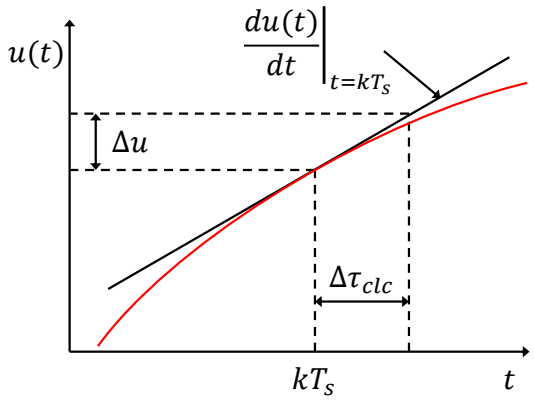

Figure 2.5: Sampling instant deviation $\Delta\tau_{clc}$ induces an amplitude error Δu during the sampling process which is proportional to the derivative of the input signal at the sampling instant kT_s.

This is valid for a full-flash converter as the fastest and most sensitive architecture to comparator ambiguity. A detailed derivation of eq. (2.16) can be found in [23] and will not be repeated here. It is mentioned for the sake of completeness. The considered time-interleaved architecture in this thesis avoids the strong requirements on the comparators. Electronic ADC architectures will be discussed in section 2.2.

In chapter 1, the clock uncertainty was mentioned. A clock signal defines the sampling instants corresponding to the Dirac comb in eq. (2.1). Superimposed random noise in the clock path induces an uncertainty of these sampling instants σ_{clc} which is known as *clock jitter* or *aperture jitter*. It leads to errors of the sampled amplitudes. This error can be approximated by the derivative of the input signal at the sampling instant multiplied by the timing error $\Delta\tau_{clc}$ [43] illustrated in fig. 2.5. Therefore, in the presence of clock jitter, lower signal frequencies can be sampled with higher ENOB. The worst case degradation of the ADC resolution due to jitter is for a sinusoid with the highest input frequency $f_s/2$ and sampling instants at the zero crossings. In this case, the ENOB can be calculated to [23, 24]

$$N_{eff,clc} = \log_2\left(\frac{1}{\sqrt{3}\pi f_s \sigma_{clc}}\right) \tag{2.17}$$

where σ_{clc} is the standard deviation of the timing error. In chapter 1, the target resolution for photonic ADC performance was named as > 5 ENOB for sampling rates of > 50 GS/s to support new optical communication standards. The resulting jitter requirement can be derived from eq. (2.17). Assuming a resolution of $N_{eff,clc} = 6$ ENOB for sampled frequencies of $f_s/2 = 30$ GHz, 40 GHz and 50 GHz results in a jitter of $\sigma_{clc} < 48$ fs, 36 fs and 29 fs. Such a low jitter has not been achieved by electronic clock distribution so far. It motivates the ansatz of this thesis to provide this clock precision by optical clock distribution.

The ultimate limit for the ADC resolution-sampling rate product results from the Heisen-

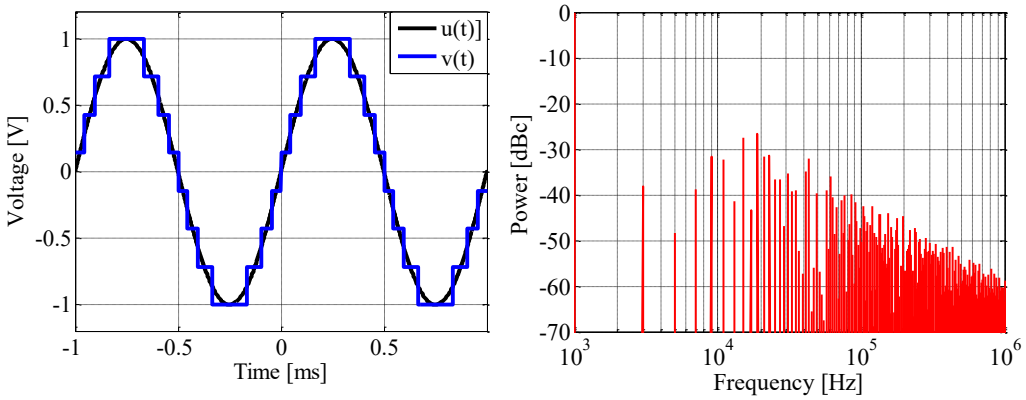

(a) (b)

Figure 2.6: Quantization of a sinusoid: (a) input signal $u(t)$ and its quantized output $v(t)$ (b) resulting output spectrum normed to the carrier power

berg uncertainty principle $\Delta E \Delta t > h/2\pi$, where h is Planck's constant. The energy of the smallest resolvable signal $\Delta E = \Delta t(\Delta_q/2)^2/R_\Omega$ is equivalent to half of the least significant bit $\Delta_q/2 = u_{rng}/2^N/2$ during half of the sampling period $\Delta t = 1/2f_s$ at a load resistance R_Ω [23]. Using this relation and solving for the ENOB results in [23]

$$N_{eff,heis} = \log_2\left(\sqrt{\frac{\pi}{8R_\Omega h}} \cdot \frac{u_{rng}}{f_s}\right). \tag{2.18}$$

This is negligible compared to previously mentioned amplitude and timing errors.

Non-linearity in the sampling process is another ADC characteristic deteriorating the resolution. The quantization diagram is one obvious non-linearity due to the discrete output values. The impact of discretization of an input sinusoid is shown in fig. 2.6 for the 3-bit quantizer from fig. 2.3. The output spectrum is normed to the power of the carrier frequency of 1 kHz. Here, the induced errors are strongly correlated with the input signal. In the spectral domain, these errors result in harmonics of odd orders of the input frequency called *spurs*. The odd order characteristic stems from the odd-symmetric nature of the considered mid-riser quantizer in fig. 2.3 [44, 45].

Another example for non-linearities is *clipping*. It represents the signal distortion if the input signal amplitude exceeds the quantizer input range. Real quantizers show non-uniform quantization intervals Δ_q already due to component mismatches. Furthermore, there are deviations from the ideal straight interpolating line in fig. 2.3. These are called differential non-linearity and integral non-linearity. They increase the quantization noise power above that of an uniform quantizer [26] given in eq. (2.9). All these non-linearities induce spectral spurs.

The ratio of the carrier power to the highest spur power is called *spurious-free dynamic*

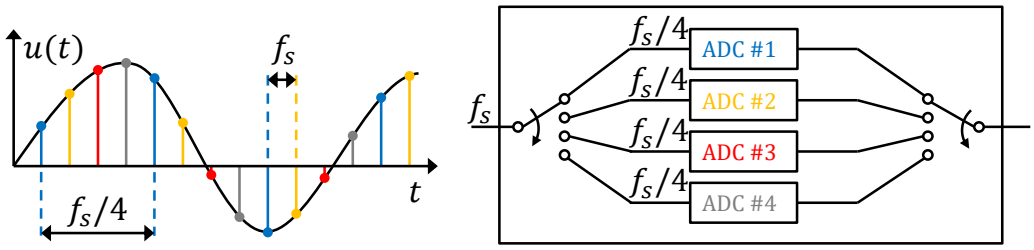

(a) (b)

Figure 2.7: 4 time-interleaved ADCs increase the overall sampling rate by factor 4: (a) input signal $u(t)$ is sampled by 4 individual ADCs with identical delays between each sampling instants (b) schematic of 4 switched ADCs with a sampling rate of $f_s/4$ corresponding a net sampling rate of f_s

range (SFDR) and is approximately 26 dB for the example in fig. 2.6. The output spectrum was obtained numerically by the Fast Fourier Transform in MATLAB. Error correlations between successive samples decrease if noise is superimposed on the ideal input signal. This decorrelation method is called *dithering* and can be used to increase the SFDR [44, 45]. It can be beneficial to enhance the SFDR performance at the expense of higher SNR like in receivers of wireless communication systems [45]. The SFDR determines the system ability to resolve weak signals in a crowded spectrum with unwanted and strong nearby interferers [43].

Other forms of non-linearities affect the sampling process in the same way decreasing the ENOB further. Including non-linear signal distortion into the SNR definition of eq. (2.10) results in the *signal-to-noise and distortion ratio* (SINAD)

$$\text{SINAD} = 10\log_{10}\left(\frac{P_s}{P_n + P_d}\right) \qquad \text{[dB]} \tag{2.19}$$

where P_d is the power of the distortion error. It can be related to the ENOB by using the SINAD instead of the SNR in eq. (2.10). This leads to [24]

$$N_{eff,SINAD} = \frac{\text{SINAD} - 1.76}{6.02} \tag{2.20}$$

for a sinusoid. This relation is useful since both ADC properties are rarely mentioned in publications.

In chapter 1, a time-interleaved ADC has already been introduced as a way to increase the overall sampling rate without the need to enhance the speed of electronics. Its principle is illustrated in fig. 2.7. The same signal $u(t)$ is sampled by 4 individual ADCs with the sampling rate $f_s/4$. Since the relative sampling instants are chosen in such a way that there is the same time interval between the 4 ADCs, the interleaved device is equivalent to a single ADC with a net sampling rate of f_s. The main disadvantage of time-interleaving is the necessary synchronization of the parallel ADCs. The delays between the sampling

instants of each ADC have to be very precise. Static timing errors between individual ADCs are called *skew*. These induce spurs in the sampled spectrum and decrease the ENOB. Furthermore, relative amplitude errors induce more spurs. Examples are the output gain differences and amplitude offsets between parallel ADCs. These timing and amplitude errors between interleaved ADCs are called *channel mismatches*. For a large number of interleaved ADCs channel mismatches can be partially avoided by using a low number of samplers and a large number of sub-samplers [31]. The high clock requirements are then reduced to the low number of front-end samplers [31]. Usually, channel mismatches in time-interleaved ADCs are minimized in a previous calibration step [27, 28, 46].
Moreover, switching noise of nearby analog and digital electronic circuits can deteriorate the ADC performance. These interferences propagate as transients on power supply lines, through the substrate or by inductive and capacitive coupling [26] affecting both the clock and the signal path. Its impact can be suppressed by supply separation [26, 46], decoupling [46], guard-rings or electromagnetic shielding [26]. Switching interference increases the total noise level and is barely distinguishable from thermal noise [26].
All mentioned sampling errors affect the overall ADC resolution and have to be minimized to enhance the sampler performance.

2.2 Electronic Analog-to-Digital Converter Architectures

There are several ways to implement electronic converters. A *full-flash* ADC is an intuitive architecture performing the quantization within one clock cycle and is the fastest architecture. Here, $2^N - 1$ comparators compare simultaneously the sampled and held voltage with references generating a row of binary values corresponding to the thermometer code. A subsequent decoder converts it into the more compact binary code. Such ADCs guarantee high throughput rates but are only acceptable for a low number of bits since the amount of comparators grows exponentially with N [23, 38, 45]. Consequently, the ICs become very large and the power dissipation very high [23]. The matching condition within the comparator chain or the comparator precision, respectively, is a high challenge [23, 42] and built-in calibration mechanisms are necessary for offset error compensations [38]. Furthermore, the overall capacity of the comparators is very high. It requires a high current from the sample-and-hold circuit for charging or discharging [42] the comparators' capacity and reduces the analog bandwidth [23]. In summary, full-flash ADCs are typically used for conversion rates of $< 1\,\text{GS/s}$ and resolutions of $< 8\,\text{bits}$ [23, 28, 31, 42].
Variations on the flash architecture address its restrictions by reducing the number of comparators. Here, more than one clock cycle is necessary for the conversion [23, 42]. Normally, this leads to more accuracy, less power dissipation, lower chip area and reduced

conversion rates [42].

In a *sub-range* algorithm, the quantization is performed in two steps [42]. At first, an M bit flash-ADC performs a coarse conversion. Afterwards, a digital-to-analog converter (DAC) transforms the M bits back and the result is subtracted from the held input voltage. A second N bit flash-ADC converts the residue in a fine conversion step.

In a *two-step* algorithm, the residue is amplified before the fine conversion [42]. Such a gain stage enables a better estimation of the least significant bits. If the gain equals 2^M, the reference voltages of both flash ADCs can be shared. Since the sample-and-hold component limits the speed of medium resolution full-flash ADCs, the clock of the sub-ranging scheme can end up being higher thanks to the reduced overall capacity being driven by the sample-and-hold [42].

A *folded flash* performs a coarse conversion by folding the input with a multiple ramp function, while the fine conversion is performed by a flash architecture [42]. Here, the same comparator is used more than once reducing its overall amount.

Successive approximation (SAR) algorithms perform the conversion over multiple clock cycles by exploiting the knowledge of previously sampled bits [23, 42]. Each bit is set at one clock cycle. Such ADCs reduce the electronic circuit complexity and power consumption but allow only low conversion rates. Nevertheless, for a high resolution of > 6 bit, SAR ADCs are attractive due to the low number of comparisons to determine the output and the absence of amplification during conversions as used in pipelined ADCs [31].

Pipeline architectures extend the two-step conversion to multiple steps and cascade a number of stages [42]. Successive approximation algorithms can also be realized in a pipeline where each bit is set in a new stage instead in one clock period. The pipeline over several clock cycles generates latencies which can cause problems in a feedback loop.

Time-interleaving of several converters is a typical method to increase the overall sampling rate despite the slow conversion rates of individual ADCs. The parallelization multiplies the sampling rate by the number of interleaved ADCs which has already been introduced in fig. 2.7. This thesis focuses on the photonic sampling to overcome the jitter bottleneck for high speed ADCs if high frequency signals are sampled. In this context, the time-interleaving concept is essential. It eliminates the resolution restriction due to the comparator ambiguity discussed by means of eq. (2.16). Then, the timing jitter remains as the major impact on the ADC resolution according to eq. (2.17). This problem is addressed by photonic ADCs by means of ultra-low MLLs and optical clock distribution.

SAR ADCs are known for their flexible architecture and power efficiency and became more popular over flash or pipelined ADCs although running at slower clock rates [27, 28, 31]. Time-interleaved SAR ADCs have become the favorite architecture for high-speed con-

verters with sampling rates of $> 10\,\text{GS/s}$ [27, 28, 31, 46]. Unfortunately, the fastest SAR ADCs are in the range of $1\,\text{GS/s}$ and necessitate a very high interleaving number [31]. For example, the high sampling rate of $90\,\text{GS/s}$ in [27] has been achieved with 64 interleaved SAR ADCs. In this case, only the 4 front-end sampler and interleaver have been highly sensitive to the clock uncertainty. The timing precision for the 64 sub-samplers has been less critical. In [28] only 2 front-end samplers and interleavers are clock sensitive that feed buffered samples to 32 time-interleaved SAR sub-ADCs. Best electronic high-speed ADCs have been realized by time-interleaving of flash or SAR converters [27, 28, 31, 46].
More ADC architectures can be taken from literature [42] and are beyond the scope of this thesis.

2.3 Performance of Electronic Analog-to-Digital Converters

In this section, the evolution of electronic ADC performance is presented based on several surveys [23, 24, 26, 47]. A link is created between the noise sources mentioned in the previous section and the limiting resolution of state-of-the-art electronic ADCs.
The first extensive survey of ADC performance was carried out by Walden in [23]. In his study, realized electronic ADCs have been inserted as dots in an ENOB versus sampling rate plot. This so-called *Walden plot* became an excellent reference for researchers for performance assessment of their ADC realizations [24, 25, 26, 38]. Fundamental performance limits in the Walden plot can be shown simply by inserted lines regarding thermal noise, clock jitter, comparator ambiguity and Heisenberg uncertainty like illustrated in fig. 2.8. Here, Nyquist ADCs have been assumed where the maximum input frequency is equal to half of the sampling rate. The thermal noise has been calculated by means of eq. (2.12) for a full-scale voltage range of $u_{rng} = 1\,\text{V}$ and a temperature of $T = 300\,\text{K}$. The two red lines are inserted in fig. 2.8 regarding an effective thermal noise resistance of $R_\Omega = 50\,\Omega$ and a more realistic $R_\Omega = 2\,\text{k}\Omega$ for state-of-the-art electronic ADCs [26]. It can be seen that the thermal noise is the limiting factor for the resolution of sampled frequencies $< 1\,\text{MHz}$. Heisenberg uncertainty has been included by means of eq. (2.18). The cyan line illustrates the ultimate measurement limit. Again, a full-scale voltage range of $u_{rng} = 1\,\text{V}$ and a load resistance of $R_\Omega = 50\,\Omega$ have been assumed. Comparator ambiguity is shown by the green lines for technologies with transition frequencies of $f_T = 250\,\text{GHz}$ and $f_T = 500\,\text{GHz}$ according to eq. (2.16). Their impact on ADC resolution is huge for very high input frequencies of tens of gigahertz. Nevertheless, time-interleaved architectures relax the comparator speed requirements by the number of interleaving stages so that the actual fundamental limit for high-speed ADCs is defined by timing jitter [48]. The ENOB decrease due to jitter was given in eq. (2.17). Its impact on the resolution is indicated by the blue lines in fig. 2.8 for

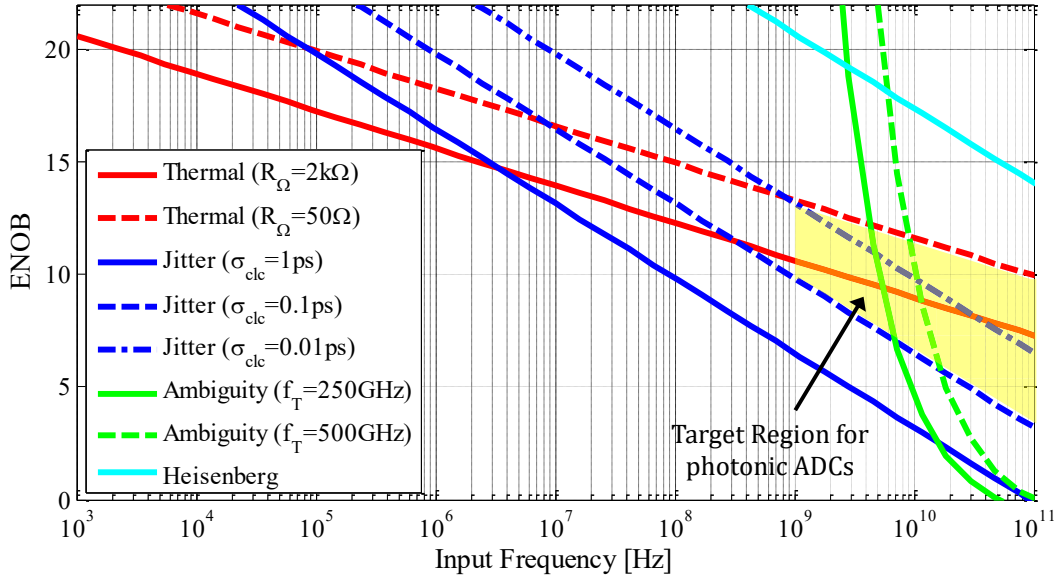

Figure 2.8: ADC resolution in ENOB as a function of the input frequency. The fundamental performance limits result from thermal noise, comparator ambiguity, clock jitter and Heisenberg uncertainty. Assumptions are discussed in the text. The target region for photonic ADCs is marked in yellow.

jitter values of $\sigma_{clc} = 1\,\text{ps}$, $\sigma_{clc} = 0.1\,\text{ps}$ and $\sigma_{clc} = 0.01\,\text{ps}$. The target region for photonic ADCs is marked in yellow. These have to outperform the jitter limit of electronic ADCs of $100\,\text{fs}$ [24, 25, 26]. This thesis is focused on integrated photonic ADCs where the quantization is performed by electronics. Therefore, the unavoidable thermal noise represents the upper limit for the resolution. In fig. 2.8, this resolution limit results from an effective thermal noise resistance of $50\,\Omega$.

The clock signal on chip is usually derived from an external low jitter crystal oscillator [43, 46, 49]. It serves as an input frequency reference for a PLL implemented on chip. It consists of a phase detector, a loop filter, a VCO and a frequency divider [43]. This is indicated in the block diagram of fig. 2.9. The PLL is locked to an external clock frequency f_{ref} and generates an M-times higher clock frequency by means of a VCO and a frequency divider. The frequency divider is necessary since low jitter crystal oscillators usually have frequencies of $< 1\,\text{GHz}$, while higher clock frequencies are desired on chip. The instantaneous phase deviation $\varphi_{ref} - \varphi_o'/M$ between the input and the output frequencies is measured by a phase detector and the filtered output signal u_{VCO} multiplied by a gain K_{VCO} serves for the correction of the VCO frequency. The loop filter creates a low pass characteristic for the closed loop PLL (clock in $\rightarrow$ clock out) and, therefore, reduces high frequency jitter components of the external oscillator. It has also a high pass characteristic for the open loop PLL (VCO $\rightarrow$ clock out) leading to unattenuated contribution of high frequency components of the VCO jitter. The open and closed loop PLL transfer functions

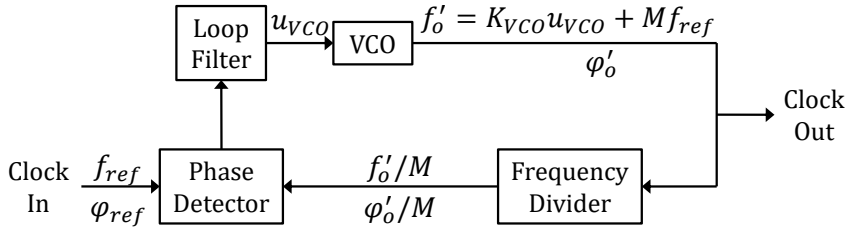

Figure 2.9: Block diagram of a PLL locked to an external clock frequency f_{ref}. The PLL generates an M-times higher clock frequency Mf_{ref} by means of a VCO and a frequency divider. An instantaneous error is measured by a phase detector and its filtered signal serves for VCO frequency adjustment.

are typically of a second order [43, 49]. Jitter stemming from the VCO is usually higher compared to the external reference, but most of its energy is concentrated at low frequencies and is suppressed by the loop filter [43]. The filter bandwidth is a trade-off between jitter contributions of the reference oscillator and the VCO.

Fundamental noise limits for VCOs result from thermal, shot and flicker noise of the electronic components [50, 51, 52, 53, 54, 55, 56, 57, 58] as well as from picked-up noise from nearby switching electronic circuits and from supply and substrate noise [50, 51, 52, 56]. They have been explored for various implementations such as single-ended [51, 52, 56] or differential [50, 51, 52, 56] (CMOS) ring oscillators and single-ended [51, 58] or differential [53, 54, 55, 57, 58] (CMOS) inductance-capacitance (LC) oscillators. Differential signals are used to mitigate the impact of nearby switching electronic circuits and supply and substrate noise [27, 28, 50, 52, 56]. LC oscillators usually have better jitter characteristics than ring oscillators but are less compact and consume significantly more chip area [51, 52, 56]. While ring oscillators dissipate all the stored energy in the capacitors during every cycle, LC oscillators dissipate only a fraction of the energy oscillating between the inductance and the capacitance per cycle [51, 52]. Their fundamental jitter limit is given by the minimum realizable inductance, its maximum quality factor, the resonator topology and the oscillation amplitude [50, 52, 54, 57, 58]. A more general interpretation refers to the resonator sensitivity and the overall tank loss which has to be compensated by an active device [59]. The induced gain is accompanied by unavoidable electronic circuit noise which causes a diffusion process for the jitter and can be characterized by a diffusion coefficient [29, 59]. This general interpretation enables a comparison between microwave oscillators and mode-locked lasers (MLLs). It indicates orders of magnitude better jitter performance for the MLLs [29]. Moreover, the electronic clock distribution across the die, especially for time-interleaved ADCs, increases the jitter.

State-of-the-art electronic ADCs achieve clock jitter values in the range of $\sim 100\,\mathrm{fs}$. This value was observed by Valley in 2007 [24] and has not been improved significantly since

then [26, 47]. Thermal noise of the resonator and the active elements of the oscillator set a fundamental jitter limit [25]. Moreover, picked-up power supply or substrate noise is an important jitter source but can be minimized by careful layout, decoupling and wiring of separate power domains [31]. The available power budget on the clock path sets the minimum achievable clock jitter due to thermal noise [31]. Higher supply voltage can reduce the limit but a clock jitter reduction by a factor of 2 requires a 4-times-higher power [31]. This is a critical requirement in regard of the technology scaling process [26, 60]. Shrinking technology enables higher bandwidths while the SNR is decreasing. Due to the supply voltage down-scaling, the relative noise floor is raising. And keeping higher supply voltage while increasing the clock frequency increases the dissipated power to critical levels. The most advanced designs exhibit $\approx$ 60-80 fs clock jitter [25, 27, 28, 31] and significant improvement is not expected due to the mentioned unavoidable noise sources.

In summary, the clock jitter became a major bottleneck for high-speed and high-accuracy ADCs [25, 26] and a significant improvement by electronics alone is unlikely. But better performance is necessary, for example to meet the requirements for new optical communication standards such as ITU OTU-4 and $100/400$ Gb/s Ethernet. These require ADCs with sampling rates of > 50 GS/s and resolutions of > 5 ENOB to enable complex equalization in the digital domain [27]. As a solution to overcome the jitter limit, photonic ADCs were investigated during the last decades since MLLs can provide pulse trains with timing precision in the sub-femtosecond range [61, 62, 63, 64, 65]. External microwave oscillators, such as sapphire-loaded cavity resonators (eventually even cryogenically cooled) can actually deliver ultra-low jitter clock signals but at impractically higher cost and size [25]. Furthermore, its connection to the chip, the eventual higher frequency generation on chip by means of an integrated VCO within a PLL and its subsequent clock distribution to individual sinks across the die would eliminate the low jitter performance.

Based on the provided discussion of the fundamental resolution limits of high-speed electronic ADCs and the requirement for future high-speed ADCs, the target performance of photonic ADCs can be defined: The research effort of photonic ADCs can only be justified if these enable sampling of input frequencies > 30 GHz with resolutions of > 6 ENOB that would outperform state-of-the-art electronic high-speed ADCs. The corresponding target area is marked in yellow in the Walden plot in fig. 2.8. For comparison, the ADC in [46] achieved a resolution of 3.9 ENOB for a signal frequency of 18 GHz with a sampling rate of 40 GS/s. It was realized by 16 time-interleaved SAR ADCs and the clock jitter was measured to 250 fs. The ADC in [27] achieved a SINAD of 33 dB for a 3 dB signal frequency of 19.9 GHz at a sampling rate of 90 GS/s. Using eq. (2.20) results in 5.2 ENOB. In this case, 64 interleaved SAR sub-ADCs were used but only the 4 front-end samplers were highly

sensitive to the clock signal. Very similar results can be found for the Nyquist ADC in [28]. Here, 32 interleaved SAR sub-ADCs and 2 front-end channel ADCs were used. A SINAD of 31.6 dB was measured for an input frequency of 18 GHz which corresponds to 5 ENOB according to eq. (2.20). The ADCs in [27] and [28] used a half-rate external differential clock. By discarding an on-chip VCO in both cases an on-chip clock jitter of 60 fs was achieved. Unfortunately, no details were provided about the clock reference. Assuming an expensive ultra-low jitter signal generator would prevent practicability of such ADCs. Nevertheless, these ADCs serve as references in the following analysis and photonic ADCs have to compete with their performances.

This thesis is focused on the investigation if integrated photonic ADCs can fulfill the requirements for future high-speed samplers. In chapter 4, a promising silicon photonics technology platform will be introduced which enables fabrication of the targeted photonic ADCs. This technology platform is used for device fabrication which will be characterized in chapter 7. Photonic ADC architectures as well as optical pulse trains characteristics will be discussed in chapter 5. A theoretical quantum noise model will be introduced to analyze the fundamental performance limits of integrated photonic ADCs in chapter 6. Based on theoretical and experimental results, the potential of integrated photonic ADCs will be concluded in chapter 8.

Chapter 3

Jitter Measurement

In this chapter, the term jitter is defined and its measurement techniques are introduced. Jitter, as a general timing uncertainty, has actually several definitions in the literature. It depends on the considered system and the measurement which term is of interest. The differences are illustrated in fig. 3.1 for a square wave signal. Often jitter is defined as the timing uncertainty of a certain signal transition. Usually, a threshold level at the highest slew rate of the signal is taken as the timing instant defining the end of one period and the start of the following one [49, 56]. Superimposed noise causes a timing uncertainty of the reference level transition which is called *clock jitter* or *aperture jitter* [43]. This is shown in fig. 3.1(a) where the clock jitter is identical for the rising and falling edges of a square wave signal. Using one rising edge as the reference, the timing uncertainty of subsequent transitions relative to the reference increases since the jitter accumulates over several clock cycles. This is indicated in fig. 3.1(b). It leads to the definition of *accumulated jitter* [43]. Thus, it depends on the number of measured clock periods. Considering the accumulated jitter after one clock cycle leads to *period jitter* [43]. It is also known as *cycle-to-cycle jitter*, *edge-to-edge jitter* and *cycle jitter* [43, 49]. In the following sections, each jitter form is derived and its measurement capability is discussed.

3.1 Clock Jitter

The clock jitter has been introduced in fig. 3.1(a) by means of a periodic square wave signal. This can be generalized for an arbitrary clock signal form $s(t) = s(t + T_p)$ of period T_p. Since a real clock signal is always limited and continuous, it can be represented by a Fourier

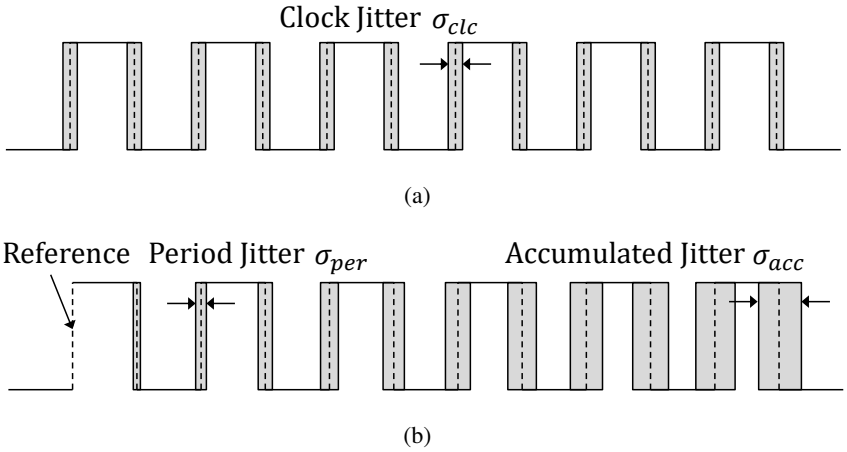

Figure 3.1: (a) Clock jitter as uncertainty of transition instants from HIGH to LOW and vice versa of a square wave signal. (b) Using one rising edge as reference, the timing uncertainty of following transitions accumulates over the clock cycles into an accumulated jitter. The timing uncertainty after one cycle is called period jitter.

series as [66]

$$s(t) = \frac{I_0}{2} + \sum_{k=1}^{\infty} \left(I_k \cos(k\omega_T t) + Q_k \sin(k\omega_T t) \right) \tag{3.1}$$

$$= \frac{I_0}{2} + \sum_{k=1}^{\infty} A_k \sin\left(k\omega_T t + \phi_k\right) \qquad \text{with} \tag{3.2}$$

$$A_k = \sqrt{I_k^2 + Q_k^2} \qquad \text{and} \tag{3.3}$$

$$\tan(\phi_k) = \frac{I_k}{Q_k}. \tag{3.4}$$

Here, the Fourier coefficients are defined by [66]

$$I_k = \frac{2}{T_p} \int_0^{T_p} s(t) \cos(k\omega_T t) \mathrm{d}t \qquad \text{and} \tag{3.5}$$

$$Q_k = \frac{2}{T_p} \int_0^{T_p} s(t) \sin(k\omega_T t) \mathrm{d}t \tag{3.6}$$

where $\omega_T = 2\pi/T_p$ is the angular frequency of the clock signal. Now, jitter can be taken into account by adding a time-dependent uncertainty $\tau(t)$ to the time variable $t \rightarrow t+\tau(t)$ in eq. (3.2). Afterwards, it can be seen that the jitter is in the argument of every sinusoid of the Fourier series and it is sufficient to study (or measure) the jitter of one harmonic. Therefore, the following jitter analysis is performed for a sinusoid illustrated in fig. 3.2. The zero-crossing with a positive slope corresponds to the transition instant for jitter investigation. For a sinusoid, the signal period results from two subsequent zero-crossings. In fig. 3.2

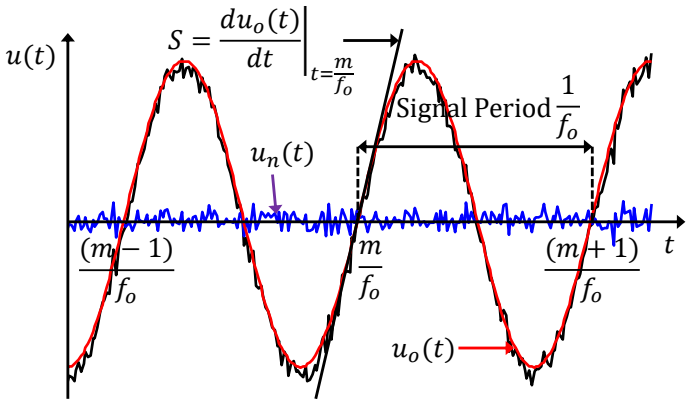

Figure 3.2: The distance of zero-crossings with the positive slope S defines the period $1/f_o$ of an oscillating signal $u(t)$ which is a superposition of an ideal signal $u_o(t)$ illustrated in red and a noise signal $u_n(t)$ shown in blue.

these zero-crossings are, for example, at the time instants m/f_o and $(m+1)/f_o$ where $f_o = \omega_T/2\pi$ is the nominal frequency of the oscillating signal $u(t)$ and m is an integer. The ideal signal $u_o(t) = A \cdot \sin(2\pi f_o t)$ is shown in red, while the noisy signal $u(t) = u_o(t) + u_n(t)$ is plotted in black. Superimposed noise $u_n(t)$ affects the transition instants by shifting the zero-crossings in time which corresponds to timing jitter [56]. To show this, a normal (or Gaussian) distribution for the voltage noise $u_n(t)$ is assumed with the probability density function [67]

$$p(u_n) = \frac{1}{\sqrt{2\pi}u_{n,rms}} e^{-\frac{u_n^2}{2u_{n,rms}^2}} \tag{3.7}$$

where $u_{n,rms}$ is the voltage noise standard deviation.

In fig. 3.2, the slope $S = \mathrm{d}u_o(t)/\mathrm{d}t|_{t=m/f_o}$ at the positive zero-crossing threshold of an oscillating signal is introduced. Using a linear approximation, the time instant of the transition point will be shifted by $\sigma = u_n/S$ due to the superimposed voltage noise u_n [43, 56]. Using this relation in eq. (3.7) to replace u_n leads to [67]

$$p(\sigma) = \frac{1}{S} \frac{1}{\sqrt{2\pi}\frac{u_{n,rms}}{S}} e^{-\frac{\sigma^2}{2\frac{u_{n,rms}^2}{S^2}}}. \tag{3.8}$$

It describes the probability density distribution of the timing uncertainty σ of the transition instant for a signal with the slope S at the threshold level. Hence, the standard deviation $\sigma_{clc} = u_{n,rms}/S$ of the transition instant due to superimposed Gaussian noise corresponds to clock jitter. Obviously, the jitter shrinks for a higher slope S for the same amount of noise $u_{n,rms}$.

Jitter measurement precision in the time domain by oscilloscopes is limited by the inherent noise sources of the used device. In contrast, frequency domain measurements enable

ultra-low jitter measurements and the opportunity of localization of certain noise sources regarding their spectral impact. For this purpose, a frequency domain interpretation of jitter is provided in the following.

Clock signals are usually derived from a PLL using ring or LC oscillators which are locked to an externally provided reference [43] as mentioned in section 2.3. Real oscillators differ from the ideal case of a sinusoid with a constant nominal frequency f_o. Due to inherent noise sources within the oscillator, the derived sinusoid contains additional phase noise $\varphi_n(t)$ leading to the relation [43]

$$u(t) = (A + a_n(t)) \cdot \sin\left(2\pi f_o t + \varphi_n(t)\right) \tag{3.9}$$

$$= (A + a_n(t)) \cdot \sin\left(2\pi f_o (t + \sigma(t))\right) \tag{3.10}$$

where A is the nominal amplitude of the oscillating signal $u(t)$ and $a_n(t)$ represents the superimposed amplitude fluctuations within the clock signal path. The phase noise in the argument of the sine wave in eq. (3.9) is related to a continuous timing uncertainty by

$$\sigma(t) = \frac{\varphi_n(t)}{2\pi f_o}. \tag{3.11}$$

Assuming a small phase noise ($\varphi_n(t) \ll 2\pi$) in eq. (3.9) and using a first order Taylor approximation for $u(t)$ around the time instant t leads to [43]

$$u(t) = \underbrace{A \sin\left(2\pi f_o t\right)}_{u_o(t)} + \underbrace{a_n(t) \sin(2\pi f_o t)}_{u_{n,a}(t)} + \underbrace{A \cos\left(2\pi f_o t\right) \varphi_n(t)}_{u_{n,\varphi}(t)} \tag{3.12}$$

where the beating of amplitude and phase noise has been neglected. The first term is the ideal signal $u_o(t)$. The amplitude fluctuations result in the superimposed voltage noise $u_{n,a}(t)$, while the last term of this expression represents the superimposed voltage noise $u_{n,\varphi}(t)$ due to phase noise $\varphi_n(t)$. This phase-noise-induced voltage error is identical to the previously introduced approximation in fig. 3.2 for the zero-crossings where the error $u_n|_{u_o=0} = \sigma \cdot S$ is derived by the slope $S = A \cdot 2\pi f_o$ multiplied by the timing uncertainty $\sigma = \varphi_n / 2\pi f_o$ resulting from phase noise. For a single frequency phase noise $\varphi_n(t) = A_\varphi \cos(2\pi f_n t)$ in eq. (3.12) the corresponding voltage noise

$$u_{n,\varphi}(t) = A A_\varphi \frac{1}{2} \left[\cos\left(2\pi(f_o + f_n)t\right) + \cos\left(2\pi(f_o - f_n)t\right)\right] \tag{3.13}$$

consists of two harmonics placed symmetrically around the oscillator frequency in a distance given by the phase noise frequency f_n [49]. This result is valid for a small modulation index $A_\varphi \ll 1$ which is also called the *narrowband frequency modulation (FM) approximation* [68]. It is a typically accurate approximation for oscillator / PLL systems and applications [49].

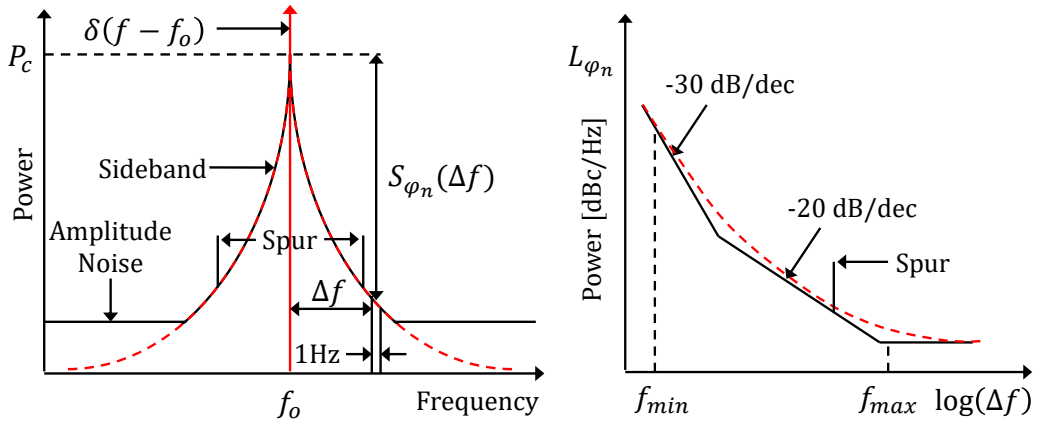

(a) (b)

Figure 3.3: (a) Power of the nominal oscillator frequency f_o is leaking out to neighboring frequencies creating sidebands. For higher offset frequencies, the power in the sidebands is negligible compared to broadband amplitude noise. (b) A single-sideband $L_{\varphi_n}(\Delta f)$ is usually measured within an offset frequency range f_{min}-f_{max}. It has characteristic frequency dependencies for certain offset frequency regions. Single dominant noise sources induce spectral spurs.

For broadband FM with $A_\varphi > 1$, the first order Taylor approximation is not valid in eq. (3.12) and higher orders have to be included. In this case, a phase-noise frequency f_n induces harmonics at multiple frequency offsets from the oscillator frequency $f_o \pm k f_n$ and their amplitudes are scaled by Bessel functions of the first kind [68]. Hence, phase noise can also be interpreted as power "leaking out" from the nominal frequency f_o to neighboring frequencies. While the spectrum of an ideal sinusoid corresponds to a Dirac function at the frequency f_o, real oscillators have a finite power amplitude for the carrier frequency and sidebands around it resulting from phase noise $\varphi_n(t)$. These are illustrated in fig. 3.3(a). This relation can also be derived from the third term in eq. (3.12). In the frequency domain, it results in a Dirac-function from the cosine function placed at the oscillator frequencies f_o convolved with the phase noise spectrum $S_{\varphi_n}(f)$ appearing as sidebands [43]. The double-sided phase noise power spectral density (PSD) is defined as [40, 69]

$$S_{\varphi_n}(f) = \lim_{T\to\infty} \frac{1}{T} \left|\mathcal{F}_T\{\varphi_n(t)\}(f)\right|^2 \tag{3.14}$$

$$\approx \frac{1}{T} \left\langle \left|\mathcal{F}_T\{\varphi_n(t)\}(f)\right|^2 \right\rangle \tag{3.15}$$

with the finite-time Fourier transform of a power signal $u(t)$ defined as [40, 69]

$$U_T(f) = \mathcal{F}_T\{u(t)\}(f) = \int_{-\infty}^{\infty} \sqcap_T \cdot u(t) e^{-j2\pi f t} \mathrm{d}t = \int_{-\frac{T}{2}}^{\frac{T}{2}} u(t) e^{-j2\pi f t} \mathrm{d}t. \tag{3.16}$$

It results from the Fourier transform in eq. (2.4) if the spectral components of a signal $u(t)$ are analyzed only within a time window $\sqcap_T(t)$. The introduction of the finite-time PSD is due to the infinite energy of the power signal $\varphi_n(t)$ for $T \to \infty$. The calculation of the PSD from a finite-time Fourier transform would lead to a finite-time PSD. In practice, therefore, multiple measurements are performed over the finite-time intervals T and the averaged value corresponds to the approximation of the real power spectral density $S_{\varphi_n}(f)$. This is indicated by the expectation value $\langle \dots \rangle$ in eq. (3.15).

The phase noise sidebands are symmetric around the carrier since the higher and lower offset frequencies are scaled by the same factor in eq. (3.13). A similar relation can be derived for the sidebands from amplitude noise if its contribution $u_{n,a}(t)$ in eq. (3.12) is expressed similar to eq. (3.13). However, if significant amplitude noise is present, its sidebands interact with the sidebands from phase noise causing an asymmetry of the upper and lower sideband levels [70]. It results from the different phase relations of the upper and lower sidebands for amplitude and phase noise thanks to the sine and cosine functions in eq. (3.12). Usually, this effect can be neglected and the sidebands can be considered symmetric as indicated in fig. 3.3(a).

A typical oscillator phase noise spectrum has regions with certain characteristic frequency dependencies which is indicated in the single-sideband (SSB) phase noise PSD $L_{\varphi_n}(f)$ in fig. 3.3(b). At low frequency offsets, the phase noise decreases with the slope $-30\,\text{dB/dec}$ in a logarithmic plot due to up-conversion of flicker noise [43, 51, 53, 56]. For higher offset frequencies, a slope of $-20\,\text{dB/dec}$ dominates resulting from thermal noise within the oscillator [43, 51, 53, 56]. Finally, there is a region of flat noise PSD stemming from the broadband amplitude noise $u_{n,a}(t)$ superimposed to the ideal signal $u_o(t)$ in eq. (3.12). Its main contribution stems from buffers in the clock path [43]. A huge advantage of frequency domain measurements is the possible identification of isolated noise sources. These induce strong phase noise for specific offset frequencies relative to the carrier and can be identified in the spectrum as *spurs*. This is indicated in fig. 3.3. Spurs result from deterministic timing uncertainties and limit the SFDR performance. Typical origins are skew in time-interleaved devices, crosstalk from nearby circuits, power supply and substrate noise, improperly designed PLLs [43] or vibrations [68].

Based on the introduced connection between clock jitter and phase noise, it is possible to calculate the jitter from a measured phase-noise spectrum. The mathematical relation can be derived from eq. (3.11). Using Parseval's theorem, the clock jitter as the standard deviation of the timing uncertainty σ results in [43]

$$\sigma_{clc} = \sqrt{\langle \sigma^2 \rangle} = \frac{1}{2\pi f_o} \sqrt{\langle \varphi_n^2 \rangle} = \frac{1}{2\pi f_o} \sqrt{\int_{-\infty}^{\infty} S_{\varphi_n}(f) \mathrm{d}f}. \tag{3.17}$$

Here, $S_{\varphi_n}(f)\mathrm{d}f$ is the double-sided phase noise PSD defined in eq. (3.14) within the frequency interval $\mathrm{d}f$. It is convenient to replace the phase noise PSD in eq. (3.17) by the SSB phase noise PSD $L_{\varphi_n}(f)$ since this is actually measurable by an electrical spectrum analyzer (ESA). It is defined as the noise power within 1 Hz bandwidth per Hz relative to the oscillator carrier frequency power $P_c(f_o)$ for an offset frequency Δf. This is illustrated in fig. 3.3(b). According to the definition, the SSB phase noise is given in dBc/Hz. Moreover, it is related to the phase noise PSD by [43, 56, 68]

$$L_{\varphi_n}(f) = \frac{S_{\varphi_n}(f)}{2}. \tag{3.18}$$

In real measurement systems, the SSB phase noise is only measured in a certain frequency range. Therefore, the often-used formula for clock jitter calculation from phase noise measurements is [43]

$$\sigma_{clc} = \frac{1}{2\pi f_o}\sqrt{\int_{f_{min}}^{f_{max}} 2 \cdot L_{\varphi_n}(f)\mathrm{d}f}. \tag{3.19}$$

In general, the lower offset frequency f_{min} depends on the application. For example, in telecommunications, this lower limit often corresponds to the symbol rate [43]. In video, it corresponds to the horizontal refresh rate when the signal is synchronized [43]. Furthermore, it is defined by the International Telecommunication Union that long-term variations of significant instants of a timing signal from their ideal positions with a frequency smaller than 10 Hz are called *wander* [71]. Only higher offset frequencies are referred to jitter. The upper limit is given by the system bandwidth [43]. The lower frequency constraint in eq. (3.19) is actually far more important. Using $f_{min} \to 0$ Hz, the integration is unbounded and the jitter is infinite thanks to the $1/f^3$ noise characteristic close to the carrier. It represents the frequency drift with time due to noise. In this case, the phase will diverge representing a random walk process [43].

The jitter calculation from the phase noise spectrum in certain offset frequencies also enables the suppression of isolated spurs by neglecting these specific frequencies in the spectrum. These spurs may result from external influences and do not represent the actually investigated device. Moreover, the impact of deterministic noise sources can be investigated by calculating the jitter in the phase noise offset frequency range around the spurs. This distinction is not possible in the time-domain.

In fully realized high-speed ADCs, the clock jitter can be determined from the known relationship between the ENOB and the signal frequency. According to eq. (2.17), clock jitter limits the ENOB for higher input frequencies. This can be used in a measurement if other noise impacts can be excluded. For example, in [46] harmonics had to be removed before the clock jitter of 240 fs was measured.

Alternatively, a digitized harmonic can be fitted to an ideal sinusoid and the deviations can be referred to the jitter if other noise sources are negligible. This is also known as modulo-time plot analysis [72]. In this way, a clock jitter of $250\,\mathrm{fs}$ was measured in [46] while in [27, 28] a clock jitter of $60\,\mathrm{fs}$ was determined.

3.2 Period Jitter

Phase noise $\varphi_n(t)$ has been introduced as a *continuous* stochastic process modulating the oscillator phase or the nominal frequency f_o by its time derivation. If this signal is used as a clock to trigger electronic circuits, the phase noise induces a timing uncertainty σ of the switching instant. Regarding fig. 3.2, its impact is only relevant at the transition instants k/f_o. Considering only the time-discrete switching instants, its timing uncertainty results in a *discrete* stochastic process [56]. As introduced in fig. 3.1, the period jitter is the standard deviation of a transition instant relative to the previous one [43, 56]. Its mean value corresponds to the ideal clock cycle. The period jitter is important for digital applications, such as microprocessors, where the correct data processing is highly dependent on the appearance of one clock edge relative to the previous one [49]. In the following, a link is created between the continuous phase noise and the discrete period jitter. For one clock cycle the phases for both transition instants in eq. (3.9) result in

$$2\pi f_o t_1 + \varphi_n(t_1) = 0 \qquad \text{and} \tag{3.20}$$

$$2\pi f_o t_2 + \varphi_n(t_2) = 2\pi. \tag{3.21}$$

The overall time period $\Delta t = t_2 - t_1 = 1/f_o + \sigma$ represents one clock cycle $1/f_o$ plus a timing uncertainty σ. Using this relation in the differential of eqs. (3.20) and (3.21) leads to [56, 67]

$$\sigma = \frac{1}{2\pi f_o}(\varphi_n(t_1) - \varphi_n(t_2)). \tag{3.22}$$

Then, the variance of this timing uncertainty results in the squared period jitter [67]

$$\sigma_{per}^2 = \langle\sigma^2\rangle = \frac{1}{4\pi^2 f_o^2}\left(\langle\varphi_n^2(t_1)\rangle - 2\langle\varphi_n(t_1)\varphi_n(t_2)\rangle + \langle\varphi_n^2(t_2)\rangle\right). \tag{3.23}$$

For a stationary process $\varphi_n(t)$, the variance is time-independent. Using Parseval's theorem, the phase noise variance can be calculated by

$$\langle\varphi_n^2(t_1)\rangle = \langle\varphi_n^2(t_2)\rangle = \langle\varphi_n^2(t)\rangle = \int_{-\infty}^{\infty} S_{\varphi_n}(f)\mathrm{d}f. \tag{3.24}$$

The middle term of eq. (3.23) corresponds to the autocorrelation function (ACF) [73]

$$\langle\varphi_n(t_1)\varphi_n(t_2)\rangle = R_{\varphi_n}(t_2 - t_1) = R_{\varphi_n}(\Delta t) = \int_{-\infty}^{\infty} S_{\varphi_n}(f)\cos(2\pi f\Delta t)\mathrm{d}f. \tag{3.25}$$

The cosine function within the integral results from the phase noise characteristic. If $\varphi_n(t)$ is a real process, then $R_{\varphi_n}(\Delta t)$ is real and even. Hence, $S_{\varphi_n}(f)$ is also real and even [73]. Using eqs. (3.24) and (3.25) in eq. (3.23) results in [43, 52, 56, 67]

$$\sigma_{per}^2 = \frac{1}{4\pi^2 f_o^2} \int_{-\infty}^{\infty} S_{\varphi_n}(f) \cdot 4\sin^2(\pi f \Delta t)\mathrm{d}f. \tag{3.26}$$

Here, the relation $2\sin^2(\pi f \Delta t) = 1 - \cos(2\pi f \Delta t)$ [66] has been used. The filtering of the phase noise PSD within the integral results from phase noise sampling after one clock cycle $\Delta t = 1/f_o$ and $4\sin^2(\pi f/f_o)$ is the corresponding transfer function [43, 49, 56]. Eq. (3.26) is the general link between period jitter and phase noise [56]. In the previous section it was mentioned that phase noise can only be measured as an SSB within a certain frequency interval. Therefore, using eq. (3.18) leads to [43, 56]

$$\sigma_{per} = \frac{1}{2\pi f_o} \sqrt{\int_{f_{min}}^{f_{max}} 2L_{\varphi_n}(f) \cdot 4\sin^2(\pi f \Delta t)\mathrm{d}f}. \tag{3.27}$$

It is also possible to measure the period jitter in the time domain. In this case, an oscilloscope is triggered by one rising edge while measuring the deviation of the subsequent one from the mean value. Assuming a normal distribution for the jitter, the probability distribution function of the sampling errors is given in eq. (3.7). Fitting this equation to a histogram of the measured voltage levels around the zero-crossings leads to the period jitter. Time domain measurement precision is restricted to jitter levels in the picosecond range.

3.3 Accumulated Jitter

The accumulated jitter σ_{acc} can be derived from the period jitter by extending the number of clock cycles $\Delta t = N_{clc}/f_o$ in eq. (3.27) [43, 67]. Obviously, the accumulated jitter is affected by the measurement time and accumulates over the clock cycles. For uncorrelated noise, the accumulated jitter increases with $\sqrt{N_{clc}}$ corresponding to a random walk characteristic [49, 52, 56]. For correlated noise sources jitter accumulates with N_{clc} [52, 56]. For example, substrate and supply noise show correlation characteristics [52]. Furthermore, low frequency noise, such as flicker noise, induces a correlation between multiple clock cycles [52, 56].

Accumulated jitter can also be measured in the time domain. Here, the rms variation of a high number of consecutive clock periods is measured. But the jitter measurement precision remains more accurate in the frequency domain.

3.4 Phase Noise Measurement

In the previous sections, different jitter definitions have been introduced and links were created between jitter and phase noise. The motivation for this is the higher precision of phase noise measurements in the frequency domain compared to direct jitter measurements in the time domain. In the following, the phase noise measurement principle is introduced.
In eq. (3.9), the harmonic $u(t)$ is accompanied by amplitude and phase noise fluctuations represented by $a_n(t)$ and $\varphi_n(t)$. State-of-the-art electrical spectrum analyzers (ESAs) use a demodulation method to increase the sensitivity of phase noise measurements. Here, a local oscillator is locked by a PLL to the input frequency f_o and its output $u_{LO} = A_{LO}\cos(2\pi f_o t + \theta)$ is mixed with the input signal $u(t)$ from eq. (3.9). The mixer output

$$u_{mix}(t) = \frac{A_{LO}}{2}(A + a_n(t))\left[\sin(\varphi_n(t) - \theta) + \sin(4\pi f_o t + \varphi_n(t) - \theta)\right] \tag{3.28}$$

is filtered afterwards by a low pass filter to get rid of the high-frequency component represented by the sinusoid with the doubled input frequency $2f_o$ in the argument. For phase noise measurements, the constant phase between the input signal and the PLL output is set to $\theta = 0$. The factor A_{LO} includes the amplitude of the local oscillation, the mixer conversion constant and the gain of the low pass filter. The usual case of small fluctuations of the amplitude $a_n(t) \ll A$ and the phase $\sin(\varphi_n(t)) \approx \varphi_n$ is assumed. In this case, the filter output results in [68]

$$u_{LPF}(t) = \frac{A_{LO}A}{2}\varphi_n(t) = K_\varphi \varphi_n(t). \tag{3.29}$$

Thus, the output is linear proportional to the small phase fluctuation and K_φ is the phase detector constant given in [V/rad]. Considering a zero mean value for the noise signal, the ESA measures the rms voltage spectral density in $\mathrm{V}/\sqrt{\mathrm{Hz}}$ by

$$u_{LPF,rms}(f) = \sqrt{\frac{\left\langle \frac{1}{T}\int_0^T u_{LPF}^2(t)\mathrm{d}t \right\rangle}{B_w}} \tag{3.30}$$

over a time interval T. The offset frequency f is chosen as the center frequency of the narrow measurement bandwidth B_w. A more precise approximation of the statistical value $u_{LPF,rms}(f)$ is achieved by performing multiple measurements using the expectation value which is indicated in eq. (3.30) by $\langle \ldots \rangle$. Afterwards, the phase noise PSD can be calculated by [68]

$$S_{\varphi_n}(f) = \left[\frac{u_{LPF,rms}(f)}{K_\varphi}\right]^2. \tag{3.31}$$

Scanning the offset frequency f over the desired frequency range leads to the phase noise PSD. Finally, the SSB phase noise $L_{\varphi_n}(f)$ results from eq. (3.18).
By means of demodulation and filtering, the background carrier is removed. Using narrowband filters while scanning through the large frequency range minimizes the measurement system noise contribution and enhances the ESA dynamic range [68].
The demodulation and filtering process by the ESA is always accompanied by noise. The origins are the PLL components such as the VCO or the phase detector, the low pass filter and the amplifier which is usually embedded for signal enhancement. These noise contributions limit the measurement sensitivity. State-of-the-art ESAs use cross-correlation techniques to suppress this noise [74]. In this case, the measured input signal is split into two symmetrical paths and each channel is demodulated and filtered by separate devices. The noise sources within the ESA in each path are uncorrelated. Ideally, these noise contributions can be removed by cross-correlations while the correlated components from the input signal add up. In reality, a measurement sensitivity improvement of up to 20 dB can be achieved by 20000 averages of individual cross-correlation measurements [75].

3.5 Jitter Measurement of Optical Pulse Trains

The motivation for photonic ADCs results from the ultra-low jitter performance of mode-locked lasers which will be discussed in section 5.1. In this section, the jitter measurement of optical pulse trains is introduced. It is based on a phase noise measurement of an arbitrary harmonic of the detected electrical spectrum. The principle was shown first by von der Linde in [19]. Here, the basics are recapitulated since the understanding is important for the jitter characterization of MLLs in the following chapters.
The intensity of an ideal optical pulse train can be written as

$$I_0(t) = \sum_{\mu=-\infty}^{\infty} I_p(t - \mu T_p) = I_p(t) * \delta_{T_p}(t). \tag{3.32}$$

It corresponds to a sum of individual pulse intensity profiles $I_p(t)$ separated by the repetition period T_p. Real optical pulse trains show fluctuations of the amplitude as well as the period. This can be taken into account by

$$I(t) = \sum_{\mu=-\infty}^{\infty} (1 + a_n(t)) \cdot I_p(t - \mu T_p + \sigma(t)) \tag{3.33}$$

where each pulse is shifted in time by $\sigma(\mu T_p)$ relative to the ideal period. The jitter $\sigma(t)$ is considered slowly varying compared to the pulse width. Relative amplitude fluctuations correspond to pulse energy fluctuations and are taken into account by $a_n(t)$. Using a Taylor

approximation of the first order leads to

$$I(t) = \sum_{\mu=-\infty}^{\infty} \left[(1 + a_n(t)) \cdot I_p(t - \mu T_p) + \frac{\mathrm{d}}{\mathrm{d}t} I_p(t - \mu T_p) \cdot \sigma(t) \right]$$
$$= (1 + a_n(t)) \cdot I_0(t) + \frac{\mathrm{d}}{\mathrm{d}t} I_0(t) \cdot \frac{\varphi_n(t)}{2\pi f_T} \tag{3.34}$$

where the jitter $\sigma(t)$ has been replaced by its relation to the phase noise $\varphi_n(t)$ from eq. (3.11) with $f_T = 1/T_p$ as the pulse train repetition rate. The pulse train intensity spectrum can be derived from the Fourier transform of eq. (3.34). This is shown in appendix A and results in

$$S_I(f) = f_T^2 \sum_{\mu=-\infty}^{\infty} S_{I_p}(\mu f_T) \cdot$$
$$\left[\delta(f - \mu f_T) + \frac{1}{(2\pi)^2} S_{a_n}(f - \mu f_T) + \frac{\mu^2}{(2\pi)^2} S_{\varphi_n}(f - \mu f_T) \right]. \tag{3.35}$$

Here, the delta comb scaled by the pulse intensity envelope spectrum $S_{I_p}(f)$ corresponds to the ideal spectrum. The amplitude noise spectrum $S_{a_n}(f)$ affects this ideal spectrum by constant sidebands around each harmonic of the delta comb, while the sidebands from the phase noise spectrum $S_{\varphi_n}(f)$ are scaled by the square of the harmonic order μ. It is possible to distinguish between the noise sources thanks to the μ^2 dependence. For $\mu = 0$, the sidebands stem only from amplitude fluctuations, while for a high harmonic order $\mu \gg 1$, the phase noise impact on the sidebands dominates. When the optical pulse train is detected by a photodiode, the resulting electrical spectrum

$$S_{I,det}(f) = |G_{PD}(f)|^2 S_I(f) \tag{3.36}$$

is scaled by the photodiode transfer function $|G_{PD}(f)|^2$. But since the delta comb and the sidebands are only scaled and not distorted by the photodiode transfer function, the sidebands can be measured by an ESA and referred to the optical pulse train. Therefore, although the photodiode impulse response broadens the detected optical pulses, the noise characteristics are not affected and it is possible to identify the jitter of optical pulse trains by means of phase noise measurements at an arbitrary harmonic of the detected electrical spectrum.

Instead of measuring the sideband power of several harmonics to distinguish between amplitude and phase noise like proposed in [19], modern phase noise measurements are performed at a single harmonic. The used RF demodulation method, introduced in section 3.4, enables a much higher phase noise measurement sensitivity and simultaneously suppresses superimposed amplitude noise. The choice at which harmonic the measurement is performed is very important. In reality, the ESA has a limited phase noise measurement sensitivity. Therefore, a high harmonic order should be used where the phase noise

level rises over this sensitivity limit due to the μ^2 dependence in eq. (3.35). But higher harmonics are stronger attenuated by the photodiode transfer function and the phase noise measurement sensitivity is higher for higher input power. The optimum harmonic order is a trade-off between these two effects. The measurement sensitivity limit of the ESA results especially from the intrinsic phase noise of the embedded VCO which has to be negligible compared to the device under test (DUT). It can be a very critical requirement. Moreover, limits for the RF demodulation method are set by non-linearities within the photodiode. Saturation effects induce amplitude-to-phase noise conversion limiting the capability of jitter measurements [76, 77]. Nevertheless, the RF demodulation method enables timing jitter measurements down to $\sim 10\,\text{fs}$. This was achieved in [78, 79] at the first harmonic of a $10\,\text{GHz}$ MLL or in [80] at the sixtieth harmonic of a $100\,\text{MHz}$ MLL.

One method to overcome this limit is based on heterodyne beating of long and short wavelength tails respective to the center wavelength of two nearly identical free-running MLLs in the optical domain [62]. Photodiodes detect the two at quadrature pair-wise interfering spectral components. Afterwards, the two heterodyne beat notes are low pass filtered and fed into a phase detector at quadrature. The output is low pass filtered and amplified before it is measured by an ESA. Furthermore, this discrimination signal serves for synchronization of the MLL repetition rates by means of a PLL. The locking bandwidth represents the lower frequency limit of the phase fluctuations. The huge advantage of this method is the insensitivity of the discrimination signal towards amplitude noise [62]. Linear high power photodiodes are still necessary to avoid amplitude-to-phase noise conversion from saturation effects. The superior sensitivity stems from mixing in the optical domain where the interfering optical frequencies are much higher than the detected harmonics of the electrical spectrum. It was shown in [62] that this method is able to measure timing jitter in the low attosecond range. An obvious disadvantage is the need of a second, nearly identical MLL.

Another approach is based on balanced optical cross-correlation in the time domain [81, 82]. It is based on group delay difference generation of two orthogonal polarized pulses and second harmonic generation by a type-II phase-matched non-linear crystal [29, 82]. Here, the single crystal is placed within two identical cross-correlation paths with a stable time delay element in between. A solution with two nearly identical non-linear crystals for sum frequency generation is also possible [81]. Balanced photodetection of the two cross-correlator output signals is immune towards intensity noise and only the timing information is extracted [81, 82]. This method overcomes the photodetector limitations and provides a higher sensitivity compared to electronic schemes [81, 82]. Here, the sensitivity enables timing jitter measurements of MLLs in the low attosecond regime [61, 63, 64, 65]. The spectral density of the jitter can be calculated by the measured voltage noise spectral density and

the measured slope of the cross-correlation signal [82]. The disadvantage is the need of a reference MLL with lower timing jitter. Furthermore, the repetition rate of the laser under test has to be either equal to [29] or a multiple [83] of the repetition rate of the reference laser. The pulse train correlation of two MLLs is called the *timing-detector method* [82]. Here, the reference MLL is locked to the repetition rate of the laser under test by a PLL. The error signal can result either from balanced optical cross-correlation or from microwave mixing of photodetected harmonics. The PLL bandwidth corresponds to the lower measurable frequency of the phase noise PSD. In this case, the jitter of both MLLs is measured.
The need of a reference MLL is avoided by the *timing-delay method* [82]. Here, the pulse train from the laser under test is split and correlated with a relative delay. In this case, the fiber link of the delay path has to be timing-stabilized to avoid measuring jitter from acoustic noise, thermal drifts and mechanical stress within the fiber [30]. The inverse of the fiber delay results in the lower measurable frequency of the phase noise PSD, assuming a lower link stabilization bandwidth. For example, the measurement of jitter frequencies down to $10\,\mathrm{kHz}$ requires a ca. $10\,\mathrm{km}$ long dispersion compensated and polarization maintaining fiber [29]. Fiber non-linearities form a higher boundary for the pulse energy and hence limit the jitter sensitivity at the cross-correlator [30]. The self-referenced correlation with a certain delay leads to a filter function affecting the measured spectrum equivalent to the filter function in eq. (3.26). It has to be corrected afterwards as was done in [82]. Link stabilization and the distorted jitter spectrum represent the disadvantages of the timing-delay method. The advantage is that the actual timing jitter of the laser under test is measured.
It should be noted that the shot noise of the balanced detected electronic signal is sufficiently low if the laser can provide enough power to generate a high power signal in the non-linear crystal. Obviously, the limited conversion efficiency of the cross-correlator is another fundamental resolution limit. The pulse width should be $\ll 1\,\mathrm{ps}$ to enhance the sum frequency generation through higher intensities. The balanced optical cross-correlation is convenient for sufficiently high pulse intensities which are provided by MLLs with repetition rates in the megahertz regime [61, 63, 64, 65, 81, 82, 84].

Chapter 4

Silicon Photonics Platform

Silicon (Si) has been used as the basic material for electronics integration since 1959 [1, 2, 3]. Since then, the IC performance has evolved simultaneously with its miniaturization which became popular as *Moore's law* [4]. Thanks to the matured IC fabrication technology, silicon became also interesting for optics integration. The pioneer work was done in the late 1980s [20, 85] and the early 1990s [21].

Silicon is nearly transparent for wavelengths $> 1100\,\text{nm}$ and, therefore, well suited for guiding the typical telecommunication wavelengths of $1300\,\text{nm}$ and $1550\,\text{nm}$. Its high refractive index (~ 3.5, in the near infrared) in comparison to air or a silicon dioxide (SiO_2) (~ 1.45, in the near infrared) cladding enables high light confinement and small waveguide bend radii. This is essential for miniaturization and fabrication of photonic integrated circuits (PICs). Here, fundamental limitations arise from the optical wavelength. Too small waveguide cross sections lead to an expansion of the field intensity out of the waveguide core. To circumvent this effect, the typical silicon waveguide size remains in the range of few hundreds of nanometers in height or width. Although the number of integrated photonic components can not compete with the number of integrated electronic components, its amount is absolutely sufficient for most applications. The PICs can be realized on a silicon-on-insulator (SOI) platform compatible with CMOS technology. A potential high volume production would decrease fabrication costs and may lead to a similar success story as for electronics. The integration of photonics and electronics on the same chip results in new applications. Furthermore, the superior performance of optics can improve electronics where its fundamental limitations are reached like in interconnects [86], clock distribution [11, 87] or high-speed ADCs [24, 88]. The prime applications for silicon photonics is often named as telecommunication and interconnects [86, 89].

The plasma dispersion effect is an important characteristic in silicon. Here, the real and imaginary part of the refractive index changes in dependence on the free carrier density

Figure 4.1: Local SOI formation: (a) SOI substrate with typical thicknesses of the silicon and the buried oxide layers. Both are locally removed and refilled with silicon. (b) Wafer with local SOI for photonics integration and local bulk silicon for electronics integration.

[85]. Therefore, by means of carrier injection or carrier depletion, light can be modulated in silicon. This is the dominant effect used to build integrated modulators since the linear electro-optic effect (Pockels effect) is absent in silicon due to its centro-symmetric crystal structure. The high third-order non-linearity in silicon in combination with small effective areas of silicon waveguides enable exploitation of non-linear effects such as four-wave mixing, stimulated Raman scattering, two-photon absorption, self-phase modulation or cross-phase modulation [90]. And this is possible on chip scale by means of PICs! As an interface between optics and electronics, fast photodiodes can be built by means of germanium (Ge) deposited on silicon waveguides [91], which is compatible with the CMOS fabrication process. Silicon is an indirect semiconductor and, therefore, unsuitable for light emission. But strained and properly doped germanium is considered a possible material to achieve light emission with the typical telecommunication wavelength of $1550\,\text{nm}$ [92] on silicon. Since it is the last missing component for the breakthrough of silicon photonics, it is often called the *holy grail* [93]. Until then, III-V semiconductors can be used for light generation [86, 89, 93] or other photonic components [89]. Two approaches are possible for the integration, namely a monolithic or a hybrid approach.

In the hybrid approach heterogeneously integrated III-V functionality on the SOI platform is used by means of molecular wafer bonding [89, 94]. III-V based modulators and of course lasers offer good characteristics for PICs but their CMOS compatible fabrication on an SOI platform remains challenging.

In this thesis, the monolithic photonic bipolar CMOS (BiCMOS) platform from IHP [95] was used to fabricate the devices which will be characterized in chapter 7. It combines high-performance BiCMOS technology with high-speed photonic devices in silicon. The photonic components are integrated by means of a local SOI approach [96], while electronics is realized in bulk silicon. The principle is shown in fig. 4.1 with typical dimensions for the upper silicon and the buried oxide layers. In this way, the interconnects between

electronics and photonics are shorter compared to the hybrid approach, which is beneficial for high-speed applications. Furthermore, the heat dissipation of high-speed electronics is much less critical on bulk silicon than on the thick buried oxide, which has a much lower thermal conductivity. At least, if a laser source is required for a PIC, a completely monolithic integration remains impossible. In this case, a III-V based laser, as the single component, can be flip-chip bonded to the silicon PIC [86].
Alternative platforms use polymer waveguides. But since it can not withstand the electronics fabrication temperatures, its use is limited to the uppermost layers when the ICs are finished. Silica-on-silicon based photonics is not compatible with electronics due to the high annealing steps at $1000\,^{\circ}\mathrm{C}$ [89, 97]. Furthermore, silica-based waveguides have large bend radii in the millimeter range prohibiting photonic integration on electronic ICs with typical sizes of few centimeters square [97]. Other waveguide alternatives can be silicon oxynitride (SiON), silicon nitride (Si_3N_4) [89, 97] or silicon mononitride (SiN) [11].
In summary, the preferred monolithic silicon photonics BiCMOS platform offers already a large toolbox of photonic components for the complex PIC design. In the next sections, the essential photonic components are introduced which are of interest for the photonic-assisted low jitter ADC design.

4.1 Fiber-Chip Interface

In telecommunication systems, light is guided in fibers with effective mode areas of $\sim 80\,\mu\mathrm{m}^2$. It is a huge mismatch to the typical effective mode areas of $\sim 0.1\,\mu\mathrm{m}^2$ of silicon waveguides. Therefore, a focusing device is necessary at the interface. The favored solution is a grating structure directly written on the waveguide. A schematic is shown in fig. 4.2(a). Here, the fiber is placed nearly perpendicular to the chip surface. By means of Bragg diffraction at a periodic structure, the diffracted light interferes constructively in one direction parallel to the chip surface focusing the light directly into a silicon waveguide. The Bragg condition gives the relationship between the optimum angle of incidence, the wavelength and the periodic refractive index variation or grating geometry, respectively. It is convenient to use a few degree deviation from a vertical fiber placement to suppress higher order diffraction directions. Other strategies to maximize the coupling efficiency are discussed in [98]. Usually, the optimum structure is found by extensive numerical simulations either by means of finite-difference time-domain methods, eigenmode expansion or finite-element methods. Here, the diffraction direction towards the fiber and the overlap between the diffracted field profile and the Gaussian fiber mode are optimized in terms of coupling efficiency. Larger grating thickness increases directionality [98, 99]. Apodization of the grating periods increases the mode overlap but remains challenging if very narrow

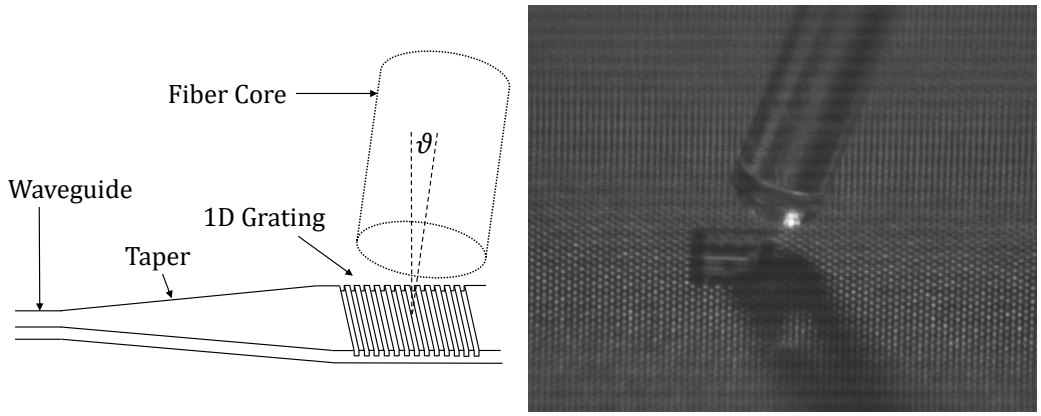

(a) (b)

Figure 4.2: (a) Basic configuration of fiber-to-chip coupling by a 1D grating. The fiber core is placed under an angle of incidence ϑ over the grating defined directly on the waveguide. A subsequent taper shrinks the waveguide widths. (b) Camera picture of a fiber placed above the grating coupler on chip.

slits have to be etched. Another option is to use a buried mirror under the grating to redirect transmitted light back to the grating [98]. This can be realized by a metal layer or a distributed Bragg reflector.

The simplest structure is a one-dimensional (1D) grating. Its basic configuration is shown in fig. 4.2(a), while fig. 4.2(b) shows a camera picture of a fiber placed above the grating coupler. The typical coupling loss of such structures is around 3 dB [96] and the wavelength dependence of the Bragg condition leads to a typical 3 dB bandwidth of $\sim$ 40 nm-60 nm [96, 98] for the telecommunication wavelengths of 1300 nm and 1550 nm. Using buried gold mirrors, a coupling loss of 1.6 dB was achieved but the fabrication process is not CMOS compatible [98]. In [100] a coupling loss of only 0.62 dB was achieved with a backside aluminum mirror and apodization. A CMOS compatible solution can be realized by an enhanced grating thickness. In this case, a coupling loss of 1.5 dB was measured in [99]. Although the 1D grating is very compact in size of $\sim$ 10 μm-by-10 μm, a subsequent adiabatic taper of $\sim$ 200 μm length remains necessary to narrow down the waveguide width. Such a taper can be avoided by a curved grating [98], which is also called a holographic lens [86]. Here, the diffracted light is focused on the waveguide cross section and achieves a coupling loss of only 1.5 dB [86]. An essential characteristic of such gratings is the polarization selectivity stemming from the high index contrast. 1D structures couple only one polarization into the transverse-electric (TE) mode of the silicon waveguide. Coupling of both polarizations is possible by superposition of two 1D gratings to a 2D grating, so that both polarizations are split and coupled into the TE modes of two orthogonal silicon waveguides [98]. The huge advantages of gratings are the possibility for wafer-scale testing

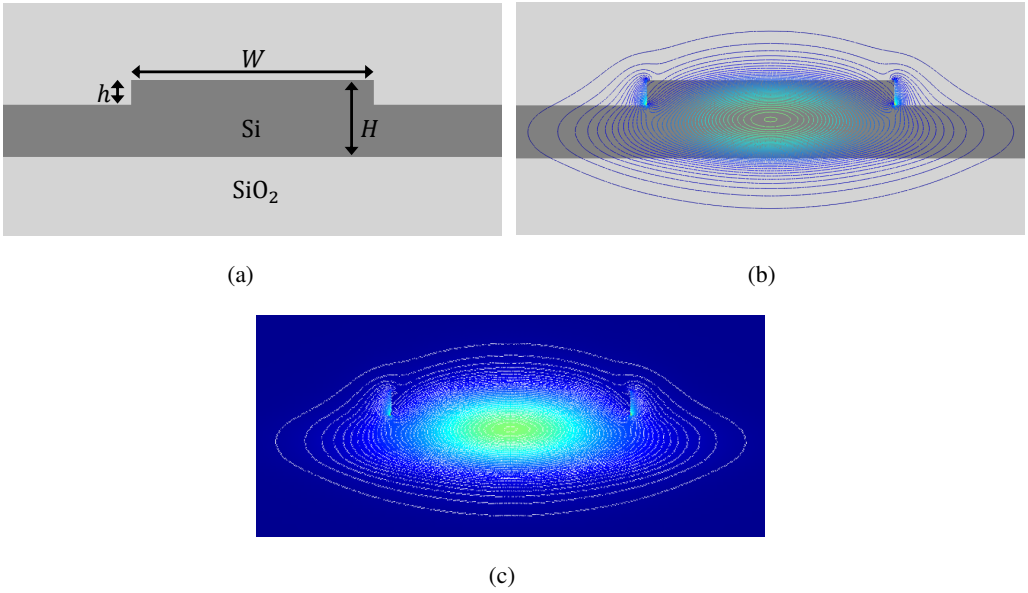

(a) (b)

(c)

Figure 4.3: Rib waveguide with silicon (Si) as the waveguide core and silicon dioxide (SiO_2) as over and under cladding material: (a) Waveguide geometry with the width W, the height H and the etch depth h (b) Equipotential lines of the electric field intensity of the fundamental quasi transverse-electric (TE) mode for a silicon rib waveguide with the dimensions $H = 220\,\text{nm}$, $W = 700\,\text{nm}$ and $h = 70\,\text{nm}$ for a wavelength of $1550\,\text{nm}$ (c) Electric field intensity distribution and equipotential lines of the fundamental quasi TE mode (simulated with JCMwave)

similar to electronics and the micro-meter alignment tolerance.
Another coupling method is to use an inverse taper structure for mode size conversion [97]. It can lead to a very low coupling loss of $< 0.5\,\text{dB}$ as long as the etching precision allows fabrication of taper tips of $< 150\,\text{nm}$ [97] which can be quite challenging. Here, the huge disadvantage is the lack of wafer-scale testing. For every device, the wafer needs to be diced and the facets have to be polished. However, this is a labor-intensive and costly solution.
In this thesis, 1D gratings have been used for the test structures in chapter 7.

4.2 Silicon Waveguides

Silicon is transparent for wavelengths $> 1100\,\text{nm}$ and optimal for guiding light of the typical telecommunications wavelengths of $1300\,\text{nm}$ and $1550\,\text{nm}$. Its high refractive index contrast towards air or cladding materials, such as silicon dioxide, results in a high confinement enabling small bend radii and device miniaturization. Fundamental limitations arise from the optical wavelength so that the confinement shrinks when waveguide cross sections become too small. In fig. 4.3(a), a schematic is shown of a *rib waveguide* with silicon as the waveguide core and silicon dioxide as over and under cladding material. If the silicon at the

waveguide edges is etched down to the buried oxide, the waveguide is called a *strip waveguide*. The electric field intensity and the effective refractive indexes of the guided modes are usually found by numerical simulations by means of finite-element, finite-difference or film mode matching methods. In fig. 4.3(b), the equipotential lines of the electric field intensity are shown for a waveguide geometry of $H = 220\,\text{nm}$, $W = 700\,\text{nm}$ and $h = 70\,\text{nm}$ and the wavelength $1550\,\text{nm}$. The simulation was performed by the finite-element-method-based software *JCMwave*. Here, the wavelength-dependent effective refractive index defined as

$$n_{eff} = \beta \frac{\lambda}{2\pi} \tag{4.1}$$

was found. λ is the vacuum wavelength of the propagating mode with the phase constant β. From the electric field intensity distribution in fig. 4.3(c) it can be seen that the field is mainly concentrated in the silicon waveguide core and corresponds to the fundamental quasi TE mode. The term quasi TE mode refers to the TE like characteristics but with non-negligible electric field component of the guided mode in propagation direction. This results from the high index contrast. The wavelength-dependent effective refractive index of the fundamental quasi TE mode is shown in fig. 4.4(a) for room temperature. The group index is defined as [101]

$$n_{grp} = n_{eff}(\omega) + \omega \frac{\mathrm{d}n_{eff}(\omega)}{\mathrm{d}\omega} = n_{eff}(\lambda) - \lambda \frac{\mathrm{d}n_{eff}(\lambda)}{\mathrm{d}\lambda} \tag{4.2}$$

and is also wavelength-dependent. Its temperature dependency for the fundamental quasi TE mode of the rib waveguide in fig. 4.3 is shown in fig. 4.4(b). Using the results in fig. 4.4(a) leads to $n_{grp}(1550\,\text{nm}) = 3.7743$ for room temperature, while $n_{grp}(1550\,\text{nm}) = 3.7879$ would result for $80\,^{\circ}\text{C}$. The group velocity dispersion (GVD) of the guided mode can be calculated by [101, 102]

$$\beta_2 = \frac{\mathrm{d}}{\mathrm{d}\omega}\left(\frac{1}{v_{gr}}\right) = \frac{2}{c_0}\frac{\mathrm{d}n_{eff}(\omega)}{\mathrm{d}\omega} + \frac{\omega}{c_0}\frac{\mathrm{d}^2 n_{eff}(\omega)}{\mathrm{d}\omega^2} \tag{4.3}$$

where $v_{gr} = c_0/n_{grp}$ is the group velocity and $\omega = 2\pi c_0/\lambda$ is the angular frequency. It results in $\beta_2(1550\,\text{nm}) = 1.87\,\text{ps}^2/\text{m}$ for the wavelength dependence at room temperature of fig. 4.4(a) and would be $\beta_2(1550\,\text{nm}) = 1.85\,\text{ps}^2/\text{m}$ at $80\,^{\circ}\text{C}$. The dispersion impact on pulse propagation can be estimated by the dispersion length [90]

$$L_D = \frac{\tau_o^2}{|\beta_2|^2}. \tag{4.4}$$

Considering a pulse width of $\tau_o = 1\,\text{ps}$ and the upper mentioned GVD, the dispersion length results in $L_D = 54\,\text{cm}$ which is much longer than silicon waveguides on chip. In this case, pulse broadening through dispersion can be neglected. For an ultra-short pulse width of

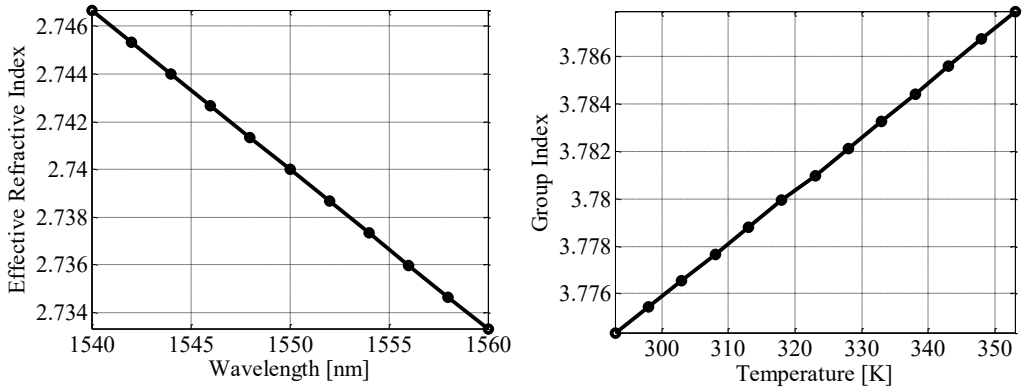

(a) (b)

Figure 4.4: Simulation results for the fundamental quasi TE mode of the rib waveguide from fig. 4.3 with the dimensions $H = 220\,\text{nm}$, $W = 700\,\text{nm}$ and $h = 70\,\text{nm}$: (a) Wavelength-dependent effective refractive index at room temperature (b) Temperature-dependent group index for a center wavelength of $1550\,\text{nm}$

$\tau_o = 100\,\text{fs}$ and the same GVD, the dispersion length results in $L_D = 0.54\,\text{cm}$ which corresponds to the conventional silicon waveguide length. In this case, dispersion can have an important impact on pulse propagation.

In silicon waveguides, the guided modes usually differ strongly in terms of their effective refractive and group indexes. It results in large mode dependent delays and is harmful for any high-speed application if more than one mode is excited. To circumvent these problems, it is convenient to shrink the waveguide size until only the fundamental mode is guided. Analytical formulas for the single-mode condition in large silicon rib waveguides can be found in [21]. For strip waveguides, the core dimension should be smaller than half-wavelength of the guided wave in silicon [97]. Smaller waveguides also enable smaller bend radii which is important for the integration of a large number of photonic components. Fortunately, the grating structures from section 4.1 couple the light solely into the fundamental quasi TE mode of the silicon rib waveguide from fig. 4.3.

Part of the electric field always spans out of the waveguide core into the cladding. This is shown by the equipotential lines in figs. 4.3(b) and 4.3(c). The electric field components of the fundamental quasi TE mode concentrate at the waveguide sidewalls and become very sensitive to its roughness. The strong electric field discontinuities at these interfaces result from the high confinement. A direct impact is the scattering at the sidewall roughness [103]. It is the major origin of the linear propagation loss in silicon waveguides. An indirect impact stems from the induced carriers at the interface charges which affect the real- and imaginary part of the dielectric function [104]. It leads to absorption due to the plasma-dispersion effect which will be discussed below. The following discussion concentrates on the funda-

mental quasi TE mode. Besides a more precise fabrication, the resulting scattering loss can be decreased by broader waveguides and smaller etch depths so that smaller field intensities are exposed to the sidewall roughness and interface charges. In the end, a compromise has to be found regarding the single-mode condition and the magnitude of the bend radii. For example, typical propagation losses are 2.4 dB/cm for strip waveguides with the dimensions $W = 400$ nm and $H = 220$ nm or 0.7 dB/cm for rib waveguides with the dimensions from fig. 4.3 for the considered silicon photonics platform [96].

Bend loss is usually negligible above a certain bend radius for a given waveguide geometry and a given guided mode. The bend loss increases strongly below a critical radius which shrinks for smaller waveguides with higher confinements [105]. For example, the bend radius can be only $5\,\mu$m without causing any loss for a quasi TE mode of a strip waveguide with the dimensions $W = 400$ nm and $H = 200$ nm [97]. For the test structures in chapter 7, a large bend radius of $100\,\mu$m was chosen to avoid any bend loss for the used rib waveguide from fig. 4.3.

An important characteristic of silicon is its high thermo-optic coefficient which is temperature and wavelength-dependent. For example, in [106] the temperature dependence of the refractive index of silicon for a wavelength of 1523 nm was measured and approximated by the second order polynomial

$$\frac{\mathrm{d}n_{Si}(T)}{\mathrm{d}T} = 9.48 \cdot 10^{-5} + 3.47 \cdot 10^{-7} \cdot T - 1.49 \cdot 10^{-10} \cdot T^2 \qquad [\mathrm{K}^{-1}] \tag{4.5}$$

with temperature T in K. In the following eq. (4.5) is also used for 1550 nm since very similar values were measured for this wavelength [107] and the principal behavior should not change for that small wavelength change. Eq. (4.5) results in $1.84 \cdot 10^{-4}\,\mathrm{K}^{-1}$ for room temperature and in $1.99 \cdot 10^{-4}\,\mathrm{K}^{-1}$ for $80\,^{\circ}$C. This value is more than ten times higher than in silicon dioxide. It is the origin of the group index temperature dependence in fig. 4.4(b) for the silicon rib waveguide from fig. 4.3. In the simulations, $n_{Si}(293\,\mathrm{K}) = 3.4777$ was used as the refractive index of silicon at room temperature for a wavelength of 1550 nm. Its temperature-dependent change was taken into account by

$$n_{Si}(T)|_{\lambda=1550\,\mathrm{nm}} = n_{Si}(293\,\mathrm{K}) + \int_{293\,\mathrm{K}}^{T} \frac{\mathrm{d}n_{Si}(T)}{\mathrm{d}T}\mathrm{d}T \tag{4.6}$$

while the much lower temperature dependence of silicon dioxide was neglected. The temperature sensitivity of silicon deteriorates the performance of various photonic components if it is not compensated. For example, interference-based devices like arrayed waveguide gratings, Mach-Zehnder interferometers, or rings are highly affected by temperature variations. Usually, the device temperature has to be controlled by means of a heater which can be power intensive. A varying refractive index affects propagation delays and the exploited

interference characteristics. Temperature induced delay variations also degrade the performance of optical CDNs [80, 108]. A passive compensation technique is based on cladding materials with a negative thermo-optic coefficient which counteracts the impact of silicon. Such materials are polymers [109] or amorphous titanium dioxide (a-TiO_2) [110]. Here, the waveguide geometry is chosen so that the electric field intensity spans over the silicon and the cladding material at the inverse ratio of their thermo-optic coefficients. It becomes necessary to shrink the waveguide size to push a larger part of the electric field intensity out of silicon. Such athermal waveguides are always accompanied by increased scattering loss due to the higher field interaction with the waveguide sidewall roughness. For example, a propagation loss of $8\,$dB/cm was measured with amorphous titanium dioxide in [110] and even $50\,$dB/cm with polymer in [109]. These losses are usually too high for real applications. Moreover, polymers are neither robust nor CMOS-compatible. Therefore, the passive compensation technique is not suitable to mitigate the temperature dependence of an optical CDN. The high propagation loss would induce non-tolerable power mismatches at the outputs of a time-interleaved CDN. The unavoidable temperature sensitive skew of the optical CDN will be characterized and discussed in section 7.1.

Free carriers in silicon affect the guided light by a refractive index change n_{FCI} and an additional absorption α_{FCA}. This is the so-called plasma dispersion effect or free carrier effect (FCE) and semi-empirical formulas were first provided in [85]. In [111], recent experimental results were included and led to the updated expressions

$$n_{FCI} = -\left(5.4 \cdot 10^{-22} \cdot N_e^{1.011} + 1.53 \cdot 10^{-18} \cdot N_h^{0.838}\right) \qquad \text{and} \tag{4.7}$$

$$\alpha_{FCA} = 8.88 \cdot 10^{-21} \cdot N_e^{1.167} + 5.84 \cdot 10^{-20} \cdot N_h^{1.109} \qquad [\text{cm}^{-1}] \tag{4.8}$$

for a wavelength of $1550\,$nm. Here, N_e and N_h are the free electron and hole concentrations in cm^{-3}. For example, assuming an equal electron and hole concentration of $N_e = N_h = 10^{16}\,\text{cm}^{-3}$ results in additional free carrier absorption (FCA) of $\alpha_{FCA} = 0.64\,$dB/cm. The absorption increases to $\alpha_{FCA} = 8.94\,$dB/cm for one order higher densities of $N_e = N_h = 10^{17}\,\text{cm}^{-3}$. The different coefficients and exponents in eqs. (4.7) and (4.8) show that electrons and holes do not equally affect the refractive index and the absorption change. In general, these coefficients are wavelength-dependent [111].

4.2.1 Non-Linear Pulse Propagation

Silicon shows no second-order non-linearity due to its centro-symmetric crystal structure if strain is neglected. But the inversion symmetry leads to a large third-order non-linearity. Its Kerr coefficient is more than 100 times larger than in silicon dioxide in the telecommunication band, while the Raman gain coefficient is more than 1000 times larger [90]. Moreover,

the high confinement and the small waveguide cores enhance the non-linear effects so that these can be exploited even in short waveguides on chip scale. A detailed review and modeling of non-linearities in silicon can be found in [90]. Since the focus of this thesis is on the distribution of optical pulse trains on chip to time-interleaved ADCs, the model from [90] is restricted here to a non-linear pulse propagation model as it was done in [87]. In this case, the dominant effects are the Kerr effect and the two-photon absorption (TPA) accompanied by FCE. The Kerr effect induces an intensity-dependent refractive index change, while TPA excites bound electrons from the valence to the conduction band whenever the sum of the energy of two photons exceeds the silicon band gap of $E_{gap} = 1.12\,\mathrm{eV}$. This process is assisted by phonons for momentum conservation due to the indirect nature of the silicon band gap. The Kerr effect and the TPA process can be seen as nearly instantaneous due to their very short response time of $< 10\,\mathrm{fs}$ [90]. Directly after excitation, the TPA-induced free carriers have some excess energy above the conduction band minimum corresponding to a higher carrier temperature. These hot carriers interact with the lattice and equilibrate with a characteristic time of $> 50\,\mathrm{fs}$ [90, 112]. It should be noted that the formulas (4.7) and (4.8) are valid for a thermal quasi-equilibrium when hot carrier effects are negligible. In [112], it was shown that hot carriers with an excess energy of $\sim 0.3\,\mathrm{eV}$ above the bandgap (or with an equivalent temperature of $\sim 2000\,\mathrm{K}$) induce a $\sim 25\,\%$ smaller refractive index change than at room temperature.

The induced free carriers change their distribution within the waveguide with time by diffusion to lower density areas through thermal motion, drift due to external electric fields and recombination at crystal deformations at the waveguide core and cladding interfaces. Recombination within the lightly doped bulk silicon can be neglected due to the long lifetimes of $> 1\,\mu\mathrm{s}$ [113]. These effects can be combined and described by an effective carrier lifetime τ_{eff} within the waveguide core. It is defined as the $1/e$-value of an exponential decay. It can be decreased by:

1. Sweeping out carriers by applied electric fields across the waveguide through pin-junctions [114, 115]

2. Increased surface recombination by a higher waveguide surface-to-volume ratio [113]

3. Increased recombination centers within the waveguide by means of ion implantation [116, 117, 118]

In general, it can only be determined experimentally. Depending on the waveguide size and a possible usage of the mentioned methods for effective carrier lifetime decrease, it ranges between tens of picoseconds [114, 117] and tens of nanoseconds [113]. It should be noted that the assumption of a simple exponential decay may be too simple. For example, in [118]

a differentiation between a fast and a slow exponential decay had to be introduced to explain a simple pump-probe experiment.

The evolution of the slowly varying mode field amplitude $A(z,\tau)$ during propagation in a silicon waveguide can be described by [87, 90]

$$\frac{\mathrm{d}A}{\mathrm{d}z} = -\frac{\alpha_l}{2}A + \beta_{FCE}(\overline{N}_e,\overline{N}_h)A + j\frac{\omega_c n_{Kerr}}{c_0 A_{eff}}|A|^2 A - \frac{\beta_{TPA}}{2A_{eff}}|A|^2 A \tag{4.9}$$

where $\tau = t - \beta_1 z$ is the relative time frame with pulse center at $\tau = 0$, z is the position in the waveguide, β_1 is the group velocity per length and A_{eff} is the effective mode area defined as [119]

$$A_{eff} = \frac{Z_0^2}{n_{Si}^2}\frac{\left|\iint_{A_{tot}} \mathrm{Re}\left\{E(x,y)\times H^*(x,y)\right\}\bullet e_z \mathrm{d}x\mathrm{d}y\right|^2}{\iint_{A_{int}}|E(x,y)|^4\,\mathrm{d}x\mathrm{d}y}. \tag{4.10}$$

Here, $Z_0 = 377\,\Omega$ is the free-space wave impedance, e_z is the unit vector in propagation direction, A_{tot} is the cross section of the whole waveguide structure, while A_{int} is the non-linear interacting waveguide region. $\times$ and $\bullet$ represent the vector and scalar product and $E(x,y)$ and $H(x,y)$ are the modal electric and magnetic fields, respectively. For example, it leads to $A_{eff} = 0.17\,\mu\mathrm{m}^2$ for the rib waveguide in fig. 4.3. The mode field amplitude $A(z,\tau)$ in eq. (4.9) is normalized such that $|A|^2$ has unit of power. Since the considered gratings from section 4.1 couple light solely into one mode and waveguides are usually designed regarding the single-mode condition, it is convenient to assume that $A(z,\tau)$ refers to the fundamental quasi TE mode. In eq. (4.9), each term indicates a non-linear effect affecting the field amplitude. The first term takes linear losses due to waveguide sidewall roughness into account by the linear propagation loss α_l. The last term includes TPA. The TPA coefficient was measured in [120] and is $\beta_{TPA} = 0.5\,\mathrm{cm/GW}$ for a wavelength of $1550\,\mathrm{nm}$. The Kerr effect affects the field amplitude by the third term. Here, the Kerr coefficient is $n_{Kerr} = 2.5\cdot 10^{-5}\,\mathrm{cm}^2/\mathrm{GW}$ for $1550\,\mathrm{nm}$ [120]. Finally, the second term takes the FCE into account by [90]

$$\beta_{FCE}(\overline{N}_e,\overline{N}_h) = \frac{n_{Si}}{n_{grp}}\left(j\frac{\omega_c}{c_0}n_{FCI}(\overline{N}_e,\overline{N}_h) - \frac{1}{2}\alpha_{FCA}(\overline{N}_e,\overline{N}_h)\right) \tag{4.11}$$

where $n_{FCI}(\overline{N}_e,\overline{N}_h)$ and $\alpha_{FCA}(\overline{N}_e,\overline{N}_h)$ are given in eqs. (4.7) and (4.8) for a carrier angular frequency $\omega_c = 2\pi c_0/\lambda_c$ or a carrier wavelength of $\lambda_c = 1550\,\mathrm{nm}$, respectively. Here, $\overline{N}_e$ and $\overline{N}_h$ are the carrier densities averaged over the optical mode profile. Eq. (4.11) shows that, FCE are enhanced in a waveguide compared to bulk material as the modal refractive index is smaller because of the mode confinement [90]. According to eq. (4.9), the power loss rate due to TPA is given by [90]

$$\frac{\mathrm{d}P}{\mathrm{d}z} = -\frac{\beta_{TPA}|A|^4}{A_{eff}}. \tag{4.12}$$

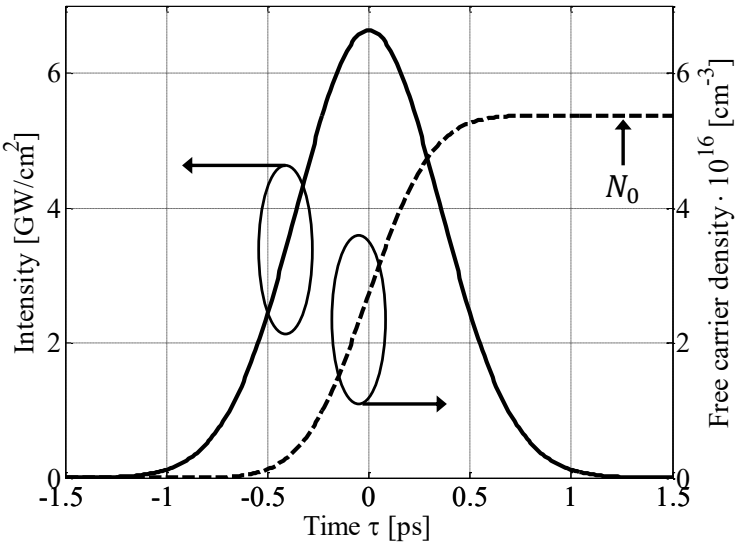

Figure 4.5: Free carrier density induced by TPA during a single Gaussian pulse with the pulse energy $E_p = 10\,\text{pJ}$ and the pulse width $\tau_o = 0.5\,\text{ps}$ for a silicon waveguide with $A_{eff} = 0.17\,\text{um}^2$ and $\tau_{eff} \gg \tau_o$. The free carriers accumulate to the concentration N_0 at the pulse tail.

Due to the fourth order amplitude dependence, it varies strongly across the pulse. The carrier generation rate in the silicon waveguide follows to [90]

$$R_{gen} = -\frac{1}{2h\nu_c A_{eff}} \frac{\mathrm{d}P}{\mathrm{d}z} = \frac{\beta_{TPA}|A|^4}{2h\nu_c A_{eff}^2}. \tag{4.13}$$

The averaged carrier density accumulates during a single pulse which can be expressed by [90]

$$\overline{N}(z,\tau) = \frac{\beta_{TPA}}{2h\nu_c A_{eff}^2} \int_{-\infty}^{\tau} e^{-\frac{\tau-\tau'}{\tau_{eff}}} |A(z,\tau')|^4 \mathrm{d}\tau'. \tag{4.14}$$

Eq. (4.14) results from eq. (4.13) taking into account instantaneous carrier generation and subsequent recombination with an effective carrier lifetime τ_{eff}. Fig. 4.5 shows the induced free carrier density from eq. (4.14) in a position z of a silicon waveguide for the Gaussian pulse power envelope

$$|A(\tau)|^2 = \frac{E_p}{\sqrt{\pi}\tau_o} \cdot e^{-\frac{\tau^2}{\tau_o^2}}. \tag{4.15}$$

with a pulse energy of $E_p = 10\,\text{pJ}$ and a pulse width of $\tau_0 = 0.5\,\text{ps}$. Assuming an effective mode area of $A_{eff} = 0.17\,\mu\text{m}^2$, eq. (4.14) leads to a carrier density of $N_0 \approx 5.375 \cdot 10^{16}\,\text{cm}^{-3}$ at the pulse tail causing a propagation loss of $\alpha_{FCA} = 4.4\,\text{dB/cm}$ according to eq. (4.8).

Since pulse train repetition periods are usually shorter than the effective carrier lifetime of passive waveguides, the carriers accumulate over multiple pulses. Free carrier accumulation

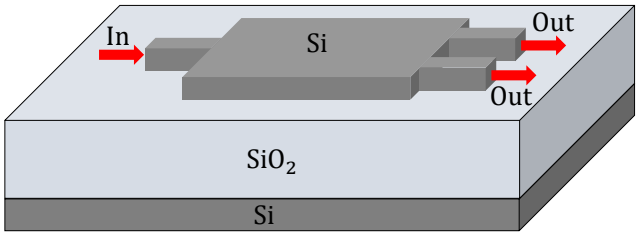

Figure 4.6: Schematic of a 1x2 MMI coupler consisting of a multimode waveguide and single-mode access waveguides at the input and output ports. The structure is based on silicon as the waveguide core with silica as the under-cladding and air as the over-cladding material .

from previous pulses can be expressed by [87]

$$N_{pre} = \underbrace{\sqrt{\frac{\pi}{2}}\frac{\beta_{TPA}}{h\omega_c A_{eff}^2}\frac{E_p^2}{\tau_o}}_{N_0} \cdot \underbrace{\frac{1}{e^{\frac{1}{f_{rep}\tau_{eff}}} - 1}}_{\text{Accumulation}} \tag{4.16}$$

for the Gaussian power profile from eq. (4.15). The first part of eq. (4.16) represents the effective carrier density N_0 induced by a single Gaussian pulse as calculated by eq. (4.14) and shown in fig. 4.5. The following accumulation factor takes free carriers induced by all previous pulses into account. For example, a pulse train with pulse properties from fig. 4.5, a repetition rate of $f_{rep} = 10\,\text{GHz}$ and an effective carrier lifetime of $\tau_{eff} = 1\,\text{ns}$ leads to an averaged carrier density of $N_{pre} \approx 10N_0$ corresponding to a propagation loss of $\alpha_{FCA} = 57.8\,\text{dB/cm}$ according to eq. (4.8)! In this case, accumulation has a significantly higher impact on the carrier density than carrier generation by a single pulse.
It should be noted that the described model was derived for small non-linear perturbation. The maximal intensity should be $< 150\,\text{GW/cm}^2$ according to the measurements in [121]. The non-linear pulse propagation model will be used in section 4.6 to estimate the impact of non-linearities on the optical CDN. Experiments will be shown in section 7.2.

4.3 Multimode Interference Coupler

Optical power dividers are necessary in optical CDNs for time-interleaving which is illustrated in fig. 1.3. A multimode interference (MMI) coupler is the favorable photonic device for this purpose thanks to its excellent performance. It consists of a multimode waveguide with typically > 3 guided modes and access waveguides at the input and output ports. An optical field at the input port excites several modes of the waveguide which propagate with different propagation constants inducing interference patterns across the multimode waveguide. At periodic positions along the propagation direction, these patterns correspond to reproduced single or multiple images of the input field which is called the self-imaging

principle. A review of the theory is provided in [122]. By exploitation of these interference effects, general NxM couplers can be made with an excess loss of < 0.5 dB, a crosstalk as low as -30 dB and an imbalance of < 0.5 dB [122, 123]. An important advantage of MMI couplers is their relaxed fabrication requirements. Especially 1x2 MMI couplers show almost ideal characteristics [97, 124]. A schematic of the principle structure is shown in fig. 4.6. Simulations of the 2x2 MMI coupler in [125] show a barely measurable excess loss and an imbalance of < 0.1 dB for the C-band and an MMI coupler width of $15\,\mu$m.
The MMI coupler bandwidth is inversely proportional to the number of coupler ports [123]. Excess loss decreases for more guided modes or broader waveguides, respectively [125]. In general, the MMI coupler performance is better for a lower number of ports and more guided modes. Usually, a compromise has to be found between the device size and its performance.

4.4 Modulator

A modulator can be used in photonic ADCs for the sampling process. Here, an optical pulse train is modulated by the sampled RF signal. This principle will be discussed in detail in section 5.2. In this section, the performance of silicon modulators is discussed in regards of their usability for integrated photonic ADCs.
The physical effect in silicon, which is exploited for modulation, is based on FCE. The free carriers change the refractive index according to eq. (4.7) in dependence of their density. This is used for modulation in interferometric devices either by injection, depletion or accumulation of the carriers. Such devices are Mach-Zehnder interferometer (MZI) or ring modulators.
Ring modulators can be very small and consume only low power. Unfortunately, rings have only a limited optical bandwidth and are very sensitive towards fabrication and temperature variations. Thermal stabilization and tuning effort can largely increase the power consumption. Furthermore, due to the limited optical bandwidth, rings are not suitable for modulation of wavelength-interleaved pulse trains like suggested in [25] or ultra-short pulses in general.
MZI modulators need much more space than rings, but it is justified by their superior characteristics. The advantages of MZI modulators are their thermal insensitivity, high robustness against fabrication variations and large optical bandwidth [126]. The large bandwidth enables modulation of wavelength-interleaved pulse trains and makes MZI modulators attractive for photonic ADCs. Therefore, their performance is discussed in the following.
Carrier-injection-based modulators [127] use forward biased pin-diodes across the modulator arms. The resulting refractive index change causes a phase shift between the output

arms and affects the intensity of the combined output signal. Unfortunately, this effect is always accompanied by FCA according to eq. (4.8). The disadvantage of carrier injection is the long minority carrier lifetime decreasing the modulation speed. This method cannot provide sufficiently high electric bandwidth for photonic ADCs.
Carrier-depletion-based modulators use reverse biased pn-junctions across the waveguides. They are less efficient than their injection-based counterparts due to the p- and n-doping within the waveguides and the resulting higher loss. But the huge advantage is the short carrier lifetime in the depletion region which enables a high-speed operation. The bandwidth limit is set by the resistive regions between the pn-junction and the metallic contacts and the capacitance of the pn-junction itself. Usually, such depletion-based modulators with high speeds of $> 25\,\text{GHz}$ necessitate high switching voltages of $V_\pi > 5\,\text{V}$ [126, 128, 129]. This is incompatible with conventional drivers. Unfortunately, driver compatible voltages of $< 4\,\text{V}$ limit the modulation speed to $< 20\,\text{GHz}$. Lower voltages decrease the modulation efficiency. As a result, longer modulator arms are necessary for the π phase shift which increases the capacitance and limits the bandwidth. A high bandwidth of $30\,\text{GHz}$ was achieved for the phase shifter in [129]. Here, the optical loss was only $2.7\,\text{dB}$, while the switching voltage was $V_\pi = 7.5\,\text{V}$. In [128] a bandwidth of $41\,\text{GHz}$ was achieved with an insertion loss of $3.8\,\text{dB}$ but with high $V_\pi = 8\,\text{V}$. Similar results were shown in [126] with a bandwidth of $35\,\text{GHz}$, an insertion loss of $4.5\,\text{dB}$ and a high switching voltage of $V_\pi = 7.5\,\text{V}$.
In carrier-accumulation-based modulators [130], metal-oxide-semiconductor capacitors are used where p- and n-doped areas are separated by a thin oxide layer. Applied forward bias accumulates free carriers on both sides of the oxide. The free carriers overlap with the guided mode inducing the desired phase shift in the interferometric structure. Accumulation-based modulators enable high-speed operation and the bandwidth limit is again set by the resistive contacts and the capacitance of the oxide layer. Their performance is similar to carrier-depletion-based modulators.

4.5 Photodiodes

Photodiodes represent the interface between optics and electronics at the end of an optical path. Their performance is essential for the transfer of superior characteristics of the optics to the electronics such as the ultra-low jitter performance of optical pulse trains.
The focus of this thesis lies on integrated photonic ADCs with silicon waveguides in the CDN. Silicon is transparent for wavelengths $> 1100\,\text{nm}$ and is, therefore, optimal for guiding the typical telecommunication wavelengths of $1300\,\text{nm}$ and $1550\,\text{nm}$. Hence, a material which absorbs theses wavelengths and can be fabricated at the end of the silicon waveg-

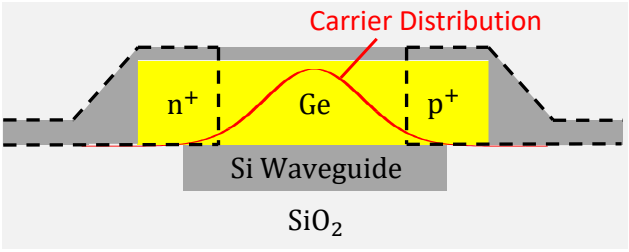

Figure 4.7: Cross section of a lateral germanium photodiode. Light is coupled out of the silicon waveguide into the intrinsic germanium layer where it gets absorbed. The induced carrier distribution is indicated by a normal probability distribution. The p^+ and n^+ doped regions on the left and right side of the germanium serve for contacting and form a pin diode with the intrinsic region.

uides in a CMOS-compatible process is necessary for the photodetection. Germanium is such a material which can be grown selectively on top of the silicon waveguide. Thanks to the higher refractive index of germanium (≈ 4 for $1550\,\text{nm}$) compared to silicon (≈ 3.5 for $1550\,\text{nm}$), the light is pushed out of the waveguide into the germanium cladding where it gets absorbed. While the light is absorbed in direction of the waveguide, the generated carriers can be extracted out of the intrinsic region by an applied electric field across the waveguide. The cross section of such a photodiode is shown in fig. 4.7. The electric field is built up by doping the germanium on both sides and applying a reverse bias at these contacts. Such a lateral geometry shows no trade-off between responsivity and bandwidth like in vertical photodiodes.

A waveguide-integrated germanium pin photodiode was shown in [91] with a $3\,\text{dB}$ bandwidth of $> 70\,\text{GHz}$, a responsivity of $> 1\,\text{A/W}$ for a wavelength of $1550\,\text{nm}$ and a dark current of $\approx 100\,\text{nA}$. All these values were measured at the reverse bias of $1\,\text{V}$. Furthermore, these photodiodes are linear for constant photocurrents up to $10\,\text{mA}$ at a reverse bias of $2\,\text{V}$. Such photodiodes are essential components of the silicon photonics BiCMOS platform from [95]. The excellent bandwidth, responsivity and linearity characteristics make these photodiodes interesting for low jitter photonic ADCs which will be discussed in detail in chapter 6. Good performance was also shown in [131] for heterogeneously integrated indium phosphide-based waveguide coupled photodiodes. In this case, a responsivity of $0.95\,\text{A/W}$ and a bandwidth of $48\,\text{GHz}$ were achieved. Furthermore, these photodiodes showed no saturation effects for continuous wave photocurrents up to $60\,\text{mA}$.

The absorption of an ultra-short optical pulse abruptly induces a high number of carriers within the intrinsic region of the photodiode. For a sufficiently high amount of induced carriers, the built-up electric field across the absorption area can decrease substantially. The resulting slower carrier transport changes the photodiode impulse response. This is known as the *screening effect*. In the following, this effect is investigated for a previous generation

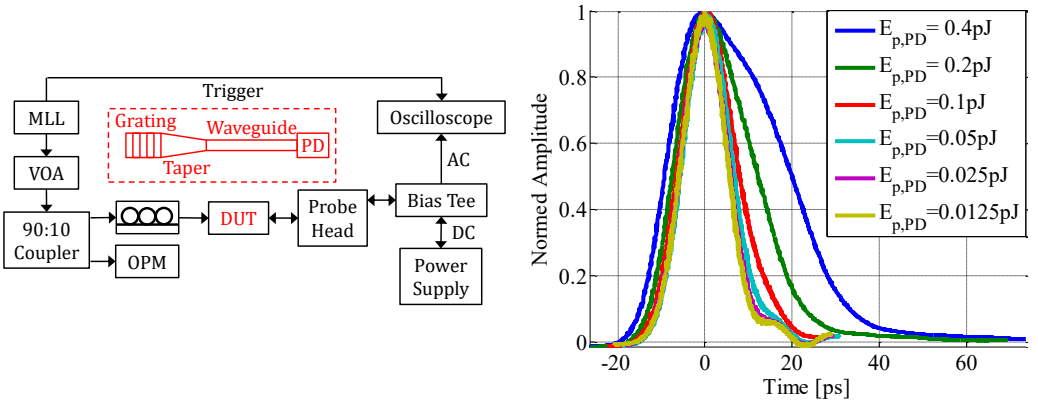

(a) (b)

Figure 4.8: Photodiode impulse response in dependence on the absorbed pulse energy $E_{p,PD}$ for an applied reverse bias of 1 V at room temperature. (a) Block diagram of the measurement set-up with the schematic of the DUT in red. Details are given in the text. (b) Measured output at the oscilloscope. The photodiode impulse response is normed to the maximum amplitude.

of the integrated germanium photodiode prior to [91]. The measurement set-up is shown in fig. 4.8(a). A 100 MHz MLL was emitting ultra-short optical pulses with a full-width-half-maximum pulse width of $\tau_{o,FWHM} = 84$ fs, according to the data sheet. These were attenuated by a subsequent variable optical attenuator (VOA) and split by a 90:10 coupler. The -10 dB output port was used to monitor the average input power by means of an optical power meter (OPM). The 0 dB output port was coupled into the device under test (DUT) which consisted of a 1D grating coupler, a taper, a short waveguide and the germanium photodiode. The optimum polarization for the grating was adjusted by means of a 3-paddle polarization controller in front of the DUT so that the measured photocurrent was maximized. A probe head with a bandwidth of 67 GHz was placed at the contact pads. The output was connected to a bias tee which had a bandwidth of 65 GHz. The AC current was measured by a 70 GHz oscilloscope. The DC output port was connected to a power supply which applied a reverse bias of 1 V to the photodiode and measured the dc current. The oscilloscope was triggered by the MLL. The measurements were performed at room temperature and the recorded and normed impulse responses are shown in fig. 4.8(b). The photodiode responsivity was known from previous measurements to be > 1 A/W. It corresponds to a photodiode quantum efficiency of $\eta_{PD} \approx 0.9$. An average optical input power between -24 dBm and -9 dBm with 3 dBm steps was used. An overall loss of 4.5 dB was assumed stemming from the fiber facet, the grating coupler, and the deviation from the optimum angle of incidence by 2 degrees. The deviation was discovered after the measurements and decreased the coupling efficiency by roughly 1 dB. The resulting pulse energies are in-

serted in the legend of fig. 4.8(b). It can be seen that for the applied reverse bias at the used photodiode, saturation effects appeared for absorbed pulse energies of > 0.05 pJ. It affected the falling edge of the impulse response. Pulse-to-pulse energy fluctuations would cause a variation in the falling edge of the impulse response. This corresponds to a pulse-energy-dependent center of mass shift. In this case, amplitude noise is coupled to phase noise and increases the jitter [76, 77].

The photodiode linearity is essential for the transfer of ultra-low jitter characteristics of optical pulse trains to the electronics which will be discussed in detail in chapter 6. However, even linear photodiodes add some amount of jitter to the induced electric pulse trains. The photodiode impulse response results from the superposition of millions of individual carrier drifts and the embedded circuit. The drift time depends on the position of the generated carriers within the intrinsic region. Their location can be described by a probability function which refers to the mode intensity profile. Furthermore, the drift process is accompanied by several scattering mechanisms within the crystal [132]. This adds another uncertainty of the drift time and leads to an intrinsic photodiode jitter. In [69], this jitter was measured to 0.8 fs and quantified by Monte-Carlo simulations in [133]. It should be noted that this value is only valid for a certain operating point. In general, this jitter depends on the photodiode material, the width of the intrinsic region, the applied voltage, the temperature, the crystal defects and probably several other conditions.

As an example, an estimation is provided for the jitter in germanium photodiodes due to a random distribution of generated carriers within the intrinsic region. Scattering effects should be neglected. It is assumed that the carriers drift with a constant saturation drift velocity towards the p- or n-regions. The saturation drift velocity of holes and electrons in germanium has the same value of $v_{c,sat} \approx 7 \cdot 10^4$ m/s for room temperature and for high electric fields [132, 134, 135]. The positions of generated carriers are assumed as normally distributed with a mean value corresponding to the center of the intrinsic region. This is indicated in fig. 4.7. The normal distribution is an approximation of the fundamental guided mode in silicon waveguides which is illustrated in fig. 4.3. The standard deviation of a single generated carrier position should be $\sigma_{p,1} = 100$ nm since for the germanium photodiode in [91] it was estimated that the depleted region is at most 200 nm for a reverse bias of 2 V. Furthermore, an absorbed pulse energy of 0.2 pJ is assumed with a pulse center wavelength of 1550 nm. The amount of induced electrons and holes results in $N_{el} = N_{hol} = 1.56 \cdot 10^6$. Then, the standard deviation of the center of mass position for N_{el} electrons corresponds to

$$\sigma_{p,N} = \sigma_{p,1}/\sqrt{N_{el}} \tag{4.17}$$

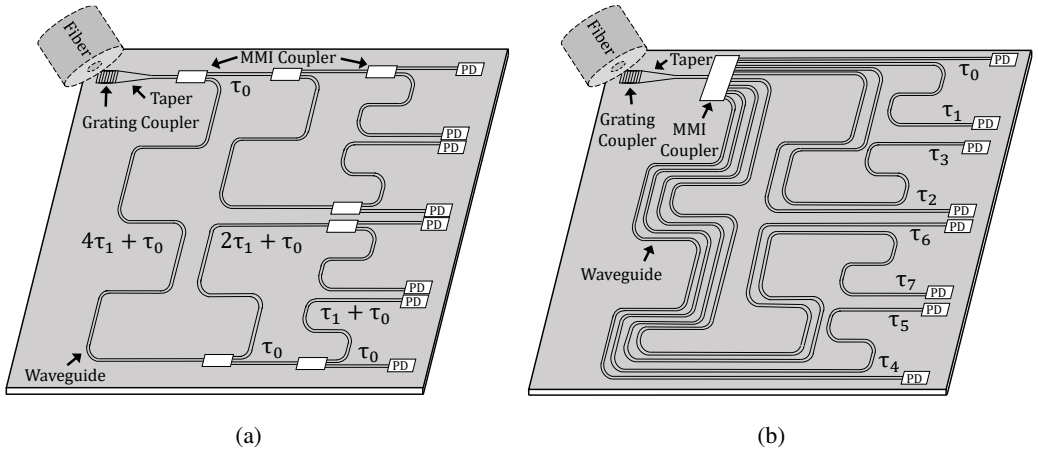

(a) (b)

Figure 4.9: Optical CDNs for 8 time-interleaved samplers consisting of (a) several 1x2 MMI couplers or (b) a single 1x8 MMI coupler for signal splitting

since the variance $\sigma^2_{p,N}$ of the average of independent events with the same variance $\sigma^2_{p,1}$ shrinks linearly with the number N_{el}. Now, the jitter can be identified as the drift time uncertainty due to the shifted center of mass position. This time uncertainty results in $\sigma_{p,N}/v_{c,sat} = 1.14\,\text{fs}$. Holes have a similar impact and taking their number into account should decrease this jitter by $1/\sqrt{2}$. It should be noted that the assumed normal distribution enables carrier generation outside of the intrinsic region since the probability density function is not limited. Furthermore, the diffusion process at the doped region has not been included. Nevertheless, the simple example provides a perception for the order of magnitude of the photodiode intrinsic jitter.

4.6 Optical Clock Distribution Network

Integrated optical clock distribution networks (CDNs) became increasingly interesting for research when electronic ICs met serious challenges in terms of clock distribution [6, 9] while low jitter MLLs emerged [136]. The superiority of optical towards electrical clock distribution regarding the clock precision [8, 9] is essential for the performance of integrated photonic ADCs. The first optical CDNs on chip were designed for VLSI circuits and had a symmetrical H-tree architecture [9, 11] similar to fig. 1.1(b). This design can be adapted for time-interleaved photonic ADCs where the delays are set by different waveguide lengths as suggested in [87, 88]. This is schematically shown for the optical CDNs in fig. 4.9 where an input signal is split and distributed across the die with certain delays to 8 outputs. In the schematic of fig. 4.9(a), the splitting is performed by several 1x2 MMI couplers instead of a single 1x8 MMI coupler like in fig. 4.9(b). It can be beneficial because couplers with

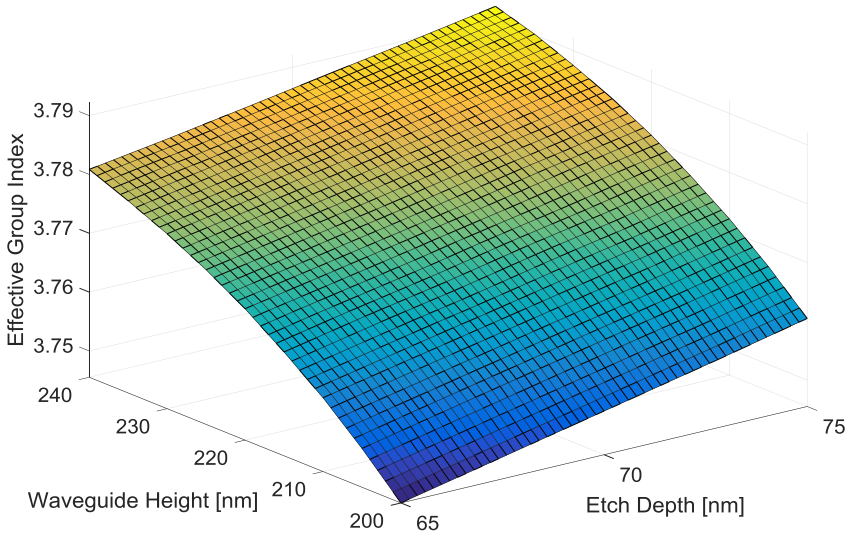

Figure 4.10: Effective group index for the rib waveguide from fig. 4.3 with the etch depth and height uncertainty of (70 ± 5) nm and (220 ± 20) nm resulting from fabrication tolerances. The waveguide width is 700 nm. The simulation has been performed with *JCMwave* for a center wavelength of 1550 nm and room temperature.

smaller splitting ratios have a better performance which was mentioned in section 4.3.
In the following, the optical CDN performance will be discussed for a certain example which was published partly in [87]. It is assumed that a 10 GHz MLL is used to clock 8 time-interleaved samplers resulting in a net sampling rate of 80 GS/s. In the concrete example, the delays relative to the shortest path are $\tau_k = k \cdot 12.5\,\text{ps}$ with $k = 1, 2, ...7$. Silicon rib waveguides from fig. 4.3 are considered for signal distribution. Performance degradation of optical CDNs corresponds to channel mismatch effects such as power imbalance and skew. At first, the skew is addressed. The temperature-dependent group index of the silicon rib waveguide from fig. 4.3 was derived by simulations and is shown in fig. 4.4(b). It leads to a temperature-induced change of the delays $d\tau_k$ as:

$$d\tau_k = \tau_k \cdot \frac{\mathrm{d}n_{grp}/\mathrm{d}T}{n_{grp}}. \tag{4.18}$$

A typical chip temperature of 80 °C results in a group refractive index of $n_{grp} = 3.7879$ for the center wavelength 1550 nm for the silicon rib waveguide from fig. 4.3, according to simulations. Its temperature drift results in $\mathrm{d}n_{grp}/\mathrm{d}T = 2.34 \cdot 10^{-4}\,\mathrm{K}^{-1}$ which was simulated with the finite-element-method-based software JCMwave. In eq. (4.18) this leads to $d\tau_k = k \cdot 0.774\,\text{fs/K}$ for the temperature sensitivity of the skew with a maximum of $d\tau_7 = 5.42\,\text{fs/K}$ between the first and the last channel. The temperature-dependent skew was simulated for the specified waveguide geometry. Fabrication tolerances, however, cause a waveguide geometry variation and, therefore, a deviation from the specified group index. This induces a skew as well. In general, these variations are randomly distributed across

Parameter	Value
Carrier wavelength	$\lambda_c = 1550\,\text{nm}$
Effective mode area	$A_{eff} = 0.17\,\mu\text{m}^2$
Group index	$n_{grp} = 3.7879$
Linear scattering loss	$\alpha_l = 0.7\,\text{dB/cm}$
Repetition rate	$f_{rep} = 10\,\text{GHz}$
Group velocity dispersion	$\beta_2 = 1.85\,\text{ps}^2/\text{m}$
Kerr coefficient	$n_2 = 2.5 \cdot 10^{-5}\,\text{cm}^2/\text{GW}$
TPA coefficient	$\beta_{TPA} = 0.5\,\text{cm/GW}$

Table 4.1: Simulation parameters for the non-linear pulse propagation model

the die and its impact is more critical for smaller structures. For example, the group index of the rib waveguide in fig. 4.3 is much more affected by height and etch depth than by width variations. In the following, their impact on the skew is analyzed. The silicon layer of the SOI wafer varies in the range of (220 ± 20) nm, while the etch depth varies between (70 ± 5) nm. The resulting group index range is shown in fig. 4.10 for a center wavelength of 1550 nm for room temperature. In the worst case scenario of a constant etch depth of 65 nm and a constant waveguide height of 200 nm across the die, the maximum skew results in 700 fs between the first and the last CDN output. Such a high skew has to be compensated. It should be noted that the optical CDN for synchronous clocking of ICs in fig. 1.1(b) has no designed delays between its outputs. Therefore, the skew would be negligible for such CDNs.

Another unavoidable disadvantage of time-interleaved optical CDNs is the power imbalance at the outputs. The maximum specified delay in the example mentioned above is $\tau_7 =$

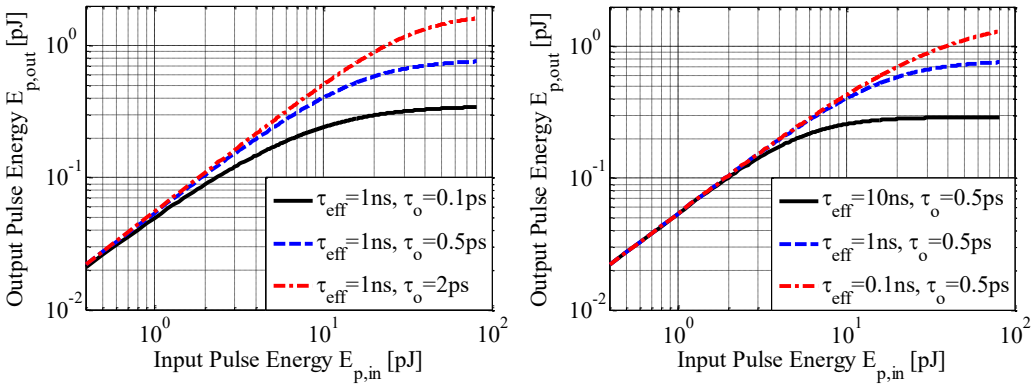

(a) (b)

Figure 4.11: Output pulse energy $E_{p,out}$ in dependence on the input pulse energy $E_{p,in}$ for the longest path of the CDN from fig. 4.9(a) for (a) a constant effective carrier lifetime τ_{eff} and a varying pulse width τ_o and for (b) a constant pulse width τ_o and a varying effective carrier lifetime τ_{eff}

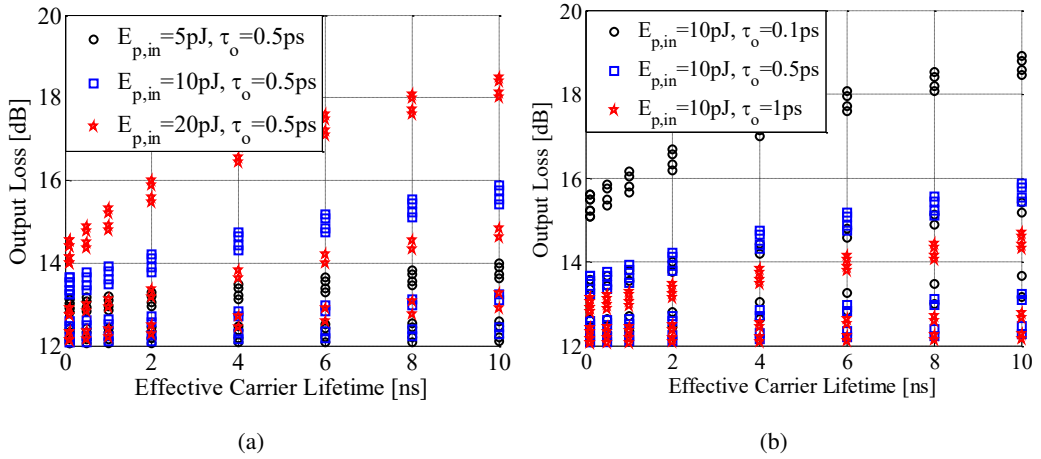

Figure 4.12: Overall losses for the CDN from fig. 4.9(a) between the input grating and the 8 output branches for (a) a constant Gaussian pulse width τ_o and a varying input pulse energy $E_{p,in}$ and (b) for a constant pulse energy and a varying pulse width in dependence on the effective carrier lifetime.

87.5 ps. Using the introduced group index of $n_{grp} = 3.7879$ for the rib waveguide leads to a maximum length difference of $L_7 = \tau_7 \cdot c_0/n_{grp} = 6.93$ mm. A linear scattering loss of 0.7 dB/cm for rib waveguides [96] results in a power imbalance of 0.49 dB. Strip waveguides have usually more than 3 times higher losses [96] and would increase the power imbalance by a similar factor. Since ultra-short pulses are distributed to individual ADCs by silicon waveguides, non-linear losses may reach non-negligible values. In the following, the introduced model for non-linear pulse propagation from section 4.2.1 is used for the analysis of the channel imbalance. Simulation parameters are summarized in tab. 4.1. The non-linear pulse propagation in silicon waveguides was introduced in eq. (4.9). In general, this equation is solved numerically by the *split-step Fourier method*. In the following simulation, it was implemented as a local error method according to [137] where each propagation length per step is changed dynamically depending on the error of the previous step. The maximum tolerable error per step was set to 1 %. The optical CDN from fig. 4.9(a) was chosen for the simulations with the delays $d\tau_I = 12.5$ ps and $d\tau_0 = d\tau_I/10$ or $dL_I = 0.99$ mm and $dL_0 = 99$ um, respectively. Furthermore, the short waveguide between the taper and the first MMI coupler is considered very short, so that its impact can be neglected. It is assumed that optical pulses with the pulse energy $E_{p,in}$ enter the chip with a repetition rate of 10 GHz. Assuming a 1D grating coupler from [95] results in a typical coupling loss of 3 dB. According to the discussion in section 4.3, the power splitters can be considered ideal. The resulting pulse energy of $E_{p,in}/4$ leaving the first 1x2 MMI coupler is used as the input, while the simulation is performed for the longest path of the CDN in fig. 4.9(a). TPA, FCE, Kerr non-linearity, dispersion and linear loss were included in the simulation

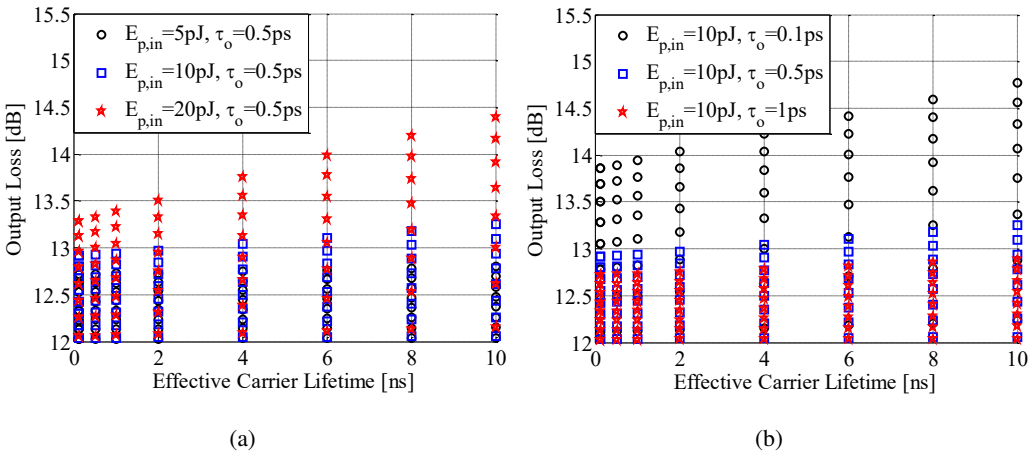

Figure 4.13: Overall losses for the CDN from fig. 4.9(b) between the input grating and the 8 output branches for (a) a constant Gaussian pulse width τ_o and a varying input pulse energy $E_{p,in}$ and for (b) a constant pulse energy and a varying Gaussian pulse width in dependence on the effective carrier lifetime.

and a Gaussian pulse shape from eq. (4.15) was assumed. The effective carrier lifetime is considered to be equal for electrons and holes since these recombine in pairs. The results are shown in fig. 4.11 for varying pulse energies, pulse widths and effective carrier lifetimes. In fig. 4.11(a), an effective carrier lifetime of 1 ns is assumed which is typical for passive silicon waveguides. It is shown that the output pulse energy saturates. The saturation value depends on the pulse width and the input pulse energy. In fig. 4.11(b), the pulse width is kept constant, while the effective carrier lifetime is varying. Here, the very short lifetime of $\tau_{eff} = 0.1$ ns corresponds to waveguides with a pin-junction where an applied electric field extracts the free carriers out of the waveguide [115]. The long lifetime of $\tau_{eff} = 10$ ns corresponds to passive waveguides with large widths and thicknesses of $> 1\,\mu$m [113]. It is obvious that non-linear loss has to be avoided to minimize channel power imbalance. According to fig. 4.11, a pulse energy of 10 pJ can be seen as a threshold value.

The channel power imbalance was simulated in dependence on the effective carrier lifetime, the pulse energy and the pulse width for the CDN from fig. 4.9(a). The results are presented in fig. 4.12. In fig. 4.12(a), the overall losses from the CDN input to the 8 output branches are plotted in dependence on the effective carrier lifetime. The pulse width is kept constant, while for the pulse energy values were assumed with low, medium and high non-linear loss. As can be seen, the power imbalance increases to > 1 dB even for low non-linear loss. A similar behavior can be observed if the pulse energy is kept constant, while the pulse width is varying in fig. 4.12(b). In summary, the channel power imbalance cannot be avoided already due to the linear loss and different waveguide lengths.

Another way to avoid non-linearities is splitting the pulse energy directly after the grating

coupler by a 1x8 MMI coupler which is schematically shown in fig. 4.9(b). In this case, the losses are considerably smaller as can be seen in fig. 4.13. However, it should be taken into account that 1x8 MMI couplers have non-negligible insertion losses and the power splitting already induces a power imbalance between the MMI outputs. Moreover, the bandwidths limitations attenuate and broaden the ultra-short pulses. Because of that, an optimal solution for the CDN architecture regarding the pulse characteristics is application-dependent.

Chapter 5

Photonic Analog-to-Digital Converters

The ADC performance improvement by means of photonics was suggested by Taylor already in 1979 [138]. But there had been no justification for the research effort due to the advance of electronics until Walden revealed a slowdown of electronic ADC performance evolution in his survey in 1999 [23]. Since then, more effort has been made to use photonics to increase the sampling rate and/or the resolution of sampled electronic signals. An excellent review of these studies was given in [24]. The main motivation for using photonics is the ultra-low timing jitter of pulse trains provided by optical sources. Their superior jitter characteristics towards electronic oscillators were explained in [29] by means of the fluctuation-dissipation theorem. It was shown that the mode-locked lasers (MLLs) can easily achieve two orders of magnitude less jitter. Ultra-low phase noise microwave oscillators such as sapphire-loaded cavity resonators (eventually even cryogenically cooled) are excluded here for the desired application since they are bulky and impractical.

MLLs are able to provide ultra-low jitter optical pulse trains which are considered as a clock source in this thesis. Their impressive suitability for synchronization was already shown in long-distance applications [30] where a clock signal was distributed over a $1.2\,\mathrm{km}$ dispersion compensated polarization maintaining fiber link. Low frequency jitter components from thermal drift, acoustic noise and mechanical stress within the fiber were suppressed by means of a feedback loop and a timing jitter impact of $< 1\,\mathrm{fs}$ was achieved over 16 days of uninterrupted operation.

In the following section, MLL varieties and their characteristics are discussed to assess their potential to serve as a clock source for photonic ADCs. It should be noted that there are other sources providing stable optical pulse trains. An alternative to MLLs is an optoelectronic frequency comb generator. Here, a low timing jitter RF signal is used to carve

pulses from a continuous wave (CW) laser output by means of an intensity modulator. This scheme of a pulse carver can be extended by several cascaded electro-optic phase modulators. The resulting higher phase modulation index induces more harmonics around the CW laser frequency which are spaced by the used RF oscillator frequency. In this way, a 10 GHz repetition rate with a low jitter of 11.35 fs for the offset frequency fluctuation range 1 Hz-10 MHz was achieved in [139]. Moreover, the repetition rate and the center frequency were tunable. The big disadvantage of such approaches is the necessity of an ultra-stable RF source and a narrow linewidth CW laser making the clock generation much more complex. For example, the stable microwave signal in [139] was actually generated by optical frequency division.

After the introduction of the expected MLL performance in section 5.1, the previous efforts and achievements in building photonic ADCs are discussed by means of several publications in section 5.2. The goal of this chapter is to provide a general understanding of the expectable optical pulse train characteristics and the different ways to exploit them in photonic ADCs. Based on the provided information, the photonic ADC noise performance will be analyzed in chapter 6.

5.1 Mode-Locked Laser

A detailed analysis of the mode-locking process, the vast MLL varieties and their physical basics is far beyond the scope of this thesis. Since the focus lies on the photonic ADC performance analysis, it is sufficient to provide a basic understanding of the typical MLL types and their characteristics which are of interest for the addressed application. Hence, the goal of this section is to introduce the pulse train performances these lasers can provide for the photonic ADCs analyzed in chapter 6.

A mode-locked laser (MLL) is using the *mode-locking technique* to emit periodic ultra-short optical pulses. Here, the superposition of resonator longitudinal modes leads to pulse formation if their relative phases fulfill a certain condition. This interpretation in the frequency domain is the origin of the term mode-locking [102]. The more longitudinal modes are involved in the pulse formation process, the shorter pulses can be generated. The dynamics and the mode-locking mechanism can be described mathematically by the *Haus-master equation* introduced by Haus in [140].

The laser resonator contains primarily a gain medium and either an active or a passive nonlinear element causing the mode-locking [102]. The principle schematics are illustrated in fig. 5.1. Active MLLs perform the mode-locking either by loss or phase modulation by means of a modulator, while a saturable absorber is responsible for an intensity-dependent loss leading to pulse formation in passive MLLs. The saturable absorbers are based for in-

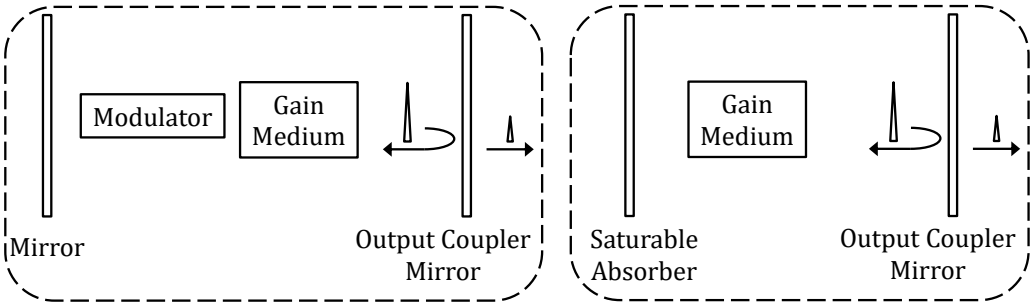

Figure 5.1: Schematic set-up of (a) an active MLL and (b) a passive MLL

stance on semiconductor saturable absorber mirrors (SESAM) [61, 65, 81, 141], carbon nanotubes (CNT) [83, 84] or graphene layers [102]. Moreover, artificial saturable absorbers can be realized for instance by non-linear polarization evolution (NPE) [63, 64], Kerr-lensing or coupled-cavities (also known as additive-pulse mode-locking) [140]. More details about the saturable absorbers can be found in [102].

Active MLLs have generally broader pulse widths in the picosecond range. Here, the curvature of the gain window is responsible for the pulse width magnitude and is restricted by the electronic reference signal speed [142]. Furthermore, the minimal timing jitter is given by the RF signal reference [142]. Passive MLLs achieve pulse widths in the femtosecond range since the pulse is modulating the gain window by its own intensity profile leading to a stronger shortening effect [102]. The final pulse width results from an equilibrium from shortening effects such as loss modulation and broadening effects such as limited gain bandwidth. In soliton MLLs, the pulse formation is dominated by self-phase modulation and dispersion [102]. Assuming a single pulse circulating in the resonator, the repetition rate results from the reverse round-trip time. By means of harmonic mode-locking, a multiple of the fundamental repetition rate can be achieved [78, 79]. A small percentage of the pulse energy is periodically leaving the resonator through the partly transparent output coupler mirror forming the pulse train. Most MLLs are continuously pumped and the circulating pulse extracts energy from the gain reservoir at each round-trip. This is enabled by the fact that the upper-state lifetime of the gain medium is much higher than the pulse spacing.

There is a vast variety of MLLs which are classified by their gain media [102]. In the following, their typical characteristics are discussed including some examples from publications which are summarized in tab. 5.1.

Solid-state (bulk) lasers are based on ion-doped crystals or glasses as gain medium. Often the pulses are circulating in free space within the resonator and transit optical components

[102]. Therefore, the mechanical stability of the components as well as the impact of dust in the optical path are important issues. Such lasers can provide ultra-short optical pulses in the typical range of 30 fs-30 ps [61, 62, 65, 81, 83, 102, 143]. A record value of 5 fs has been shown with a Ti:sapphire laser [102]. High average output power can be achieved in a typical range of 50 mW-1 W [61, 62, 65, 81, 102]. Lower output power can still be amplified by an external optical amplifier [83]. Typical repetition rates are in the regime of 50 MHz-500 MHz [61, 62, 65, 81, 102] but the gigahertz range has also been achieved [83, 143]. The wavelengths of bulk lasers are typically in the range of 700 nm-1000 nm [102]. For example, neodymium-doped as well as ytterbium-doped [83] gain media emits around 1000 nm. Titanium-doped sapphire crystals emit at 800 nm and chromium-doped colquiriites emit in the range of 800 nm-900 nm [65]. By means of erbium-doped glass, the C-band telecommunication wavelength at 1550 nm can be used [61, 62, 143].

Fiber lasers are based on rare-earth-doped fibers as gain media. For example, erbium-doped fibers emit wavelengths at 1550 nm [63, 78, 84] and ytterbium-doped fibers emit around 1000 nm [64]. Passively mode-locked fiber lasers generate ultra-short pulse widths in the typical range of 30 fs-500 fs [63, 64, 84, 102]. Detrimental effects within the fiber, such as uncompensated chromatic dispersion and excessive non-linearities, limit the exploitation of the full gain bandwidth. The non-linearities restrict lower pulse widths as well as higher intracavity pulse energies which (at least for low repetition rates) are usually orders of magnitudes lower than in solid-state lasers [102, 144]. Because of that, a higher degree of output coupling is necessary to reduce the intracavity pulse energy and to enhance the usable output power [144]. As a result, the average output power is typically $\ll 100$ mW [63, 84, 102]. But low output power can always be increased by an external optical amplifier [84]. Furthermore, the pulse width can be compressed externally although it does not reduce the timing jitter [144]. The lower pulse energies, higher output losses and correspondingly higher gain per round-trip make fiber lasers more sensitive to quantum noise [144]. The repetition rates are usually in the range of 50 MHz-1 GHz [63, 64, 84, 102], similar to solid-state lasers. Higher rates are barely possible for fundamental mode-locking since the resonator cannot be made sufficiently short regarding the limited amplification per length of a doped fiber. But by means of harmonic mode-locking, it is possible to increase the repetition rate into the gigahertz range [78, 79]. Here, the impact of non-linearities shrinks with the pulse energy regarding limited amplification by the gain medium. In this case, the quantum noise impact may no longer be stronger than in solid-state lasers anymore but additional challenges arise from supermode noise [144, 145]. Fiber lasers are very practical since the light is confined within a fiber involving less mechanical components than solid-state lasers and making the connection to external devices very simple. Consequently, fiber lasers are more compact,

more robust, easier to operate and have lower costs compared to solid-state lasers [64]. Unfortunately, free space transition within the resonator cannot be completely avoided if, for example, bulk components have to be inserted into the resonator [63, 64].

Semiconductor lasers are based on direct bandgap semiconductors as gain media where carrier inversion causes stimulated emission due to interband transition. The inversion can be induced by electrical or optical pumping. The emitted wavelength can be controlled by bandgap engineering in a certain range. For example, the important telecommunication wavelength can be achieved by an AlGaInAs/InP structure [141]. Such lasers are usually integrated but there are some exceptions where only a semiconductor optical amplifier is embedded in a fiber or free space-based resonator [79]. The average output power is limited to few milliwatts with pulse widths in the picosecond range [79, 141]. The small integrated devices have short resonators and, therefore, achieve very high repetition rates of tens of gigahertz [141]. Their noise characteristics cannot compete with solid-state or fiber lasers and their jitter is usually in the range of few hundreds of femtoseconds or even in the picosecond range [141]. The noise behavior is different to solid-state or fiber lasers because of the very short carrier lifetime and the resulting gain fluctuations [146]. The pulse saturates the gain so that the pulse front experiences more gain than the pulse back. Hence, gain is pushing the pulse forward, while gain fluctuations induce jitter [146]. Furthermore, gain fluctuations are accompanied by group index changes affecting the round trip time as well [146]. The much higher timing jitter of integrated semiconductor lasers compared to solid-state or fiber lasers makes them uninteresting for the jitter-sensitive application of photonic ADCs addressed in this thesis.

In the following, MLL noise characteristics are discussed since the usage of optical pulse trains for photonic ADCs is based on its excellent noise performance. The most relevant pulse train characteristics are the timing jitter and the pulse-to-pulse energy fluctuations or relative intensity noise (RIN), respectively. The laser RIN is specified as the power noise normalized to the average power level [102]. Its SSB PSD $S_{RIN}(f)$ can be measured by an ESA. The unit is 1/Hz but it is more common to use the logarithmic unit dB/Hz. The rms value of the RIN is calculated by integrating this PSD within a given frequency interval [102]

$$\mathrm{RIN} = \sqrt{\int_{f_{min}}^{f_{max}} S_{RIN}\mathrm{d}f}. \tag{5.1}$$

Other fluctuating parameters, such as the pulse width, the optical phase or the chirp are less important. In a laser, all these types of noise are coupled to each other in different ways [148]. The MLL noise properties were successfully described by Haus and Mecozzi by means of the soliton perturbation theory [18]. Later it was shown that the results are more

Reference	MLL type	f_{rep}	$\tau_{o,FWHM}$	P_{opt}	λ_c	σ_{rms} (integration region)	minimal S_{RIN}
[63]	NPE-based strechted-pulse Er-fiber laser	77.6 MHz	60 fs	6.2 mW	1582 nm	70 as (10 kHz-38.8 MHz), 224 as (1 kHz-38.8 MHz)	-
[84]	Fiber taper CNT saturable absorber based soliton Er-fiber laser	80 MHz	400 fs	5.4 mW, 80 mW (after amplifier)	1560 nm	3 fs (10 kHz-40 MHz), 11 fs (1 kHz-40 MHz)	-140 dB/Hz ($f > 1$ MHz)
[64]	NPE-based stretched-pulse Yb-fiber laser	80 MHz	> 30 fs	-	1040 nm	175 as (10 kHz-40 MHz)	-144 dB/Hz ($f > 100$ kHz)
[61]	SESAM-based Er:Yb:glass laser	100 MHz	146 fs	164 mW	1556 nm	83 as (10 kHz-50 MHz)	-157 dB/Hz ($f > 200$ kHz)
[65]	SESAM-based Cr:LiSAF laser	100 MHz	< 100 fs	120 mW	860 nm	30 as (10 kHz-50 MHz)	-149 dB/Hz ($f > 1$ MHz)
[62]	Er:Yb:glass laser	500 MHz	> 180 fs	80 mW	1560 nm	16.3 as (10 kHz-250 MHz)	-150 dB/Hz ($f > 10$ kHz)
[83]	Single-wall CNT saturable absorber based Yb:KYW laser	1.13 GHz	282 fs, 300 fs (after amplifier)	35 mW, 220 mW (after amplifier)	1037 nm	0.7 fs (17.5 kHz-10 MHz)	-127 dB/Hz ($f > 1$ MHz)
[143]	SESAM-based Er:Yb:glass laser	10 GHz	1.5 ps	15 mW	-	135 fs (100 Hz-1.56 MHz), 18.4 fs (6 Hz-1.56 MHz) (using active stabilization)	-
[78]	Actively and harmonically mode-locked Er-fiber laser	10 GHz	1 ps	-	1560 nm	< 5.1 fs (1 kHz-1 MHz), < 9.9 fs (100 Hz-1 MHz), < 153 fs (10 Hz-1 MHz)	-
[79]	Actively and harmonically mode-locked laser	10.287 GHz	< 16 ps < 1.1 ps (after compression)	-	1557 nm	3 fs (1 Hz-100 MHz), 14 fs (1 Hz-5.14 GHz)	-160 dB/Hz ($f > 1$ MHz)
[147]	SESAM-based integrated quantum-dot laser	38.616 GHz		2.8 mW	1310 nm	3.8 ps (10 kHz-1 GHz), 219 fs (10 kHz-1 GHz) (using optical feedback)	-
[141]	SESAM-based integrated laser	40.77 GHz	1 ps	2 mW	1541 nm	1.2 ps (10 kHz-100 MHz)	-

Table 5.1: Comparison of MLLs from publications including their characteristics as far as stated

general and not limited to soliton effects [148, 149]. The noise origin can be categorized as quantum or technical-based. *Quantum noise* is associated with spontaneous emission in the gain section and the resonator loss and its strength are influenced by pulse parameters such as pulse energy, pulse duration and repetition rate [144]. It defines the fundamental noise limit and can only be reduced by higher optical power, longer cavities and shorter pulse widths within the resonator. *Technical noise* arises from various sources such as resonator vibrations, pump excess noise or temperature fluctuations. Its reduction can be achieved by building stable resonators, using a low noise pump source and temperature stabilization.
Gain saturation can accumulate over multiple round-trips leading to the phenomena of relaxation oscillation in solid-state or fiber lasers, while it is negligible in semiconductor lasers [148, 149]. This is due to the much higher saturation energy of the gain medium compared to the intracavity pulse energy. Pump noise induces gain and intensity fluctuations as well [65, 148]. This large excess noise affects the pulse train intensity fluctuations up to the relaxation frequency [148]. The wavelength-dependent gain profile of the gain medium is associated with a phase profile by the Kramers-Kronig relation and induces some amount of dispersion [148, 149]. Hence, gain fluctuations translate into intensity, timing and optical phase noise [83, 148, 149]. Here, the coupling between intensity noise and timing jitter through gain fluctuations depends only on the gain bandwidth [149]. It is stronger for narrow gain bandwidth which coincides with broad pulses [149]. The Kerr effect induces an optical intensity-dependent refractive index change. At the same time there is an intensity-dependent change of the group velocity in the medium through the self-steepening effect [148]. Both affect the temporal pulse position depending on the pulse energy and pulse duration and couple intensity noise to timing jitter [148, 149]. A slow saturable absorber causes a temporal shift of the pulse position because the rising edge is stronger attenuated than the falling edge of the pulse. Since this action depends on the pulse energy, it leads again to coupling between intensity noise and timing jitter [65, 149]. Spontaneous emission noise from the gain medium and linear loss within the resonator can be seen as equivalent to enhanced quantum noise affecting the intensity noise and timing jitter [142, 148, 149]. In general, the noise impact from quantum fluctuations decreases for higher pulse energies. Furthermore, quantum noise has a smaller impact for longer cavities since the interaction with the gain medium and losses are less frequent [149]. The quantum noise from spontaneous emission affects the pulse position in two ways [61, 142, 148, 149]. In the direct mechanism, the center of mass position is shifted in time. In the indirect mechanism, the center wavelength shifts. It results into a group velocity change in the presence of dispersion and affects the round-trip time at the same time. The resulting timing variations are known as *Gordon-Haus jitter* and can only be reduced by minimizing dispersion [63, 64, 84, 142, 149] or the

low frequency part of the center frequency fluctuations by means of a bandwidth-limiting filter [149]. Mechanical vibrations of the cavity mirrors modulate the round-trip time and lead to timing jitter [143, 148, 149]. Moreover, refractive index fluctuations due to thermal effects contribute to timing jitter in the same way [143, 149]. Longer cavities decrease the sensitivity towards mirror vibrations [79, 143].

The design of low jitter MLLs is a highly challenging task regarding the numerous mentioned noise sources. In a well designed MLL, the technical noise is suppressed as far as possible and the circulating pulse is less sensitive towards fluctuations. In this case, quantum noise defines the fundamental noise limit which MLLs achieve, at least for high offset frequency fluctuations. The main contribution to timing jitter is usually concentrated in the low offset frequency components. In particular passive MLLs have stronger drift components of the repetition rate since there is a lack of a timing reference which is provided in active MLLs. In general, the laser noise approaches the shot noise limit for higher intracavity power, lower resonator losses and longer cavities [79].

In the following, the MLLs are classified in three rough categories to simplify the discussion of their applicability for photonic ADCs in the next chapter. These are indicated by colors in tab. 5.1.

In the first category, passive MLLs are grouped which provide the lowest timing jitter. These are highlighted in cyan in tab. 5.1 and are usually solid-state [61, 62, 65] or fiber lasers [63, 64, 84] with long cavities. Here, typical timing jitter values in the low femtosecond [84] or even in the low attosecond regime [61, 62, 63, 64, 65] have been achieved with passive mode-locking. An essential characteristic of such lasers is the short pulse width of $< 400\,\text{fs}$ [61, 62, 63, 64, 65, 84]. The excellent jitter performance is usually achieved for higher offset frequencies of $f_{min} > 1\,\text{kHz}$ with respect to the carrier frequency. Jitter contribution of low offset frequencies can be orders of magnitude higher. Due to the longer round-trip time, the repetition rate of such lasers is usually in the range of $50\,\text{MHz}$-$500\,\text{MHz}$ [61, 62, 63, 64, 65, 84]. For example, for the solid-state $500\,\text{MHz}$ laser in [62], an average output power of $80\,\text{mW}$ with an RIN PSD down to $-150\,\text{dB/Hz}$ was achieved. Similar results were shown for the $100\,\text{MHz}$ MLL in [61] with an average output power of $164\,\text{mW}$ and an RIN PSD down to $-157\,\text{dB/Hz}$. Fiber lasers usually provide lower average output power of down to few milliwatts [63, 84]. Because of this, the RIN is typically higher. For example, in [64, 84] an RIN PSD of $< -140\,\text{dB/Hz}$ was achieved. The output power can always be raised by an external optical amplifier [84] but this deteriorates the RIN further. The mentioned performances were achieved for the important telecommunication wavelength of $1550\,\text{nm}$ [61, 62, 63, 84].

In the second category, fundamentally locked passive MLLs are summarized which provide

repetition rates in the low gigahertz regime corresponding to shorter cavities than lasers of the first category. These are highlighted in yellow in tab. 5.1. Such lasers have higher timing jitter in the low femtosecond regime and are realized as solid-state lasers [83, 143]. This is again valid for high-frequency jitter components above the typical value of 1 kHz. While attosecond jitter seems possible for repetition rates up to 1 GHz [83], such low jitter is much harder to achieve for a one-order-higher repetition rate of 10 GHz. For example, in [143] active stabilization of the cavity length was necessary to decrease the timing jitter to a low femtosecond range. It should be noted that in this case, most jitter contributions resulted from low offset frequency fluctuations of < 1 kHz which are less important for some applications. For example, regarding a photonic ADC in a real-time oscilloscope, the device memory can be filled after 1 ms, and timing jitter which varies slower than 1 kHz becomes irrelevant. In other applications, a PLL corrects slow timing variations. It should be noted that the jitter in [143] was almost quantum-limited and fundamentally locked lasers with higher repetition rates would have an increased timing jitter (assuming the same average optical power) since the quantum noise PSD is inversely proportional to the square of the round-trip time [143, 149]. Here, few or tens of femtoseconds can be found in the literature [143]. The typical pulse width is in the range of few hundreds of femtoseconds [83] or even in the low picosecond range [143].

In the third category, lasers are grouped which provide repetition rates of tens of gigahertz. These are highlighted in green in tab. 5.1. This is usually achieved by integrated semiconductor lasers [141, 147]. Unfortunately, passive mode-locking leads to a much worse jitter performance of hundreds of femtoseconds or even more than one picosecond [141, 147]. Active or hybrid mode-locking decreases the jitter but the requirement of an ultra-stable RF reference is a high cost disadvantage. Optical feedback is a low-cost alternative to decrease the jitter to few hundreds of femtoseconds [147]. Furthermore, integrated lasers emit only a low average output power of few milliwatts [141, 147]. Because of the much worse pulse quality, such MLLs are not interesting for the desired application of a photonic ADC.

An important group of lasers does not fit to the categories mentioned above, namely the harmonically MLLs which are often realized as active lasers. These are not highlighted in color in tab. 5.1. Short cavities have a low quality factor leading to a high timing jitter [141, 143]. But by means of harmonic mode-locking schemes, long cavities enable high quality factors and low timing jitter [79]. Here, supermode noise can be suppressed, for instance by an intracavity Fabry-Perot etalon [79]. External pulse compression is necessary to achieve short pulse widths for active MLLs [78, 79] since the shortening effect of modulators is limited by the RF reference signal. For example, in the active MLL in [78], more than 10000 pulses circulated within a 190 m-long cavity leading to a repetition rate

of $> 10\,\text{GHz}$. Similarly, the active MLL in [79] achieved a repetition rate of $10.287\,\text{GHz}$ from the fundamental frequency of $5.6\,\text{MHz}$ in a $35\,\text{m}$-long cavity. Here, the resulting pulse train showed a timing jitter of only $14\,\text{fs}$ up to the Nyquist frequency and an RIN PSD down to $-160\,\text{dB/Hz}$ for high offset frequency fluctuations. These are impressive results but the MLL is barely suitable as a clock source for photonic ADCs. The complex set-up, including free space transition, an electronic ultra-stable reference signal, a semiconductor optical amplifier and diverse optical and electronic components, makes it impractical for a low-cost solution.

5.1.1 Pulse Repetition Rate Multiplier

Optical pulse trains with desired repetition rates of tens of gigahertz delivered by MLLs usually show insufficient timing stability for high-speed photonic ADCs. The ultra-low jitter performance can be easier achieved by lasers with long cavities or low repetition rates, respectively. Moreover, high power and at the same time high repetition rate can lead to thermal destruction of saturable absorbers. As a result, the desired low jitter pulse trains usually have repetition rates $\ll 10\,\text{GHz}$ and repetition rate multipliers have to be used to achieve higher sampling rates.

One method to increase the repetition rate is *optical time-interleaving*. Here, the pulse train is divided and reunited again with a delay corresponding to half of the pulse period. This process can be repeated multiple times until the desired repetition rate is achieved. It can be realized easily in a cascaded Mach-Zehnder interferometer (MZI) scheme by fibers and couplers [150]. Obvious disadvantages are the high requirements for the coupler splitting ratio and the fiber lengths and the $3\,\text{dB}$ power loss at the last interferometer stage. Coupler tolerances induce periodic amplitude fluctuations, while fiber length tolerances cause periodic timing deviations corresponding to skew. These errors are unavoidable but can be compensated in theory as long as they stay constant and deterministic.

Another method uses an *external Fabry-Perot cavity* at the laser output [151]. Here, the cavity length is locked to a multiple of the laser repetition rate in a feedback loop. In the frequency domain, it corresponds to an optical filter passing only every M-th optical mode, while in the time domain it corresponds to multiplication of the repetition rate by the factor M. Unfortunately, such a filtering process is inefficient since most of the MLL power is reflected back to the laser and is not entering the cavity. Furthermore, a certain amount of non-uniformity within the resulting pulse train cannot be avoided which is indicated by the spurs in the detected electrical spectrum in the realized work in [151].

The third approach is to use *time-to-wavelength mapping* [25]. Here, the pulse train is divided by a spectral demultiplexer in several pulse trains on different carrier wavelengths.

Afterwards, these pulse trains are combined again by means of a spectral multiplexer with characteristic delays similar to the first method [25]. The advantage is that after optical sampling, the different wavelength channels can be easily separated again by a spectral demultiplexer and processed in parallel by low-speed electronics [25]. The disadvantages are again the channel mismatches leading to skew and periodic pulse-to-pulse energy fluctuations although these can be minimized by post-detection electronics as long as they remain constant [25].

Pulse rate multiplication can also be realized by a dispersive medium which is known as the temporal (fractional) Talbot or *self-imaging effect* [152]. Essential characteristics of the dispersive medium is a flat amplitude spectrum and a linear group delay over the entire pulse bandwidth [152]. The linear group delay can be implemented by fibers for picosecond pulses since higher order dispersion effects are not negligible for ultra-short pulses or long fiber lengths [152, 153]. In a simple form it can be realized by an electro-optic phase modulator followed by a dispersive fiber as was done in [153]. Here, the repetition rate multiplication factor can be electrically programmed by modifying the temporal phase modulation profile. An alternative implementation can be performed by linearly chirped fiber gratings [152]. These can be designed to provide the required dispersion characteristics over the desired bandwidth in a compact form. Important advantages of the Talbot-effect-based repetition rate multiplication are pulse shape as well as energy conservation [152, 153] and noise mitigation [154]. Here, each output pulse results from interference of numerous input pulses. Hence, pulse-to-pulse energy fluctuations as well as timing jitter shrinks by the inherent averaging process [154].

The fifth method to increase the repetition rate is to use *all-pass optical ring structures* which can be integrated on chip [155, 156]. Unfortunately, propagation losses in the rings induce severe periodic amplitude fluctuations [156], while temperature sensitivity necessitates a control mechanism. Moreover, a non-negligible pulse broadening is accompanied by the dispersion characteristics of the ring.

5.2 Photonic Analog-to-Digital Converter Architectures

In this section, a short review of principle photonic ADC architectures is given based on previous publications. It is a more detailed discussion of the architecture comparison given by the author in [88]. Based on the conclusions, an analytic investigation of the potential photonic ADC performance will be provided in the next chapter.

An excellent review of realized photonic ADC architectures was given in [24], where the digitization of an RF signal is separated into a sampling and a quantization process. Depending on the ADC architecture, each process can be realized in the photonic or electronic

domain. In fact, the optical contribution can be reduced to clocking the electronics which performs both the sampling and the quantization process.

The original pulse train characteristics provided by an available laser usually have to be modified to enable a reasonable operation. An optical amplifier may be necessary if the output power is too low. The repetition rate may be multiplied by one of the discussed possibilities from section 5.1.1. A time-interleaved scheme of several parallel ADCs is often necessary to achieve high sampling rates. The combinations of all mentioned variants result in a vast variety of photonic ADC architectures. Nevertheless, two principle architectures can be distinguished for the photonic ADC performance analysis in the following chapter.

The resolution of sampled high-frequency microwave signals depends highly on the sampling instant accuracy what can be seen in eq. (2.17). In section 5.1, it has been discussed that MLLs can provide ultra-stable optical pulse trains with timing jitter down to the low attosecond range, which outperforms microwave oscillators. Furthermore, optical clock distribution is more accurate than electrical clock distribution since it induces only a low heat generation, has a high signal speed, is less sensitive towards fabrication tolerances and temperature fluctuations and does not have any impacts from crosstalk and power supply noise [7, 9, 11, 22, 80]. Therefore, it is beneficial to perform the clock distribution and the sampling process in the optical domain. The quantization process can still be realized optically or electronically. But for a low-cost solution, by means of an integrated system on chip, it is more appropriate to consider electronic quantization. In fact, quantization can be performed well by electronics [157] for instance in a photonic BiCMOS process [96].

Typical photonic ADC architectures are illustrated in fig. 5.2. The ADC architecture in fig. 5.2(a) suggests an integrated system on chip where the optical pulse train is coupled into the chip and distributed by an optical CDN to each sampling unit. Photodiodes detect these pulses and generate electric clock signals which initiate the sampling process. Such a system was suggested in [87] by the author where a grating couples the optical pulse train into a silicon waveguide. Multimode interference (MMI) couplers and silicon waveguides with different delays form an optical CDN, delivering these pulses to several time-interleaved sampling units. The steepest point of the rising edge of the induced electrical pulse, as schematically shown in fig. 5.3(a), is used as the sampling instant to trigger the subsequent electronic circuit. Such a clocking mechanism was published in [39] where an optoelectronic clock converter (OECC) generated an electrical $5\,\mathrm{GHz}$ square wave signal from the received $10\,\mathrm{GHz}$ optical pulse train. Here, the optical pulses were detected by a photodiode and the resulting photocurrent pulses induced a switching mechanism of a subsequent flip-flop. The output power of the solid-state MLL used in [39] had to be amplified by an erbium-doped fiber amplifier (EDFA) as suggested in fig. 5.2. Moreover, the repetition rate

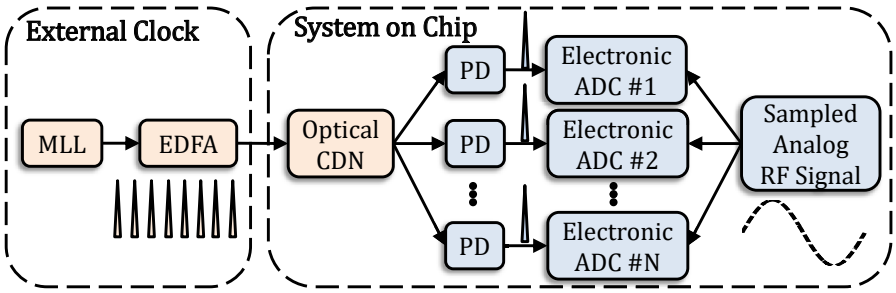

(a)

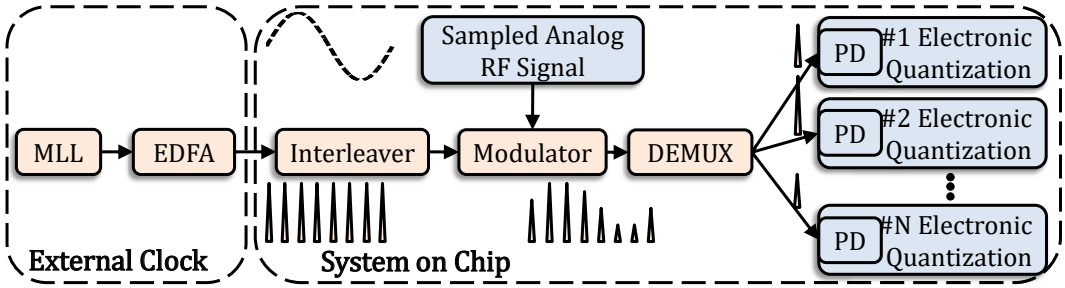

(b)

Figure 5.2: Typical system architectures for photonic ADCs where an external MLL output is amplified by an EDFA and coupled into an integrated system on chip. The optic and electronic components are highlighted by different colors. (a) Using the rising-edge-triggered clocking technique for photonic assisted ADCs (or VLSI circuits), the pulse train is delivered by an optical CDN to the interleaved electronic ADCs defining the sampling instants. (b) Using the center of mass sampling technique, the pulse train is interleaved and weighted by the sampled analog RF signal applied to a modulator. Afterwards, the pulses are demultiplexed and distributed to several photodiodes where they are detected and electronically quantized.

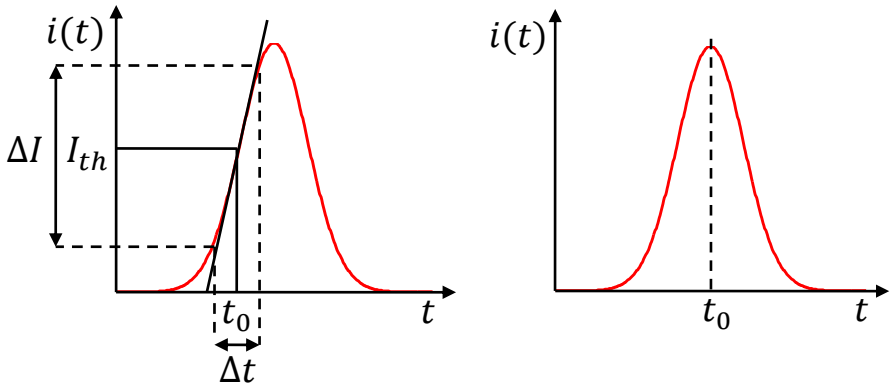

(a) (b)

Figure 5.3: Gaussian pulse shape with two different sampling instants and their uncertainties: (a) Current noise at the threshold value I_{th} at the rising edge with the slope $\Delta I/\Delta t$ at a time instant t_0 corresponds to timing jitter (b) Current noise causes a shift of the pulse center of mass t_0.

of 1.25 GHz was increased by factor 8 by means of optical time-interleaving. The square wave output signal of the OECC can be used as a stable clock for time-interleaved electronic ADCs. A stable time-interleaving can be performed by different waveguide lengths of the optical CDN branches as was suggested in [87] and shown in [80]. The measured OECC timing jitter of 24 fs in the offset frequency range of 1 kHz-30 MHz resulted almost completely from the used MLL and a more stable laser should enable an even better performance. Experimental results of this device will be shown and discussed in detail in section 7.3. Beyond that, the OECC output can be used to clock VLSI circuits. The realized clock mechanism for VLSI circuits in [11] can also be described by the architecture of fig. 5.2(a). In this case, the optical CDN was realized in a symmetrical H-tree architecture to simultaneously clock electronic sub-circuits as illustrated in fig. 1.1(b).

In the ADC architecture of fig. 5.2(b), the sampling process is performed by a modulator, driven by the sampled analog RF signal. In this case, the pulses are weighted by the RF signal and the detected pulse energies refer to the signal amplitude. Here, the sampling instant corresponds to the pulse center of mass as is schematically illustrated in fig. 5.3(b). The pulse train can also be interleaved before passing the modulator and demultiplexed afterwards. Such schemes are usually necessary to achieve high sampling rates but perform the quantization with slow electronics [25]. The receivers either integrate the induced charge per pulse [32, 38] for the quantization process or electrically sample the detected pulse peaks [25]. Since the pulses are broadened after the photodiode and the slope is minimal at the peaks, the electrical jitter is much less critical. Both quantization principles can be found in the literature.

Several studies followed the ADC architecture of fig. 5.2(b). In [38], the optical interleaving

system is realized in free-space, while photoconductive switches perform the sampling process of the RF signal. The pulse weighting process is performed by a metal-semiconductor-metal switch attached in series with a hold capacitor across the signal and ground lines of a transmission line. Then, the applied voltage charges a hold capacitor when the photoexcited carriers open the sampling window. A subsequent flash quantizer digitizes the held voltage after amplification by a buffer amplifier. In this case, no demultiplexing schemes were used. It should be noted that other than in fig. 5.2(b), the sampling process is performed electrically but the timing jitter also coincides with the center of mass uncertainty indicated in fig. 5.3(b). In the proposed photonic ADC in [25], the interleaving concept is realized by time-to-wavelength mapping as described in section 5.1.1. After weighting the pulses by an electro-optic modulator, the interleaved pulse train is demultiplexed into individual wavelengths and detected by separate photodiodes. Subsequent post-detection electronics generates the digital output. Here, amplitude and timing mismatches between the channels, resulting from the interleaving system and the photodiodes, as well as modulator non-linearity are corrected by digital signal processing. In [32], after passing the sampling modulator, the pulses are distributed by time-division demultiplexers to the individual photodetectors. The sampling process in the non-integrated work in [34] is also performed by a modulator and, therefore, its uncertainty can also be modeled by the quantum noise model introduced in the following chapter. The time- [32] or wavelength-demultiplexing scheme [25] after sampling by a modulator is beneficial since it strongly relaxes bandwidth requirements for photodetectors and electronic quantizers. This means that the comparator ambiguity, as another critical issue for electronic ADCs, is much less problematic. The modulator non-linearity as well as the laser amplitude noise can be largely suppressed by using the information of both modulator output arms [32, 158] as long as the subsequent system components remain linear. Here, using a combination of both outputs and the inversion of the modulator transfer function during post-processing leads to suppressed sensitivity towards pulse-to-pulse energy fluctuations. The disadvantage is the twice-as-high system complexity consisting of waveguides, MMIs, photodiodes, quantizer circuits and post-detection electronics. In [159], the pulse weighting is performed in the electronic domain after photodetection of the optical pulse train. As will be shown in the following chapter, the timing uncertainty of such a sampling process corresponds also to the center of mass of the optical pulse.

The external MLL has to be synchronized with the electronics on chip. Here, either the MLL or an RF reference can serve as the master clock. Derivation of a precise high frequency clock on chip from an MLL was shown in [39] and considered in [25, 32, 38] . But in this case, part of the laser power has to be reserved for the clock generation on chip. This is avoided if an RF reference serves as the master clock. Here, the laser cavity length can be

adjusted by means of a piezoelectric transducer to a reference signal. This is widely used in ultra-low jitter measurement systems [61, 62, 63, 64, 82, 83, 84, 143]. Passive MLLs are usually considered for photonic sampling due to their ultra-low jitter performance for higher offset frequency fluctuations. The usually much higher slow frequency jitter can be filtered by locking the laser within a PLL to a slow reference. In this case, the jitter during the fast photonic sampling process is dominated by high offset frequency fluctuations of the lasers repetition rate. Moreover, the jitter requirements for the quantization process are much less stringent due to the parallel architecture. Therefore, the slow drift is not critical for the electronics and is filtered by the PLL.

Chapter 6

Jitter of Photonic Analog-to-Digital Converters

In the following, a quantum noise model is introduced capable of describing fundamental noise source impacts on the photonic ADC performance. It was published by the author in [88] as an evolved model from previous versions introduced in [87, 160]. In this chapter, a more detailed derivation is given.
An integrated system on chip is considered where the quantization is performed electrically, while the sampling process can be done either electrically or optically. An external MLL is considered for providing the pulse train which can be optionally amplified by an EDFA. Assuming reasonable properties for individual components of the whole system, the potential performance of photonic ADCs will be discussed for both sampling methods mentioned in section 5.2.

6.1 Quantum Noise Model of Photodetection

A block diagram of the system model is shown in fig. 6.1 where all parameters in front of the photodetector (PD) are related to the optical field. An MLL with negligible jitter σ_{MLL} is considered, emitting ultra-short optical pulses with a complex optical field envelope $A(t)$ and the pulse energy $E_p = \int |A(t)|^2 \mathrm{d}t$. The actual time-dependent electrical field would be $\mathrm{Re}\{A(t) \cdot \exp(j2\pi\nu_c t)\}$ where ν_c is the carrier frequency related to the carrier wavelength by $\lambda_c = c/\nu_c$ with c as the speed of light in vacuum. A subsequent EDFA amplifies the pulse energy by a factor G. This process adds noise $n_{ASE}(t)$ due to amplified spontaneous emission (ASE) noise. It is complex and can be described by the ACF [101, 161]

$$R_{ASE}(\tau) = \langle n_{ASE}(t) n^*_{ASE}(t+\tau) \rangle = n_{sp} h \nu_c (G-1) \cdot \delta(\tau) \tag{6.1}$$

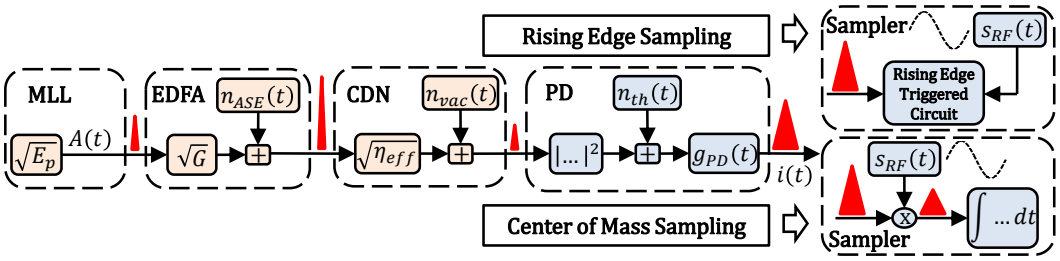

Figure 6.1: Detailed block diagram of the system model for quantum noise calculation in the photonic sampling process. All variables in front of the PD are related to the electrical field amplitude. Optical and electrical signal paths are highlighted by different colors. The PD output can be used for two principle sampling techniques mentioned in the text.

where n_{sp} is the EDFA inversion factor, h is Planck's constant and "*" denotes the complex-conjugate. As the direct impact, it causes the pulse center of mass to shift in time. Furthermore, it induces a slight change of the pulse center frequency, leading to a group velocity change. In combination with dispersion of the optical path, it leads to a varying arrival time at the end of the optical path which corresponds to an indirect impact on jitter. The effect of a varying center frequency and fiber dispersion is known as *Gordon-Haus jitter* σ_{GH}. It had been first described in [162] and later analyzed for long-haul fiber communication systems in [163] where the effect was extended by the pulse chirp impact on jitter. In the following, the Gordon-Haus jitter is neglected, while the direct impact on the center of mass is included in the noise model. The indirect impact of ASE noise on jitter is subsequently considered as superimposed additional mean squared jitter [161]

$$\begin{aligned}\sigma_{GH}^2 &= \frac{S_{ASE}}{GE_p}\tau_o^2\left(\frac{d}{\tau_o^2}+C_0\right)^2 \\ &= \frac{(FG-1)h\nu_c}{2GE_p}\tau_o^2\left(\frac{d}{\tau_o^2}+C_0\right)^2.\end{aligned} \tag{6.2}$$

Here, $S_{ASE} = n_{sp}h\nu_c(G-1)$ is the PSD of the ASE noise, C_0 is the chirp parameter regarding linear frequency change and $d = \overline{\beta_2}L$ is the accumulated dispersion in the fiber of a length L with the average group velocity dispersion (GVD) coefficient $\overline{\beta_2}$. The more practical EDFA noise figure [161, 101]

$$F = \frac{\mathrm{SNR}|_{\mathrm{in}}}{\mathrm{SNR}|_{\mathrm{out}}} = \frac{1}{G}(1+2n_{sp}(G-1)) \tag{6.3}$$

has been used to replace the inversion coefficient n_{sp} and τ_o is the pulse width of the Gaussian optical power envelope from eq. (4.15). Eq. (6.2) was derived for long-haul transmission systems with a fiber length much longer than the fiber length within the EDFA. In the investigated application of photonic ADCs, the fiber to the chip is very short and the sum of the EDFA fiber and the output fiber can be taken as an upper bound of the effective fiber

length L. As a practical example, an MLL can be considered, emitting pulses with a pulse energy of $E_p = 0.1\,\text{pJ}$, a center wavelength of $\lambda_c = 1550\,\text{nm}$, a pulse width of $\tau_o = 180\,\text{fs}$ (or $300\,\text{fs}$ full-width-half-maximum (FWHM) respectively) and a chirp of $C_0 = 1$. An EDFA with the noise figure $F = 4$ amplifies the pulses by factor $G = 100$. For an optical path with the average GVD coefficient $\overline{\beta_2} = 20\,\text{ps}^2/\text{km}$ and the effective length $L = 10\,\text{m}$, the Gordon-Haus jitter would be $\sigma_{GH} = 2.07\,\text{fs}$. If necessary, the Gordon-Haus jitter can be decreased by minimizing the accumulated dispersion which is usually done in MLLs [63, 64].

After amplification by the EDFA, the pulse train is coupled into the optical CDN and distributed to certain positions on the silicon die. The CDN can look very different depending on the sampler architecture which has been discussed in section 5.2. Here, its impact can be reduced to the overall loss α_{CDN}. The photodiode quantum efficiency η_{PD} and the efficiency of the optical CDN including grating coupler, MMI couplers, waveguides or other passive components can be summarized to the effective efficiency $\eta_{eff} = \eta_{PD}\alpha_{CDN}$. Superimposed vacuum fluctuations $n_{vac}(t)$ added to the optical field in front of the photodiode model the shot noise. These are complex and can be modeled by the ACF [101, 161]

$$R_{vac}(\tau) = \langle n_{vac}(t) n_{vac}^*(t+\tau)\rangle = \frac{h\nu_c}{2}\cdot\delta(\tau). \tag{6.4}$$

Here, $h\nu_c/2$ refers to the zero-point energy [101]. Finally, the PD is represented by the concatenation of a square law detector and a linear system with the impulse response $g_{PD}(t)$ normalized by $\int g_{PD}(t)\mathrm{d}t = 1$. Thermal noise of an effective load resistance R_Ω at the PD is included by the current noise $n_{th}(t)$. Its ACF is known as [101]

$$R_{th}(\tau) = \langle n_{th}(t) n_{th}(t+\tau)\rangle = \frac{4k_BT}{R_\Omega}\cdot\delta(\tau). \tag{6.5}$$

Following the block diagram in fig. 6.1, the output current results in

$$\begin{aligned} i(t) =& R_p\left|\sqrt{G\eta_{eff}}A(t) + \sqrt{\eta_{eff}}n_{ASE}(t) + n_{vac}(t)\right|^2 * g_{PD}(t) + n_{th}(t) * g_{PD}(t) \\ =& R_p\Bigg(G\eta_{eff}|A(t)|^2 + 2\,\mathrm{Re}\left\{\sqrt{G\eta_{eff}}A(t)\cdot\left(\sqrt{\eta_{eff}}n_{ASE}(t) + n_{vac}(t)\right)\right\} \\ &+ \left|\sqrt{\eta_{eff}}n_{ASE}(t) + n_{vac}(t)\right|^2\Bigg) * g_{PD}(t) + n_{th}(t) * g_{PD}(t). \end{aligned} \tag{6.6}$$

$R_p = q/h\nu_c$ is the response of an ideal photodiode and q is the electron charge. The beatings of the pulse with ASE noise and vacuum fluctuations is dominant compared to the contribution of the beating of ASE noise with vacuum fluctuations. Therefore, the third addend can be neglected towards the second in the brackets of eq. (6.6). In summary, the detected electrical signal is a superposition of a deterministic photocurrent $i_d(t)$ and the

noise currents $i_{n,opt}(t)$ and $i_{n,th}(t)$ resulting from the noise sources mentioned above. The output current can be expressed as [87, 88]

$$i(t) = i_d(t) + i_{n,opt}(t) + i_{n,th}(t) \qquad \text{with} \tag{6.7}$$

$$i_d(t) = R_p G \eta_{eff} |A(t)|^2 * g_{PD}(t) \tag{6.8}$$

$$\begin{aligned} i_{n,opt}(t) &= i_{n,ASE}(t) + i_{n,vac}(t) \\ &= \Big[2R_p\sqrt{G}\eta_{eff}\,\mathrm{Re}\{A(t)\cdot n_{ASE}(t)\}\Big] * g_{PD}(t) \\ &\quad + \Big[2R_p\sqrt{G\eta_{eff}}\,\mathrm{Re}\{A(t)\cdot n_{vac}(t)\}\Big] * g_{PD}(t) \end{aligned} \tag{6.9}$$

$$i_{n,th}(t) = n_{th}(t) * g_{PD}(t). \tag{6.10}$$

Based on the introduced noise model, the fundamental jitter limit for both photonic sampling techniques introduced in section 5.2 will be calculated in the next sections.

6.2 Rising Edge Sampling

One way to exploit the ultra-low jitter performance of MLLs for the sampling process is to use the steepest point of the rising edge of the induced electrical pulses as the sampling instant. This was realized in [11, 39]. In digital electronic circuits, a potential barrier, such as a threshold voltage of a transistor, has to be exceeded to switch a circuit state [56]. In this case, the superimposed noise currents at the threshold current I_{th} induce an uncertainty of the time instant t_0 what is schematically shown in fig. 5.3(a). Here, the standard deviation of this time instant corresponds to jitter [56]. For its following derivation, a Gaussian PD impulse response

$$g_{PD}(t) = \frac{1}{\sqrt{\pi}\tau_e} \cdot e^{-\frac{t^2}{\tau_e^2}} \tag{6.11}$$

is assumed with τ_e as the impulse response widths.
The superimposed stochastic photo current $i_{n,opt}(t)$ has a zero mean value so that the variance can be calculated to [164]

$$\mathrm{var}\left(i_{n,opt}(t)\right) = 4R_p^2 G\eta_{eff} \int_{-\infty}^{\infty} A^2(\tau) g_{PD}^2(t-\tau) R_{nn}(0)\mathrm{d}\tau. \tag{6.12}$$

Here, the ACF value

$$R_{nn}(0) = \eta_{eff}\frac{R_{ASE}(0)}{2} + \frac{R_{vac}(0)}{2} \tag{6.13}$$

represents the sum of ACF values of both optical noise sources at $\tau = 0$. Due to the square law detection, only the real part of the noise sources can be found in eq. (6.9) so that only the half value of the ACFs in eqs. (6.4) and (6.1) are used in eq. (6.13).

The variance of the thermal noise $i_{n,th}(t)$ has a zero mean value as well and is well known as [101]

$$\text{var}(i_{n,th}(t)) = \frac{4k_BT}{R_\Omega} B_{PD} \tag{6.14}$$

with B_{PD} as the 3 dB PD bandwidth. For a first order timing jitter estimation, linearization of the impulse response $g_{PD}(t)$ around the threshold value I_{th} by the signal slope can be used. This is schematically shown in fig. 5.3(a) and leads to

$$\text{var}(t_0) = \frac{\text{var}(I_{th})}{\left(\frac{\mathrm{d}i_d(t)}{\mathrm{d}t}\Big|_{t=t_0} \right)^2} \tag{6.15}$$

with $\text{var}(I_{th})$ as the current variance at the threshold value. Inserting the current variance due to ASE noise and shot noise from eq. (6.12) or the current variance due to thermal noise from eq. (6.14), respectively, in eq. (6.15) results into the mean squared jitter contributions of shot and ASE noise and thermal noise [87, 88]

$$\sigma^2_{e,opt} = \frac{h\nu_c}{E_{p,PD}} \left[1 + \eta_{eff}(GF - 1)\right] \cdot \frac{(\tau_e^2 + \tau_o^2)^3}{4\ln(2)\tau_e^3\sqrt{\tau_e^2 + 2\tau_o^2}} \cdot e^{-\frac{2\ln(2)\tau_e^2}{2\tau_o^2+\tau_e^2} + \frac{2\ln(2)\tau_e^2}{\tau_o^2+\tau_e^2}}, \tag{6.16}$$

$$\sigma^2_{e,th} = \frac{4k_BT}{R_p^2 E_{p,PD}^2 R_\Omega} \cdot 0.83\tau_e^3 \quad \text{with} \tag{6.17}$$

$$E_{p,PD} = \eta_{eff} G E_p \tag{6.18}$$

as the detected pulse energy at the PD. For the 3 dB bandwidth in eq. (6.14), the relation $\tau_o = \sqrt{\ln 2}/\sqrt{2}\pi B_{PD}$ has been used. It is valid for Gaussian pulse forms and, therefore, also for the bandwidth of the considered Gaussian PD impulse response in eq. (6.11). The impact of ASE noise results into the expression in the first brackets of eq. (6.16). Jitter that originates from shot and ASE noise in eq. (6.16) decreases for higher detected pulse energy $E_{p,PD}$, shorter optical pulse width τ_o and shorter PD impulse response τ_e or higher PD bandwidth, respectively. Jitter from thermal noise decreases faster for a higher detected pulse energy and a shorter PD impulse response width due to the squared and cubic dependencies in eq. (6.17). Depending on the magnitude of the detected pulse energy, both noise sources can dominate.

Unavoidable relative pulse-to-pulse energy fluctuations Δr_{p2p} transfer to timing jitter of the time instant t_0 in fig. 5.3(a) since the threshold current is reached earlier or later depending on the detected pulse energy. Assuming the usual case of $\tau_o \ll \tau_e$, this transition instant of the half peak value as a reference point at the PD impulse response in eq. (6.11) can be

calculated by

$$\frac{1}{2}\frac{1}{\sqrt{\pi\tau_e}} = \frac{1+\Delta r_{p2p}}{\sqrt{\pi\tau_e}} \cdot e^{-\frac{t'^2}{\tau_e^2}}$$
$$\Leftrightarrow t' = \tau_e \cdot \sqrt{\ln(2+2\Delta r_{p2p})}. \tag{6.19}$$

Using a first order Taylor approximation for the time instant variation t' due to pulse energy fluctuations Δr_{p2p} and calculating its deviation from the expected value $t_0 = \sqrt{\ln(2)}\tau_e$ results in the corresponding timing jitter

$$\sigma_{e,p2p} = \frac{\Delta r_{p2p}}{2\sqrt{\ln 2}}\tau_e \tag{6.20}$$

where the relative pulse-to-pulse energy fluctuations

$$\Delta r_{p2p} = \frac{\Delta E_p}{E_p} = \sqrt{\int_0^{f_{rep}/2} S_{RIN}(f)\mathrm{d}f} \tag{6.21}$$

within the pulse train can be calculated from the RIN PSD of the MLL. The integration is performed up to the Nyquist frequency corresponding to half of the repetition rate f_{rep}. A RIN PSD of -155 dB/Hz for a 10 GHz MLL results in $\Delta r_{p2p} = 0.13\%$ at the MLL output. Considering a subsequent EDFA with the noise figure $F_{dB} = 6$ dB and the amplification $G_{dB} = 20$ dB followed by a CDN with the effective efficiency $\eta_{eff} = -17$ dB results in the total noise figure [101]

$$F_{tot} = F + \frac{1/\eta_{eff} - 1}{G} \tag{6.22}$$

where all variables are given by their explicit values and not in dB. The EDFA and the subsequent CDN increases the RIN PSD by the total noise figure. For the upper example, the concatenated noise figure results in $F_{tot,dB} = 6.5$ dB and leads to shot noise limited relative pulse-to-pulse energy fluctuations of $\Delta r_{p2p} = 0.27\,\%$ at the photodiode. This causes a timing jitter of $\sigma_{e,p2p} = 7.96$ fs for a Gaussian PD impulse response width of $\tau_e = 5$ ps corresponding to $B_{PD} = \sqrt{\ln(2)}/\sqrt{2}\pi\tau_e = 37.5$ GHz PD bandwidth. It is important to note that eq. (6.20) is only valid for linear photodiodes. Using the photodiodes in saturation, pulse-to-pulse energy fluctuations affect the rising edge much less compared to the falling edge [77] as has been shown in section 4.5. In this case, pulse-to-pulse energy fluctuations should be less critical for the timing jitter. The measured additional jitter for photodiodes in saturation resulting from amplitude-to-phase noise conversion [77] does not apply for the rising edge case since an ESA always measures the center of mass. The impact on the center of mass is much higher. In conclusion, the performance of the rising edge sampling technique depends highly on the detected pulse energy and the PD bandwidth, according to eqs. (6.16), (6.17) and (6.20). The impact of pulse-to-pulse energy fluctuations on timing jitter in eq. (6.20) shows an upper bound and photodiode saturation can even be beneficial.

6.3 Center of Mass Sampling

In ADC architectures as proposed in [25] or in several architectures suggested in [24], the sampling process is performed by weighting the optical pulse train by the RF signal which has to be sampled. Afterwards, the discretized signal can be derived from the detected pulse energies $E_{p,PD}$ as schematically shown in fig. 5.2(b). In this case, jitter results from the uncertainty of the center of mass position due to random photon distribution within the pulse. The Poisson distribution describes noise resulting from the particle nature of light [165]. For the usual case of a large number of photons, the noise characteristics correspond to Gaussian noise superimposed to the deterministic signal. Describing this noise in the wave form of light leads to vacuum fluctuations which are used in the quantum noise model in section 6.1. In the following derivation, Gaussian optical pulses as written in eq. (4.15) are assumed.

Following the ansatz in eq. (6) in [149], the shifted pulse center of mass position due to a noise current $i_{n,opt}(t) = i_{n,ASE}(t) + i_{n,vac}(t)$ superimposed to a deterministic photocurrent $i_d(t)$, given in eqs. (6.8) and (6.9), can be calculated by

$$\begin{aligned}\sigma_c^2 &= \frac{1}{Q^2}\left\langle \left(\int_{-\infty}^{\infty} t \cdot i_{n,opt}(t)\mathrm{d}t \right)^2 \right\rangle \\ &= \frac{1}{Q^2}\left\langle \left(\int_{-\infty}^{\infty} t \cdot i_{n,opt}(t)\mathrm{d}t \right) \left(\int_{-\infty}^{\infty} t' \cdot i_{n,opt}(t')\mathrm{d}t' \right) \right\rangle \end{aligned} \tag{6.23}$$

where

$$Q = \int_{-\infty}^{\infty} i_d(t)\mathrm{d}t = R_p E_{p,PD} \tag{6.24}$$

is the detected charge induced by the optical pulse. The beating term between shot noise $i_{n,vac}(t)$ and ASE noise $i_{n,ASE}(t)$ disappears in eq. (6.23) since the noise sources are not correlated. Therefore, the jitter calculations due to vacuum fluctuations (or shot noise respectively) and ASE noise can be split. In the following, the derivation of the jitter contribution from shot noise $i_{n,vac}(t)$ is provided. The calculation steps are identical for ASE noise related jitter taken into account by $i_{n,ASE}(t)$. The result will be given by a simple adaptation of relevant factors. For shot noise eq. (6.23) leads to

$$\begin{aligned}\sigma_{c,sh}^2 = \frac{K^2}{Q^2}\Bigg\langle \int_{-\infty}^{\infty}\int_{-\infty}^{\infty} tt' \left[\int_{-\infty}^{\infty} \mathrm{Re}\{A(\tau)\cdot n_{vac}(\tau)\} \cdot g_{PD}(t-\tau)\mathrm{d}\tau \right] \cdot \\ \left[\int_{-\infty}^{\infty} \mathrm{Re}\{A(\tau')\cdot n_{vac}(\tau')\} \cdot g_{PD}(t'-\tau')\mathrm{d}\tau' \right] \mathrm{d}t'\mathrm{d}t \Bigg\rangle \end{aligned} \tag{6.25}$$

with $K = 2R_p\sqrt{G\eta_{eff}}$. In the following, a real optical field envelope is assumed for the optical pulse. Thus, reorganizing eq. (6.25) results in

$$\sigma_{c,sh}^2 = \frac{K^2}{Q^2}\int_{-\infty}^{\infty}\int_{-\infty}^{\infty} tt'\Bigg[\int_{-\infty}^{\infty}\int_{-\infty}^{\infty} A(\tau)A(\tau')\left\langle \mathrm{Re}\{n_{vac}(\tau)\}\,\mathrm{Re}\{n_{vac}(\tau')\}\right\rangle \cdot g_{PD}(t-\tau)g_{PD}(t'-\tau')\mathrm{d}\tau\mathrm{d}\tau'\Bigg]\mathrm{d}t'\mathrm{d}t. \tag{6.26}$$

Only the real part of the vacuum fluctuations appears in the ensemble average in eq. (6.26). Since the PSD of the vacuum fluctuations is distributed equally in the real and imaginary part [101], only half of the ACF from eq. (6.4) has to be used. Therefore, eq. (6.26) leads to

$$\begin{aligned}\sigma_{c,sh}^2 &= \frac{K^2}{Q^2}\frac{h\nu_c}{4}\int_{-\infty}^{\infty}\int_{-\infty}^{\infty} tt'\Bigg[\int_{-\infty}^{\infty} A^2(\tau)\cdot g_{PD}(t-\tau)g_{PD}(t'-\tau)\mathrm{d}\tau\Bigg]\mathrm{d}t'\mathrm{d}t\\ &= \frac{K^2}{Q^2}\frac{h\nu_c}{4}\int_{-\infty}^{\infty} t\Bigg[\int_{-\infty}^{\infty} A^2(\tau)\cdot g_{PD}(t-\tau)\left(\int_{-\infty}^{\infty} t'\cdot g_{PD}(t'-\tau)\mathrm{d}t'\right)\mathrm{d}\tau\Bigg]\mathrm{d}t\\ &= \frac{K^2}{Q^2}\frac{h\nu_c}{4}\int_{-\infty}^{\infty}\tau\cdot A^2(\tau)\left(\int_{-\infty}^{\infty} t\cdot g_{PD}(t-\tau)\mathrm{d}t\right)\mathrm{d}\tau.\end{aligned} \tag{6.27}$$

Here, the relation that the normed impulse response $\int g_{PD}(t)\mathrm{d}t = 1$ is centered at $t = 0$ has been used twice and, therefore, the mean value of its shifted version $g_{PD}(t-\tau)$ corresponds to the time shift τ. Finally, using the Gaussian pulse shape from eq. (4.15) for the optical pulse power envelope $A^2(t)$ in eq. (6.27) results in the shot-noise-induced mean squared timing jitter

$$\sigma_{c,sh}^2 = \frac{h\nu_c}{2E_{p,PD}}\tau_o^2. \tag{6.28}$$

The ASE noise contribution to timing jitter can be calculated identically to

$$\sigma_{c,ASE}^2 = \eta_{eff}(FG-1)\frac{h\nu_c}{2E_{p,PD}}\tau_o^2 \tag{6.29}$$

by using the corresponding ACF from eq. (6.1) and a slightly different factor K. Moreover, the expression in eq. (6.3) has been used to replace the inversion factor by an expression with the more practical noise figure F. The jitter in eqs. (6.28) and (6.29) is additive and results in [88]

$$\sigma_{c,opt}^2 = \frac{1}{2}\frac{h\nu_c}{E_{p,PD}}\tau_o^2\left[1+\eta_{eff}(GF-1)\right]. \tag{6.30}$$

since the noise sources are not correlated. Eq. (6.30) represents the variance of the center of mass position of the induced electrical pulses due to the current noise $i_{n,opt}(t)$ superimposed

to the ideal photocurrent $i_d(t)$. Without the EDFA ($F = G = 1$) and the CDN, the effective efficiency reduces to the photodiode quantum efficiency $\eta_{eff} \to \eta_{PD}$ and eq. (6.30) reduces to

$$\sigma_{c,sh}^2 = \frac{1}{2}\frac{h\nu_c}{\eta_{PD}E_p}\tau_o^2. \tag{6.31}$$

It describes the mean squared center of mass jitter resulting from shot noise in the photodetection of an optical pulse train. This equation was first derived in [69] and shows that the center of mass jitter of the induced electrical pulses does not depend on the PD bandwidth. Jitter increase due to the photodiode stems only from the limited quantum efficiency η_{PD}. Furthermore, only the optical pulse characteristics define the jitter from shot and ASE noise. The higher the pulse energy and the shorter the pulse width, the less jitter is generated. In [69], the derived relation was explained by shot noise correlations in the photodetection process of an optical pulse train. Here, identical results are shown with the intuitive explanation of pulse center of mass variation analyzing the photodetection of a single pulse. In the upper derivation, shot noise is considered by optical field fluctuations and a deterministic PD impulse response from eq. (6.11) is used. Therefore, the unique random variable that causes jitter depends only on the optical pulse characteristics. The PD, as a deterministic component, deteriorates the jitter performance only by the non-ideal quantum efficiency. Limits of this approach were observed in [69] where the measured phase noise of an induced harmonic did not decrease further for shorter pulses after reaching a certain level. This effect was explained in [133] by the random carrier drift time within the intrinsic region of the photodiode. A random drift time causes a non-deterministic PD impulse response and leads to a certain amount of jitter. In [69], this value was $0.8\,\text{fs}$ corresponding to the measured phase noise of $-179\,\text{dBc/Hz}$ for the fifth harmonic of the used repetition rate of $2\,\text{GHz}$.

The noise model introduced here can also be used to calculate the jitter of the optical pulse in front of the PD. In this case, the PD can be reduced to a square law detector leading to an optical power instead of a photocurrent in the upper derivation. Then, eq. (6.31) with $\eta_{PD} = 1$ is consistent with the results found in [149, 166]. It is noteworthy that for other pulse shapes, eq. (6.30) would have slightly different factors than $1/2$, as can be seen in [167, 168].

The detected pulse energies $E_{p,PD}$ or induced charges $R_pE_{p,PD}$, respectively, refer to the sampled signal amplitudes after being scaled by the sampled analog signal $s_{RF}(t)$. This is indicated for the electrical center of mass sampling principle in fig. 6.1. Consequently, pulse-to-pulse energy fluctuations affect the sampled amplitudes directly. The relative uncertainty of the detected pulse energy can be described by eq. (6.21) considering RIN deterioration by the EDFA and the effective CDN efficiency according to eq. (6.22). In the

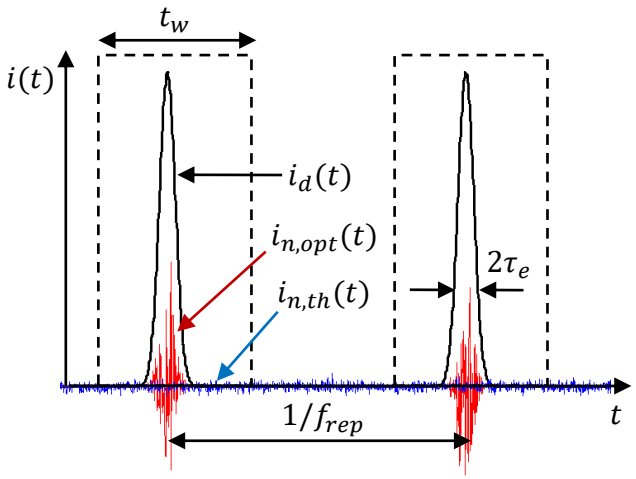

Figure 6.2: The detected pulse energies are integrated during a time window t_w. Noise currents are superimposed to the deterministic photocurrent.

example at the end of section 6.2, the detected relative pulse-to-pulse energy fluctuations of $\Delta r_{p2p} = 0.27\%$ are higher than the quantization noise $r_q = 2^{-N} = 0.002$ of an $N = 9$ bit ADC.

The ultra-low jitter performance of the pulse train after photodetection depends on the conservation of the photon distribution statistics, given by the ultra-short optical pulse. Photodiode saturation destroys these statistics, and amplitude-to-phase noise conversion in the photodiode increases the timing jitter further [77]. In conclusion, the center of mass sampling technique in the electrical domain requires linear photodiodes, tolerating as high pulse energy as possible. High power-handling photodiodes integrated on silicon waveguides can be found in [131]. In [80], an optically induced electrical pulse train with femtosecond precision was measured at the output of a waveguide-integrated photodiode. Since a linear photodiode affects the jitter in eq. (6.30) only by the quantum efficiency, it is reasonable to use a lower photodiode bandwidth to avoid high current peaks and saturation effects. Thermal noise in the PD further deteriorates the performance. For the electrical center of mass sampling in fig. 6.1, it is considered to scale the induced electrical pulses by the sampled RF signal $s_{RF}(t)$ and subsequently to integrate the induced and scaled charges. Such a sampler has been recently realized in [159]. Thermal noise $i_{n,th}(t)$ as well as shot and ASE noise $i_{n,opt}(t)$ superimposed to the deterministic current pulse $i_d(t)$ affect the value of the integrated charge. This is illustrated in fig. 6.2 where the electrical current is integrated during a time window t_w. Integration of a noise current $i_{n,th}(t)$ on a capacity C over a time interval t_w results in a random walk characteristic of the integrated voltage uncertainty [56]

$$\left\langle v_{n,th}^2 \right\rangle = \frac{2k_BT}{R_\Omega}\frac{t_w^2}{C^2}\int\limits_{-\infty}^{\infty}\left|\frac{\sin(\pi f t_w)}{\pi f t_w}\right|^2 |G_{PD}(f)|^2\,\mathrm{d}f \leq \frac{2k_BT}{R_\Omega C^2}t_w. \tag{6.32}$$

In the integral of eq. (6.32), a higher PD bandwidth is assumed compared to the bandwidth of the rectangular integration window. In this case, the filter effect of $G_{PD}(f)$ can be neglected. This leads to a relative amplitude uncertainty of

$$\Delta r_{th} \leq \frac{\sqrt{\left\langle v_{n,th}^2 \right\rangle}}{U_p} = \frac{\sqrt{2k_BTt_w/R_\Omega}}{R_pE_{p,PD}} \tag{6.33}$$

where $U_p = Q/C$ corresponds to the integrated charge $Q = R_pE_{p,PD}$ at the capacity C, induced by the optical pulse. Such an electronic circuit has been realized in [159].

In addition, the pulse train jitter characteristics are also affected by thermal noise. This impact can be assessed by calculating the center of mass shift due to thermal current noise as has been done in eq. (6.23) for the current noise stemming from shot and ASE noise. Replacing the current noise $i_{n,opt}(t)$ in eq. (6.23) by the thermal current noise $i_{n,th}(t)$ from eq. (6.10) results in

$$\begin{aligned}
\sigma_{c,th}^2 &= \frac{1}{Q^2}\left\langle \left(\int\limits_{-\frac{t_w}{2}}^{\frac{t_w}{2}} t\cdot i_{n,th}(t)\mathrm{d}t \right)^2 \right\rangle \\
&= \frac{1}{Q^2}\left\langle \int\limits_{-\infty}^{\infty} t\cdot \sqcap_{t_w}(t)\cdot\left[\int\limits_{-\infty}^{\infty} n_{th}(\tau)\cdot g_{PD}(t-\tau)\mathrm{d}\tau\right]\mathrm{d}t\cdot \right. \\
&\qquad \left. \int\limits_{-\infty}^{\infty} t'\cdot \sqcap_{t_w}(t')\cdot\left[\int\limits_{-\infty}^{\infty} n_{th}(\tau')\cdot g_{PD}(t'-\tau')\mathrm{d}\tau'\right]\mathrm{d}t' \right\rangle \\
&= \frac{1}{Q^2}\int\limits_{-\infty}^{\infty}\int\limits_{-\infty}^{\infty} tt'\sqcap_{t_w}(t)\sqcap_{t_w}(t')\cdot \\
&\qquad \left[\int\limits_{-\infty}^{\infty}\int\limits_{-\infty}^{\infty} g_{PD}(t-\tau)g_{PD}(t'-\tau')\langle n_{th}(\tau)n_{th}(\tau')\rangle\mathrm{d}\tau\mathrm{d}\tau'\right]\mathrm{d}t\mathrm{d}t'.
\end{aligned} \tag{6.34}$$

Now, by means of the ACF from eq. (6.5) and the Gaussian PD impulse response from eq. (6.11), the expression within the rectangular brackets can be solved. Then eq. (6.34) leads to

$$\begin{aligned}
\sigma_{c,th}^2 &= \frac{4k_BT}{R_\Omega Q^2}\int\limits_{-\frac{t_w}{2}}^{\frac{t_w}{2}}\int\limits_{-\frac{t_w}{2}}^{\frac{t_w}{2}} tt'\cdot\left(\frac{1}{\sqrt{2\pi}\tau_e}\cdot e^{-\frac{(t-t')^2}{2\tau_e^2}}\right)\mathrm{d}t\mathrm{d}t' \\
&= \frac{4k_BT}{R_\Omega R_p^2 E_{p,PD}^2}\cdot g(\tau_e, t_w).
\end{aligned} \tag{6.35}$$

Since the integration time t_w should be reasonably higher than the PD impulse response width τ_e, the double integral in eq. (6.35) is written as a function $g(\tau_e, t_w) = \tau_e^3 \cdot \gamma_k$ where γ_k is a constant depending on the integration time $t_w = k \cdot \tau_e$ with $k \gg 1$. For example, this function results in $\gamma_k = 0.72, 2.4, 5.7$ for $k = 3, 4, 5$. As a practical example, a detected pulse energy of $E_{p,PD} = 0.2\,\text{pJ}$ and a temperature of $T = 300\,\text{K}$ for the load resistance $R_\Omega = 50\,\Omega$ can be considered. Using an integration time of $t_w = 4\tau_e$ for a PD with the pulse width $\tau_e = 5\,\text{ps}$ ($B_{PD} = 37.5\,\text{GHz}$) results in a timing jitter of $\sigma_{c,th} = 1.26\,\text{fs}$ and an amplitude uncertainty of $\Delta r_{th} \leq 2.3 \cdot 10^{-4}$ from thermal noise.

6.4 Performance Comparison of Photonic Sampling Techniques

In the previous sections, several noise sources have been identified affecting the performance of both photonic sampling techniques. Now, a comparison will be given considering the achievable performance in every device, mentioned in the block diagram of fig. 6.1, and optimal receiver characteristics for each sampling technique. The assumed system parameters and the calculated noise performances for the rising edge and the electrical center of mass sampling techniques are summarized in tab. 6.1. Again, an MLL with negligible jitter σ_{MLL} is considered since it is the basic motivation for photonic assisted ADCs and the focus of this thesis is on the analysis of other fundamental noise sources in the system. The repetition rate should be $f_{rep} = 10\,\text{GHz}$. An emitted pulse energy of $E_p = 0.1\,\text{pJ}$ is considered with the pulse width $\tau_o = 180\,\text{fs}$ (300 fs FWHM) and the center wavelength $\lambda_c = 1550\,\text{nm}$. Using an MLL with a RIN PSD of $-155\,\text{dB/Hz}$, as it was measured for a $10\,\text{GHz}$ MLL in [79], leads to relative pulse-to-pulse energy fluctuations of $\Delta r_{p2p} = 1.26 \cdot 10^{-3}$ according to eq. (6.21) at the MLL output. This is slightly above the shot noise limit of $\Delta r_{p2p,sh} = \sqrt{h\nu_c / E_p} = 1.13 \cdot 10^{-3}$. An EDFA with the noise figure $F = 4$ amplifies the pulse train by factor $G = 100$. A chirp of $C_0 = 1$ and a fiber with the average GVD coefficient of $\overline{\beta_2} = 20\,\text{ps}^2/\text{km}$ and the length $L = 10\,\text{m}$ leads to a Gordon-Haus jitter of $\sigma_{GH} = 2.07\,\text{fs}$ as discussed in section 6.1. For both sampling techniques, the CDN in fig. 1.1(b) should be used with a typical CDN loss of $\alpha_{CDN} = \alpha_{gr} + 3\alpha_{MMI} + \alpha_{wg} = 14\,\text{dB}$ or $\alpha_{CDN} = 0.04$ including a grating coupler loss of $\alpha_{gr} = 3\,\text{dB}$, a MMI coupler loss of $\alpha_{MMI} = 3\,\text{dB}$ due to the splitting and a waveguide loss of $\alpha_{wg} = 2\,\text{dB}$. The CDNs from fig. 4.9 can be used for time-interleaving of eight samplers which receive optical pulse trains from an external $10\,\text{GHz}$ MLL. Combined with the photodiode quantum efficiency of $\eta_{PD} = 0.5$, the effective CDN efficiency results in $\eta_{eff} = \alpha_{CDN}\eta_{PD} = 0.02$. This leads to a detected pulse energy of $E_{p,PD} = 0.2\,\text{pJ}$. In general, photodiode requirements are different for both sampling techniques, as mentioned in sections 6.2 and 6.3. For the rising edge triggered sampler photodiodes with high bandwidths of $B_{PD,e} = 30\,\text{GHz}$, $50\,\text{GHz}$

MLL	Pulse energy	$E_p = 0.1\,\text{pJ}$
	Gaussian pulse width	$\tau_o = 180\,\text{fs}$ ($\tau_{o,FWHM} = 300\,\text{fs}$)
	Repetition rate	$f_{rep} = 10\,\text{GHz}$
	Center wavelength	$\lambda_c = 1550\,\text{nm}$
	RIN PSD	$S_{RIN}(f) = -155\,\text{dB/Hz}$
	Pulse energy fluctuations	$\Delta r_{p2p} = 0.126\,\%$
EDFA	Gain	$G = 20\,\text{dB}$
	Noise figure	$F = 6\,\text{dB}$
CDN	Grating coupler loss	$\alpha_{gr} = 3\,\text{dB}$
	MMI loss	$3 \cdot \alpha_{MMI} = 3 \cdot 3\,\text{dB}$
	Waveguide loss	$\alpha_{wg} = 2\,\text{dB}$
PD	Quantum efficiency	$\eta_{PD} = 0.5$
	Detected pulse energy	$E_{p,PD} = 0.2\,\text{pJ}$
	Load resistance	$R_\Omega = 50\,\Omega$
	Temperature	$T = 300\,\text{K}$
	Detected pulse energy fluctuations	$\Delta r_{p2p} = 0.27\,\%$

	Rising edge sampling	**Center of mass sampling**
PD bandwidth	$B_{e,PD} = 30\,\text{GHz}/50\,\text{GHz}/70\,\text{GHz}$	$B_{e,PD} = 20\,\text{GHz}/30\,\text{GHz}/40\,\text{GHz}$
Jitter from ASE and shot noise	$\sigma_{e,opt} = 9\,\text{fs}/5.4\,\text{fs}/3.9\,\text{fs}$	$\sigma_{c,opt} = 0.3\,\text{fs}$
Integration window	-	$t_w = 4\tau_e = 37.4\,\text{ps}/24.9\,\text{ps}/18.7\,\text{ps}$
Jitter from thermal noise	$\sigma_{e,th} = 1\,\text{fs}/0.5\,\text{fs}/0.3\,\text{fs}$	$\sigma_{c,th} = 3.2\,\text{fs}/1.8\,\text{fs}/1.1\,\text{fs}$
Jitter from pulse energy fluctuations	$\sigma_{e,p2p} = 9.95\,\text{fs}/5.97\,\text{fs}/4.26\,\text{fs}$	-
ENOB limit from pulse energy fluctuations	-	$< 9\,\text{ENOB}$

Table 6.1: Example for comparison of photonic sampling techniques with assumed individual system parameters and the resulting noise performances for the rising edge and the electrical center of mass sampling.

and 70 GHz should be used. The expected photodiode saturation is beneficial in this case, as discussed in section 6.2. Again, a Gaussian-shaped PD impulse response is considered with the pulse width $\tau_e = \sqrt{\ln 2}/\sqrt{2}\pi B_{PD,e}$ ($\tau_{e,FWHM} = 2\sqrt{\ln 2}\tau_e$). Using eq. (6.16) leads to a jitter of $\sigma_{e,opt} = 9\,\text{fs}$, $5.4\,\text{fs}$ and $3.9\,\text{fs}$ for the mentioned bandwidths $B_{PD,e}$ due to shot and ASE noise. For a load resistance of $R_\Omega = 50\,\Omega$ at the temperature $T = 300\,\text{K}$, the jitter due to thermal noise would be $\sigma_{e,th} = 1\,\text{fs}$, $0.5\,\text{fs}$ and $0.3\,\text{fs}$, according to eq. (6.17). The MLL RIN PSD is decreased by the total noise figure of $F_{dB,tot} = 6.5\,\text{dB}$ by the EDFA and the effective CDN efficiency leading to relative pulse-to-pulse energy fluctuations of $\Delta r_{p2p} = 0.27\,\%$ at the PD. Neglecting any photodiode saturation results in an induced jitter of $\sigma_{e,p2p} = 9.95\,\text{fs}$, $5.97\,\text{fs}$ and $4.26\,\text{fs}$ for the bandwidths $B_{PD,e}$ according to eq. (6.20). The actual jitter induced by pulse-to-pulse energy fluctuations should be smaller due to photodiode saturation. In [39], an opto-electronic clock converter (OECC) was realized where the rising edge of photodetected pulses was used to switch electronic circuit states, and a phase noise of $-161\,\text{dBc/Hz}$ was measured for high offset frequencies of $> 3\,\text{MHz}$. Integration of this value up to the Nyquist frequency of $2.5\,\text{GHz}$ results in a jitter of $20\,\text{fs}$.

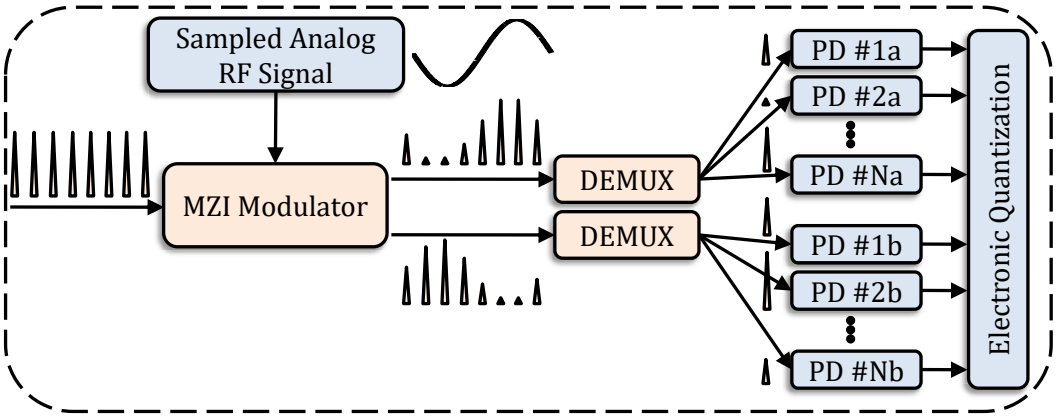

Figure 6.3: The sampled analog RF signal is weighting the optical pulse train by an MZI modulator. Both output arms are used for the electronic quantization process after optical pulses are detected by PDs. Two demultiplexer (DEMUX) distribute the pulses of both MZI modulator outputs to several PDs.

Taking into account that the measured phase noise was limited by the thermal noise within the measurement path and subtracting the amplifier noise figure of $F_{dB} = 6\,\text{dB}$ from the measured phase noise level at the electric spectrum analyzer leads to a jitter of $10\,\text{fs}$. This experimentally shown value suggests that pulse-to-pulse energy fluctuations are less critical. Detailed measurement results of this device will be given in section 7.3. In conclusion, the rising edge sampling technique is dominated by shot and ASE noise and pulse-to-pulse energy fluctuations. Nevertheless, the provided calculations and the work in [39] show that for such systems with reasonable values for individual system components, timing jitter values of $\approx 10\,\text{fs}$ can be achieved. Fast photodiodes with high responsivity as essential components had been shown in [91] and used in [39].

For center of mass samplers, the timing jitter due to shot and ASE noise is $\sigma_{c,opt} = 0.3\,\text{fs}$ for the same system. The electrical PD bandwidths should be $B_{PD,c} = 20\,\text{GHz}$, $30\,\text{GHz}$ and $40\,\text{GHz}$ to avoid high peak currents and photodiode saturation. Using an integration time of $t_w = 4\tau_e$ results in thermal-noise-induced timing jitter of $\sigma_{c,th} = 3.2\,\text{fs}$, $\sigma_{c,th} = 1.8\,\text{fs}$ and $\sigma_{c,th} = 1.1\,\text{fs}$ for the different bandwidths $B_{PD,c}$. Therefore, the center of mass sampling technique shows a better timing jitter performance of roughly one order of magnitude. Unfortunately, the unavoidable pulse-to-pulse energy fluctuations of $\Delta r_{p2p} = 0.27\,\%$ in this example limit the ADC resolution to $< 9\,\text{ENOB}$ since it exceeds the quantization noise of $r_q = 0.002$ of a $9\,\text{bit}$ ADC. Furthermore, weighting the detected pulses by the sampled RF signal decreases the pulse energy even more and hence also the ENOB. For example, if the modulation depth of the weighting process in fig. 6.1 is $90\,\%$ (decreasing the amplitude by $10\,\text{dB}$), the relative pulse-to-pulse energy fluctuations result in $\Delta r_{p2p} = 0.38\,\%$. This is slightly smaller than the quantization noise $r_q = 0.0039$ of an $8\,\text{bit}$ ADC. These dis-

Sampling technique	Photodiode requirements	Timing jitter	Pulse-to-pulse energy fluctuations
Rising edge (electrical)	high quantum efficiency, high bandwidth, saturation beneficial	decreases for higher pulse energy, shorter optical pulses and higher PD bandwidth	transfer to timing jitter
Center of mass (electrical)	high quantum efficiency, high linearity	decreases for higher pulse energy and shorter optical pulses	limit ADC resolution
Center of mass (optical)	high quantum efficiency	decreases for higher pulse energy and shorter optical pulses	limit ADC resolution

Table 6.2: Summarized characteristics of principle photonic sampling techniques

advantages can be avoided by performing the weighting process in the optical domain by means of a modulator. In such a scenario, both outputs of an MZI modulator can be used for the quantization process, as was suggested in [25] and is schematically illustrated in fig. 6.3. The quantization can be performed with the higher pulse energy of the MZI modulator outputs in an electronic post-detection process. In the presented example, the modulation depth of $50\,\%$ results in relative pulse-to-pulse energy fluctuations of $\Delta r_{p2p} = 0.28\,\%$. It is noteworthy that this ADC resolution limitation depends only on the signal amplitude. Thus, pure electronic ADCs provide a better resolution in terms of ENOB for low signal frequencies of $< 1\,\mathrm{GHz}$ [24] compared to photonic ADCs which use the center of mass sampling technique. Their superiority remains for higher sampled signal frequencies where the jitter of electronic clock signals is too high. By sampling in the optical domain, the impact of thermal noise on timing jitter disappears since the jitter is only relevant at the sampling instant. The timing jitter after the sampling process becomes irrelevant. Thus, the photodiode linearity requirement disappears. Thermal noise impact on the quantization process remains, but is less critical than pulse-to-pulse energy fluctuations. For the previous example, the relative uncertainty of the current integration is $\Delta r_{th} < 3.2 \cdot 10^{-4}$ according to eq. (6.33). The discussed characteristics of the sampling techniques are summarized in table 6.2.

6.5 Measurability

In this section, the experimental verification of the derived formulas for the rising edge and the center of mass sampling techniques from sections 6.2 and 6.3 are discussed.
In general, it is a challenging task to measure jitter values in the range of few femtoseconds and to verify their origin. Experimental investigation of a certain jitter characteristic regarding one noise source requires the cancellation or mitigation of other interfering effects affecting the jitter. As discussed in section 3.5, frequency domain measurements are well

suited for this. By means of phase noise measurements at an arbitrary harmonic, different noise sources can be separated regarding their characteristic impact on the offset frequency fluctuations. It enables the possibility to measure shot noise limited jitter of few femtoseconds with a passive MLL having a much higher low frequency jitter. The laser only needs to have a sufficiently low jitter contribution from high offset frequency fluctuations which is usually the case.

An ESA, performing the phase noise measurement, requires a certain input power level for the harmonic to achieve a high measurement sensitivity. But too high pulse energies saturate the photodiode and affect the phase noise curves by means of amplitude-to-phase noise conversion [76, 77, 151] where pulse-to-pulse energy fluctuations couple to the jitter of the induced electrical pulse train. A method to avoid photodiode saturation and to achieve a high power level for the harmonic at the same time is to use higher repetition rate pulse trains [150, 151]. Moreover, it is convenient to use higher order harmonics since the phase noise is proportional to the square of the harmonic order, which has been shown in eq. (3.35).

The most important formulas derived from the quantum noise model in the upper sections are (6.16) and (6.30) describing the jitter performance of photonic samplers using the rising edge or the center of mass sampling technique. Experimental verification of these confirms the whole noise model.

First of all, eq. (6.16) gives the jitter at one reference point of the rising edge of the induced photocurrent pulses. A possible jitter measurement of this exact reference point has to be performed in the time domain. But time domain measurements by electronics are not able to measure jitter in the desired femtosecond regime. Oscilloscopes have unavoidable intrinsic jitter and a measurement of jitter values of < 1 ps is barely possible. Only after realization of a complete rising edge sampler, the jitter at the sampling instant can be derived from the effective resolution of the sampled high-frequency signals. Frequency domain measurements always refer to the center of mass jitter and, therefore, are not applicable for verification of the rising edge jitter. But since the relations in eqs. (6.16) and (6.30) are derived from the same noise model and using the same noise currents from eq. (6.7), induced during the photodetection process, verification of the formula for the center of mass jitter suggests correctness of the formula for the rising edge jitter. Therefore, the focus here is on the verification of eq. (6.30).

In section 3.5, it has already been shown that pulse-to-pulse energy fluctuations as well as the timing jitter of optical pulse trains can be measured through the sideband noise of arbitrary harmonics of the detected electrical spectrum. In section 6.1, a quantum noise model has been presented able to describe the photocurrent noise induced by shot, ASE

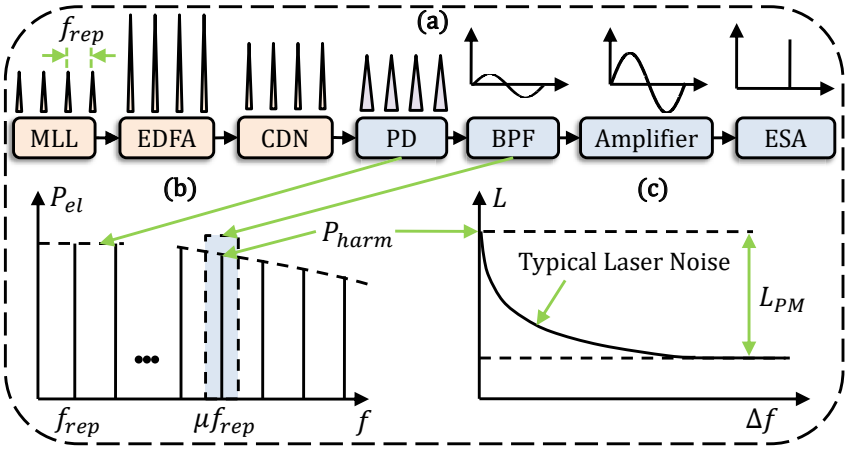

Figure 6.4: **(a)** Typical center of mass jitter measurement set-up using a BPF and an electrical amplifier to perform a phase noise measurement by an ESA at the μ-th harmonic of the electrical spectrum. The optical pulse train is emitted by an MLL with the repetition rate f_{rep}, amplified by an EDFA, coupled to a CDN and detected by a PD. **(b)** Spectrum after PD with the filtered harmonic and the envelope resulting from limited PD bandwidth. **(c)** SSB phase noise of a demodulated harmonic with typical phase noise of real MLL for low offset frequencies and the quantum noise limit L_{PM} for high offset frequencies relative to the harmonic power P_{harm}.

and thermal noise. Its impact on the rising edge and the center of mass jitter was discussed in sections 6.2 and 6.3. In this section, the SSB noise at an arbitrary harmonic is derived based on the introduced quantum noise model and the derived photocurrent noise to verify its validity through phase noise measurements.

The principle measurement set-up is illustrated in fig. 6.4. The pulse train with the repetition rate f_{rep} is emitted by an MLL, amplified by an EDFA, coupled to the CDN and detected by a PD. The photocurrent PSD can be measured by an ESA and is derived in appendix B to

$$S_i(f) = R_p^2 G^2 \eta_{eff}^2 \left|P_{opt}(f)\right|^2 \left|G_{PD}(f)\right|^2 + qI_{avg}(1+\eta_{eff}(FG-1))\left|G_{PD}(f)\right|^2 \quad (6.36)$$

where $G_{PD}(f)$ is the photodiode transfer function. Furthermore, the PSD of the pulse train optical power envelope

$$\left|P_{opt}(f)\right|^2 = \lim_{T\to\infty} \frac{1}{T}\left(\left|P_{opt,T}(f)\right|^2\right) = \lim_{T\to\infty} \frac{1}{T}\left(\left|\mathcal{F}_T\left\{|A(t)|^2 * \delta_{T_{rep}}(t)\right\}\right|^2\right) \quad (6.37)$$

and the average photocurrent

$$I_{avg} = R_p G \eta_{eff} P_{avg} = R_p G \eta_{eff} E_p f_{rep} \quad (6.38)$$

have been used. The average optical power in eq. (6.38) can be related to eq. (6.37) by $P_{avg} = P_{opt}(0)$. $\delta_{T_{rep}}(t)$ in eq. (6.37) is a Dirac comb with the pulse train repetition

period $T_{rep} = 1/f_{rep}$. The first term in eq. (6.36) represents the deterministic photocurrent PSD consisting of the optically induced current PSD $R_p^2 G^2 \eta_{eff}^2 |P_{opt}(f)|^2$ scaled by the amplitude spectrum of the PD transfer function $|G_{PD}(f)|^2$. The second term represents the photocurrent noise PSD which is identical to the case of photodetection of CW light which has also been found in [69]. Thus, the mathematical approach in appendix B leads to the well-known result for the amplitude photocurrent PSD $S_i(f)$.

In the following, the focus is on the PSD from amplitude and phase noise measurements where the phases of the detected components are relevant in contrast to the spectrum in eq. (6.36). A bandpass filter (BPF) filters out a harmonic of the μ-th order where the phase noise measurement is performed after demodulation to the baseband. This is indicated in the measurement set-up in fig. 6.4. An electrical amplifier in front of the ESA is usually necessary to achieve a high phase noise sensitivity. For sufficiently high photocurrents ($\gg$ 1 mA), shot noise dominates compared to thermal noise of a load resistance, and its noise floor is detectable for high offset frequency fluctuations. In appendix C, this SSB amplitude and phase noise level in Hz^{-1} is derived to

$$L_{AM/PM}(f) = \frac{1}{2} \frac{q I_{avg} |\tilde{G}(\mu f_{rep})|^2 R_\Omega}{P_{harm}(\mu f_{rep})} \cdot (1 + \eta_{eff}(FG - 1)) \cdot \left[1 \pm \frac{|P_{opt}(2\mu f_{rep})|}{|P_{opt}(0)|} \cos(\phi_p(2\mu f_{rep}) - 2\phi_p(\mu f_{rep}))\right] \quad (6.39)$$

where the plus sign within the rectangular brackets is valid for amplitude noise measurements, while the minus sign represents phase noise measurements. It stems from the relative phase of the local oscillator which demodulates the noise components to the baseband. This phase difference leads to the different sign of the cosine function. $\tilde{G}(\mu f_{rep})$ is the concatenated transfer function of the photodiode and the BPF at the μ-th harmonic μf_{rep} and R_Ω is the terminating resistor of the ESA. $|P_{opt}(f)|$ and $\phi_p(f)$ are the amplitude and the phase of the optical power envelope transfer function $P_{opt}(f)$. The SSB amplitude or phase noise is always measured relative to the microwave power of the measured harmonic which can be expressed as

$$P_{harm}(\mu f_{rep}) = I_{avg}^2 |\tilde{G}(\mu f_{rep})|^2 R_\Omega. \quad (6.40)$$

From the result in eq. (6.39), it can be concluded that the phase noise shrinks for shorter optical pulses corresponding to $|P_{opt}(2\mu f_{rep})| \rightarrow |P_{opt}(0)|$. In this case, the expression within the brackets goes to zero. In contrast, the amplitude noise increases due to the plus sign. It leads to the interpretation that the shot noise is shifting from the phase to the amplitude for shorter optical pulses. This result corresponds to the calculations in [69, 168] if the CDN and the EDFA are neglected. This proves consistency of the used noise model compared to recent publications. The resulting squared timing jitter can be calculated from

the SSB phase noise level by [19]

$$\sigma^2 = \frac{1}{(2\pi\mu f_{rep})^2} \int_0^{\frac{f_{rep}}{2}} 2L_{PM}(f)\mathrm{d}f. \tag{6.41}$$

Now, an example is provided to point out the derived relations. An optical pulse train with a Gaussian pulse power envelope from eq. (4.15) is considered. The phase function $\phi_p(f)$ of such a Gaussian pulse train is zero and the cosine function in eq. (6.39) equals 1. The Fourier transform of a Gaussian pulse is again a Gaussian pulse and, therefore,

$$\frac{|P_{opt}(2\mu f_{rep})|}{|P_{opt}(0)|} = e^{-(2\pi\mu f_{rep}\tau_o)^2}. \tag{6.42}$$

For the Gaussian pulse, the SSB phase noise in eq. (6.39) results in

$$\begin{aligned} L_{PM,Gauss}(f) &= \frac{q}{2I_{avg}} \cdot (1 + \eta_{eff}(FG-1)) \cdot \left[1 - e^{-(2\pi\mu f_{rep}\tau_o)^2}\right] \\ &\approx \frac{q}{2I_{avg}} \cdot (1 + \eta_{eff}(FG-1)) \cdot (2\pi\mu f_{rep}\tau_o)^2 \end{aligned} \tag{6.43}$$

where the ultra-short optical pulse approach $2\pi\mu f_{rep}\tau_o \ll 1$ has been used reducing the expression within the brackets to a second order Taylor approximation. The derived SSB phase noise in eq. (6.43) is proportional to the squared harmonic order μ as expected from the results in eq. (3.35). The relation $R_p = q/h\nu_c$ for the ideal photodiode impulse response and eq. (6.38) can be applied to eq. (6.43). In that way the timing jitter in eq. (6.41) with the SSB phase noise of a Gaussian pulse power envelope in eq. (6.43) corresponds exactly to the formula of the center of mass jitter from eq. (6.30) derived by a different approach. It proves the correctness of the calculated SSB phase noise as well as the fact that this phase noise refers to the center of mass jitter. This is a much more intuitive interpretation than the explanation given in [69] based on shot noise correlations during the photodetection process.

The SSB amplitude noise can be derived similarly for the ultra-short Gaussian pulse approach to

$$L_{AM,Gauss}(f) \approx \frac{q}{I_{avg}} \cdot (1 + \eta_{eff}(FG-1)). \tag{6.44}$$

As expected, it is independent of the harmonic order μ, as has already been shown in eq. (3.35). Regarding the simplified expressions in eqs. (6.43) and (6.44), it can be seen that the noise is shifting from the phase to the amplitude for the ultra-short pulse approach. The sum is still the same and refers to the noise term in the amplitude spectrum of eq. (6.36).

Now, the derived relations should be demonstrated in an example. Once again, the standard example from the end of section 6.4 is used with the effective CDN efficiency $\eta_{eff} = 0.02$, the center wavelength $\lambda_c = 1550\,\mathrm{nm}$ and the detected pulse energy $E_{p,PD} = 0.2\,\mathrm{pJ}$ which

is achieved by an EDFA with the amplification $G = 100$ and the noise figure $F = 4$. Using a repetition rate of $f_{rep} = 10\,\mathrm{GHz}$, the average photocurrent results in $I_{avg} = 2.5\,\mathrm{mA}$, according to eq. (6.38). Finally, the optical pulse width $\tau_o = 180\,\mathrm{fs}$ is used and deteriorating effects of the photodiode and the BPF, such as saturation or loss, should be neglected. In this case, the SSB phase noise level in eq. (6.43) results in $L_{PM}(f) \approx -194.3\,\mathrm{dBc/Hz}$, $-188.3\,\mathrm{dBc/Hz}$, $-184.8\,\mathrm{dBc/Hz}$, $-182.3\,\mathrm{dBc/Hz}$ for the harmonic orders $\mu = 1, 2, 3, 4$ corresponding to a timing jitter of $\sigma = 0.3\,\mathrm{fs}$ using eq. (6.41). It corresponds exactly to the calculated center of mass jitter from section 6.4 for the same example.

Recent experiments in [69, 168] confirmed that the SSB phase noise decreases for shorter optical pulses as predicted by eq. (6.39). A limiting factor in such phase noise measurements can result from saturation effects in the photodiode. In the experiments in [69], the SSB phase noise level of $-179\,\mathrm{dBc/Hz}$ at the fifth harmonic of the $2\,\mathrm{GHz}$ repetition rate did not decrease further for pulse widths $< 3\,\mathrm{ps}$. Such a phase noise level corresponds to $0.8\,\mathrm{fs}$ jitter if Gaussian pulses are assumed. This effect was explained in [133] by means of the random carrier drift time within the intrinsic photodiode region indicating that the photodiode impulse response is not completely deterministic. The random drift time within the intrinsic region creates also a certain amount of jitter although its value seems to be very low according to the mentioned experiment. This has been discussed in section 4.5.

Chapter 7

Experiments

In this chapter, the experimental results are shown and discussed. Skew measurements of optical CDNs are provided in section 7.1. Non-linear pulse propagation experiments are discussed in section 7.2. Finally, an opto-electronic clock converter (OECC) is introduced in section 7.3 whose jitter performance proves the superiority of optical clock distribution. This OECC can be used to clock time-interleaved ADCs. Its timing precision refers to the rising edge jitter of the induced photocurrent pulses. All devices were fabricated with the silicon photonics BiCMOS platform from [96] in the framework of the MOSAIC project (13N12435) of the German Ministry of Education and Research. The presented results were partly published in [39, 80].

7.1 Skew

A certain amount of skew is unavoidable in optical CDNs due to fabrication tolerances and temperature dependency which has been discussed in section 4.6. To characterize the skew of the time-interleaved optical CDNs from fig. 4.9, a test structure had been fabricated. Here, a CDN with different waveguide lengths and without photodiodes had been realized. The results were published in [80] and are discussed here in more detail. The measurement set-up and the schematic of the device under test (DUT) is shown in fig. 7.1, while a camera picture of the actual test structure is shown in fig. 7.3(a). The test structure consisted of a 1D input grating which coupled a pulse train out of a fiber into a silicon rib waveguide with the dimensions from fig. 4.3. 1x2 MMI couplers and different waveguide lengths were used to split the pulse train into four which were combined again with certain delays. The CDN corresponded to the upper half of the CDN from fig. 4.9(a) which was connected to its mirrored version. The resulting signal was coupled back into a fiber by a 1D output grating. As a consequence, four pulses were coupled out of the CDN for every input pulse. Afterwards,

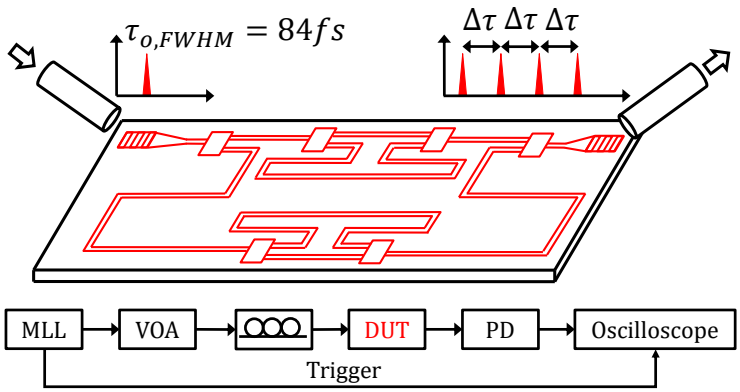

Figure 7.1: Block diagram of the measurement set-up for skew characterization of optical CDNs: A pulse train from a low repetition rate MLL is damped by a variable optical attenuator (VOA). The polarization is adjusted for optimum input coupling to the 1D grating coupler of the device under test (DUT). The output signal is coupled into a fiber, detected by a fast photodiode (PD) and measured by an oscilloscope. The schematic of the DUT is shown above the block diagram. It consists of a CDN which splits an incoming pulse into four combining them with certain delays.

these pulses were detected by a photodiode and measured by an oscilloscope. It was triggered by the electrical reference output of the MLL which provided the optical pulse train with a low repetition rate of 100 MHz. The repetition period had to be much larger than the maximum delay in the DUT, so that the four time-interleaved pulses did not overlap with the following ones after detection at the oscilloscope. This condition was fulfilled since the designed delays had been $\tau_k = k \cdot 25\,\text{ps} \ll 10\,\text{ns}$ for $k = 1, 2, 3$. The MLL pulse width was $\tau_{o,FWHM} = 84\,\text{fs}$, according to the data sheet. The pulse train polarization was adjusted by a 3-paddle polarization controller to maximize the coupling efficiency of the 1D input grating. Moreover, a variable optical attenuator (VOA) was used to set the optical average input power to $P_{opt} = 0\,\text{dBm}$, so that non-linearities could be neglected. A 50 GHz photodiode detected the output signal. Finally, a following 70 GHz oscilloscope was used to measure these four time-interleaved pulses while being triggered by the MLL. The deviations from the designed delays between the leading and the following pulses correspond to the skews. A typical measurement result is shown in fig. 7.2. In fig. 7.2(a), the four detected pulses are shown. The amplitude decrease from the 1st to the 2nd and from the 3rd to the 4th detected pulse results from non-ideal splitting ratios of the 1x2 MMIs and additional attenuation due to the longer waveguide length. During the measurements, it was observed that by slight displacement of the fiber above the input grating coupler, the amplitudes of the 1st and 2nd pulse changed relative to the 3rd and 4th pulse. It indicates that only the splitting ratio of the 1st MMI was sensitive towards the exact fiber position at the input grating.

The delays of the 2nd, 3rd and 4th pulse were measured relative to the 1st pulse. The skews corresponded to deviations of these delays from the designed values. A zoom to the second

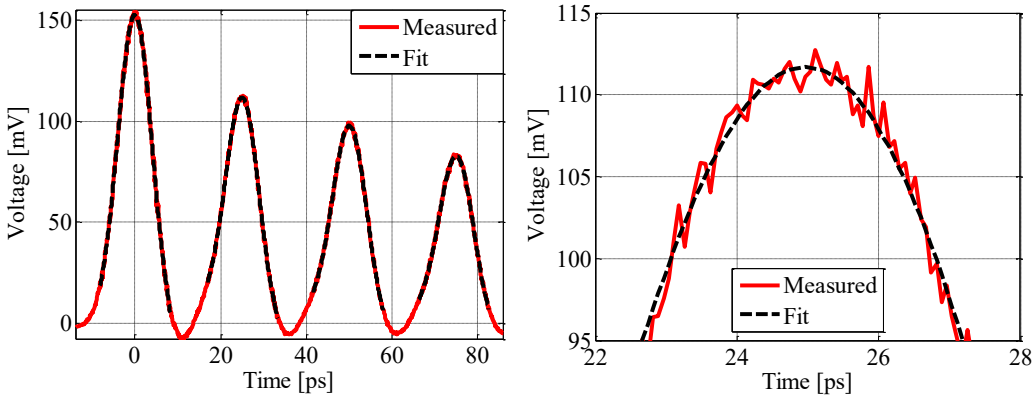

Figure 7.2: Typical measurement result of four time-interleaved optical pulses detected by a PD and measured by an equivalent-time oscilloscope: (a) Single measurement of the four detected pulses (b) Zoom to 2nd pulse peak including the 7th order polynomial fit.

pulse peak in fig. 7.2(b) shows the noise impact on the measurement. Because of that, an exact identification of the pulse peak position is not possible. To deal with noise, the following fitting procedure was applied. At first, 1024 measurements were recorded by the oscilloscope and the averaged pulse form was saved. Afterwards, a 7th order polynomial fit was used for each pulse to get an exact instant of time for the pulse peak position. A fitting procedure is necessary for skew measurements in the femtosecond range. After the identification of the pulse peak position in time, the skew was calculated. Furthermore, this measurement was done for different chip temperatures to investigate the temperature drift. Five measurements were performed for each temperature to reduce the noise impact further. A typical result is shown in fig. 7.3(b). The standard deviation for the calculated skew values was $\approx 20\,\text{fs}$. In fact, it is sufficient for this measurement set-up since the distance in time between two measurement points of the oscilloscope had been $74\,\text{fs}$. Fig. 7.3(b) shows that the skew was $< 100\,\text{fs}$ for the specified chip temperature of $80\,^{\circ}\text{C}$ for the investigated test structure. A linear fit to the temperature drifts leads to values of $\approx 6\,\text{fs/K}$, $\approx 3\,\text{fs/K}$ and $\approx 0\,\text{fs/K}$ for delay lines of $75\,\text{ps}$, $50\,\text{ps}$ and $25\,\text{ps}$. To the authors knowledge, it is the first measurement of such low skew values for optical CDNs. Considering the thermo-optic coefficient of silicon as the single temperature-sensitive source affecting the effective refractive index would result in temperature drifts of $4.56\,\text{fs/K}$, $3.04\,\text{fs/K}$ and $1.52\,\text{fs/K}$, according to eq. (4.18) for the mentioned delays and an ideal waveguide fabrication process. Obviously, there are deviations between the theoretical and the experimental values. Similar deviations were noticed for identical test structures from different dies. Their values are summarized in table 7.1. Here, the shown measurement results in figs. 7.2 and 7.3

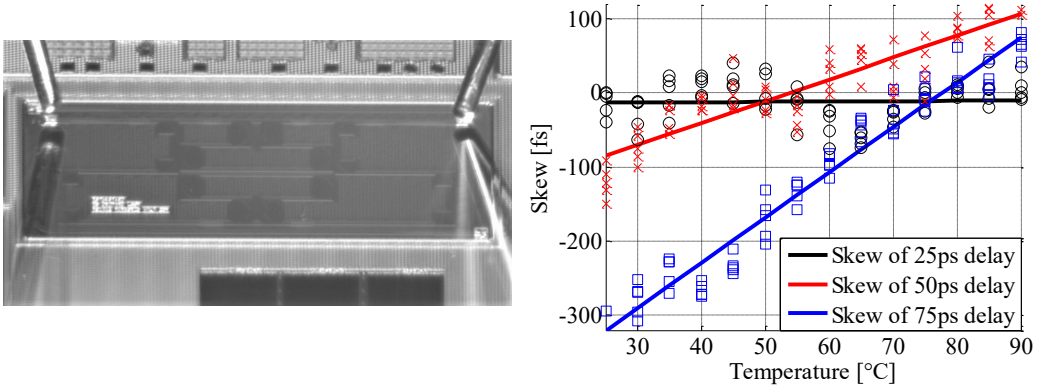

(a) (b)

Figure 7.3: (a) Camera picture of the DUT used for skew measurement with fibers placed above the input and output gratings. (b) Typical measurement results of the temperature-dependent skews as deviations from the designed delays of 25 ps, 50 ps and 75 ps of the following pulses relative to the leading pulse.

correspond to device #1. Fabrication tolerances do not have such a strong impact on the temperature drift. Furthermore, oscillations of the measured skew during the temperature rise in fig. 7.3(b) indicate another thermo-optic influence. A possible reason for the deviations could be stress at the waveguide interfaces. The silicon dioxide cladding induces an effective refractive index change by the stress-induced photo-elastic effect [169, 170].

Balanced optical clock trees for electronic circuit synchronization, as introduced in fig. 1.1(b), have identical delays and would of course have a much lower skew and temperature drift.

Skew compensation in time-interleaved ADCs have been discussed by various authors and will not be addressed here. An overview can be found in [48]. In general, its detection and correction can be performed in the analog or digital domain. Furthermore, the calibration can run in the foreground or background. But since the clock is distributed optically, it is more appropriate to compensate the skew in the digital domain since electronic delay control cannot be applied there.

7.2 Non-linearities

In this section, the non-linear pulse propagation in silicon waveguides is investigated. The non-linearities were discussed in section 4.2.1 as the limiting factor for the CDN performance. Simulations were provided in section 4.6. The additional attenuation from TPA and FCA limits the output pulse energy at every CDN branch.

Basic pulse propagation experiments were performed to study this non-linear behavior and

Device	$\Delta\tau_1$	$\Delta\tau_2$	$\Delta\tau_3$	$d\tau_1$	$d\tau_2$	$d\tau_3$
#1	-11 fs	77 fs	14 fs	0 fs/K	3 fs/K	6 fs/K
#2	127 fs	133 fs	-47 fs	1.6 fs/K	3 fs/K	5.1 fs/K
#3	87 fs	-49 fs	-100 fs	1.9 fs/K	2.3 fs/K	5.5 fs/K
#4	179 fs	20 fs	-3 fs	1.5 fs/K	2.6 fs/K	4.4 fs/K
#5	71 fs	100 fs	92 fs	1.1 fs/K	3.3 fs/K	5.1 fs/K
#6	13 fs	159 fs	-49 fs	0.6 fs/K	4 fs/K	4.9 fs/K
#7	44 fs	51 fs	-6 fs	1.6 fs/K	2.5 fs/K	5.6 fs/K

Table 7.1: Measured skews and their temperature drifts for identical test structures from different dies. The corresponding optical CDN is schematically shown fig. 7.1.

to verify the widely used non-linear pulse propagation model from [90]. A straight 2.1 mm-long rib waveguide with dimensions from fig. 4.3 was used as the test structure. A 1D grating and a subsequent adiabatic taper at the input and output of the waveguide served for coupling of the pulse train into and out of the silicon waveguide. A camera picture of the DUT is shown in the inset of fig. 7.4 where the measurement set-up is provided in a block diagram. The chip temperature was kept constant at 25 °C during the measurement.

A 1.25 GHz MLL was emitting ultra-short pulses whose repetition rate could be optionally increased to 10 GHz by means of a 1x8 optical interleaver. Moreover, an optical BPF could be used optionally for pulse broadening. The bandwidth of the used BPF was 1 nm around the center wavelength of 1550 nm. The resulting pulse train was amplified by an EDFA. The pulse width after the EDFA was either $\tau_{o,FWHM} = 0.3$ ps or $\tau_{o,FWHM} = 3.5$ ps if the BPF had been used. These values resulted from the measured 3 dB optical bandwidth and an assumed Gaussian time-bandwidth product. The VOA in front of the EDFA was necessary so that the specified maximum input power for the EDFA was not exceeded, while the VOA at the amplifier output was used for finetuning of the input power at the DUT. The input power was monitored by means of a 90:10 coupler in front of the DUT. The -10 dB output port was connected to an optical power meter (OPM), while the 0 dB output port provided the input signal. Before coupling the pulse train into the test structure, the optimum polarization was adjusted by means of a 3-paddle polarization controller. The DUT output was coupled back into a fiber and measured by an OPM. The used angle of incidence for the fibers was 12 degrees where the coupling efficiency was maximum. An alternative pulse repetition rate was provided by a 100 MHz MLL with a pulse width of $\tau_{o,FWHM} = 84$ fs, according to the data sheet. The filter function of the input grating broadened these pulses to $\tau_{o,FWHM} \approx 0.1$ ps. These value resulted from the measured 3 dB optical bandwidth at the DUT output and an assumed Gaussian time-bandwidth product. Using the 100 MHz laser at the EDFA input port was not considered since the high pulse intensities exceeded the specified maximum input power. During the measurements, several pulse train characteris-

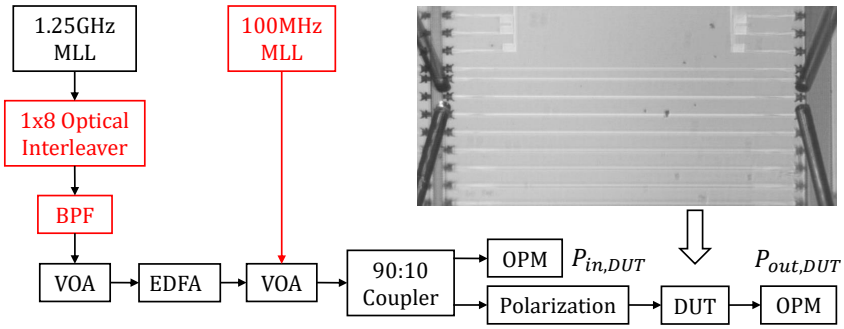

Figure 7.4: Measurement set-up for non-linear pulse propagation experiments. A camera picture of the test structure is shown in the inset.

tics were changed depending on the used MLL, the optional BPF and the optional optical interleaver. The measured average output power of the DUT $P_{out,DUT}$ in dependence on the average input power $P_{in,DUT}$ for these several cases is shown in fig. 7.5(a). The overall DUT loss for a low input power was $8.85\,\mathrm{dB}$. Therefore, the input gratings had a coupling loss of $\approx 4.4\,\mathrm{dB}$. An additional $0.5\,\mathrm{dB}$ was lost at each fiber facet placed above the grating couplers. This value was known from the previously measured fiber-to-fiber transition experiment. Linear propagation loss can be neglected for such a short waveguide.

The pulse trains with lower repetition rates were attenuated much stronger for the same input power since the pulse energies were much higher. A surprising result was that the broader pulses had been attenuated stronger than the ultra-short pulses for the repetition rates of $1.25\,\mathrm{GHz}$ and $10\,\mathrm{GHz}$, as can be seen in fig. 7.5(a) for high input powers. Interestingly, the DUT output power was decreasing after reaching the saturation level for the ultra-short $100\,\mathrm{MHz}$ pulse train exactly like reported in [121]. This could not be observed for higher repetition rate pulse trains because the output power could not be increased into deep saturation without destroying the test structure. This behavior cannot be explained by the widely used model from [90]. As mentioned in [121], this model is derived for small non-linear perturbations which is not fulfilled anymore in deep saturation. The higher attenuation of broader pulses is also not conform with this model. Fig. 7.5(b) shows simulation results for the same experiment. The simulation parameters were taken from tab. 4.1. The unknown effective carrier lifetime was chosen as $\tau_{eff} = 10\,\mathrm{ns}$ to fit the simulation results to the experiment for the broad pulse cases. Using the same parameters for the ultra-short pulses leads to the higher loss of $\approx 5\,\mathrm{dB}$ in the simulations. But the experimental results did not show less output power. In fact, for ultra-short pulse trains, the attenuation even decreased as mentioned before. This is another hint that the model from [90] is less applicable for ultra-short pulses. Furthermore, the assumption of an exponential decay of the effective carrier lifetime may be too simple [118] and its actual impact should be reconsidered. The

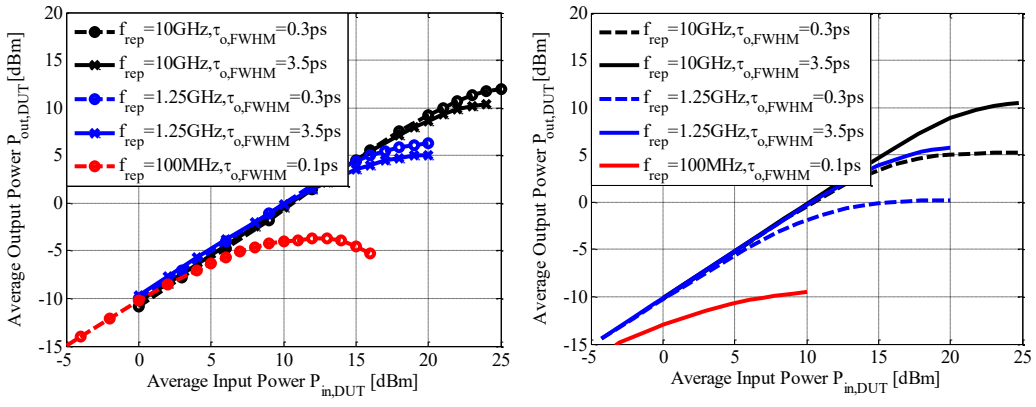

Figure 7.5: (a) Measured average DUT output power in dependence on the average DUT input power for various pulse train characteristics. (b) Simulation results for the used pulse train characteristics in the experiments with parameters from tab. 4.1. The effective carrier lifetime was chosen as $\tau_{eff} = 10\,\text{ns}$ to fit the curves of the broad pulse cases to the experimental results.

surprising observation of less attenuation for shorter pulses is very beneficial since it also decreases the jitter after detection according to eq. (6.30).

7.3 Opto-Electronic Clock Converter

In this section, a fully integrated opto-electronic clock converter (OECC) circuit is introduced. The optical CDN had been designed by the author, while the electronics had been designed by *Rohde&Schwarz* under the frame of the MOSAIC project (13N12435) of the German Federal Ministry of Education and Research. The chip was fabricated by the photonic $0.25\,\mu$m BiCMOS platform [96] at the *Institute of Innovations for High Performance Microelectronics (IHP)*. It enables monolithic integration of photonic components and high performance BiCMOS technology. Measurement results of the realized OECC were partly published in [39]. In this section, the OECC is characterized and the goal is to verify the theoretical calculations provided in chapter 6. A camera picture of the chip is shown in fig. 7.6(a), while the optical layers of the CDN are shown in fig. 7.6(b).

An optical pulse train with a repetition rate of 10 GHz was provided as the input to the DUT. It was coupled out of a fiber into a silicon waveguide by a 1D grating coupler. This corresponds to the left fiber in the camera picture of fig. 7.6(a). This pulse train was split by 1x2 MMI couplers into eight versions and distributed across the chip. At one CDN branch, a 1D grating coupler was placed to measure the optical output signal of the CDN. Once again, the light was coupled into a fiber. It corresponds to the right fiber in fig. 7.6(a). This optical output served for CDN characterization and optimum fiber positioning. At the other CDN

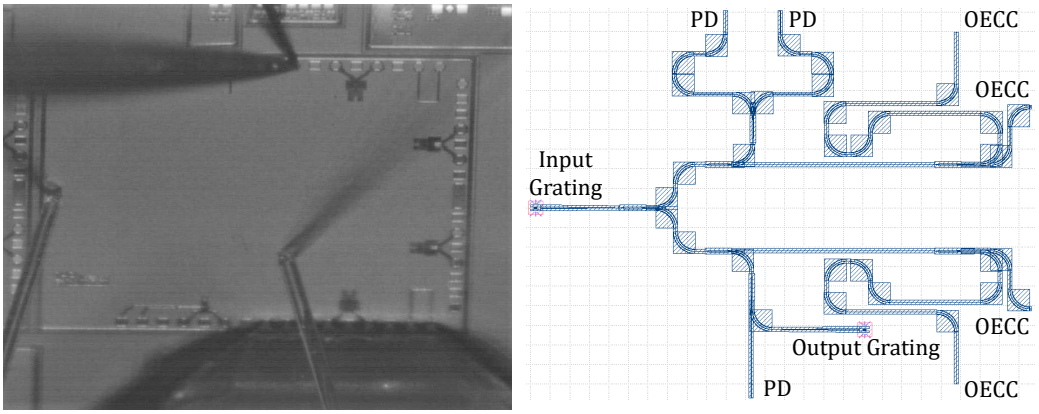

(a) (b)

Figure 7.6: (a) Camera picture of an OECC chip with input and output fibers placed above the grating couplers on the left and right. A probe head is placed at the electrical contacts, while internal voltage of the IC is measured by the contact at the upper part of the photo. (b) Layout of optical CDN with an input grating on the left and eight outputs distributed across the chip. An optical output is used for CDN characterization, while either an OECC or a photodiode is placed at the other outputs.

branches, either photodiodes or OECC circuits were placed as indicated in fig. 7.6(b). A probe head was placed at the contact pads for measurement of the electrical output which can be seen in the lower right part of the camera picture in fig. 7.6(a). Finally, the contact quality was checked by the needle in the upper part of the camera picture where the internal voltage of the IC was measured. Since the electronic circuit had been designed by *Rohde&Schwarz*, its detailed description can be found in [171]. Here, only a short principle of operation will be given and the focus is set to the performance characterization and comparison to the analytical calculations in chapter 6 which were both done by the author. In fig. 7.7 a schematic of the implemented core circuit is shown. The integrated germanium photodiode is placed as the tail current source of a differential pair of transistors. The reverse bias of the operating point was $3\,\mathrm{V}$. Depending on the state of the applied data input D and its inverted state D', respectively, an induced photocurrent is directed through one of the electrical paths. Hence, the nodes above the transistors change their voltage states to either set (S=1, R=0) or reset (R=1, S=0) the output state of the connected RS-flip-flop. The voltage difference between both nodes was $\approx 250\,\mathrm{mV}$, while the supply voltage of the circuit was $4.5\,\mathrm{V}$. Its inverted and non-inverted output states Q and Q' of the RS-flip-flop are directed to an inverter circuit whose outputs Q" and Q"' correspond to the data input for the optically clocked switching circuit for the next incoming pulse. The inverter serves as a delay element to ensure the applied data input at the switch circuit remains constant over the entire photocurrent pulse width. Hence, for every incoming optical pulse, the RS-flip-flop changes its output state leading to an electrical square wave signal with the halved repetition

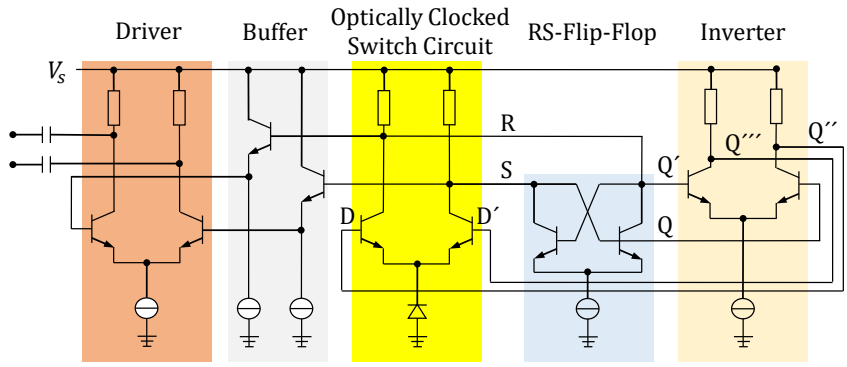

Figure 7.7: Simplified schematic of the implemented OECC circuit with core elements highlighted by different colors.

rate of the incoming pulse train. Finally, the RS-flip-flop output is directed to a buffer and a driver circuit. The direct current components of both driver outputs are blocked. In the actual differential state, these signals are measured against each other. However, in the realized device, both driver outputs were measured separately against a constant voltage. This case is called single-ended. The OECC was implemented by silicon-germanium bipolar transistors in a current-mode logic leading to a differential signal transmission. The flip-flop is triggered by the rising edge of the detected pulses and switches between two voltage states. Therefore, it corresponds to the rising edge clocking case described in section 6.2.
A block diagram of the measurement set-up used for device characterization is shown in fig. 7.8. A fundamentally locked solid-state $1.25\,\mathrm{GHz}$ MLL served as the optical source with a pulse width of $\tau_{o,FWHM} = 200\,\mathrm{fs}$ according to the data sheet. The repetition rate was increased to $10\,\mathrm{GHz}$ by a subsequent 1x8 optical interleaver. Afterwards, a VOA reduced the average optical power to $-3\,\mathrm{dBm}$ for protection of the subsequent EDFA. The optical amplifier was necessary since the MLL did not provide enough power. The pulse width after the EDFA increased to $\tau_{o,FWHM} = 300\,\mathrm{fs}$. Once again, these values resulted from the measured $3\,\mathrm{dB}$ optical bandwidth and an assumed Gaussian time-bandwidth product. A second VOA was used for finetuning of the input power which was monitored during the whole measurements by means of a 90:10 coupler in front of the DUT. The $-10\,\mathrm{dB}$ coupler port was measured by an OPM, while the $0\,\mathrm{dB}$ coupler port provided the signal input for the DUT. The optimum polarization for the 1D input grating coupler was set by a 3-paddle polarization controller. The optical output port of the DUT was used for optimum fiber placement and optimum polarization adjustment at the DUT input by maximizing the detected power at the CDN output. Both fibers were placed under the optimum angle of incidence of 12 degrees. A probe head was placed at the contact pads of the OECC. By means of the probe head DC connectors, the power supply was applied. The specified supply volt-

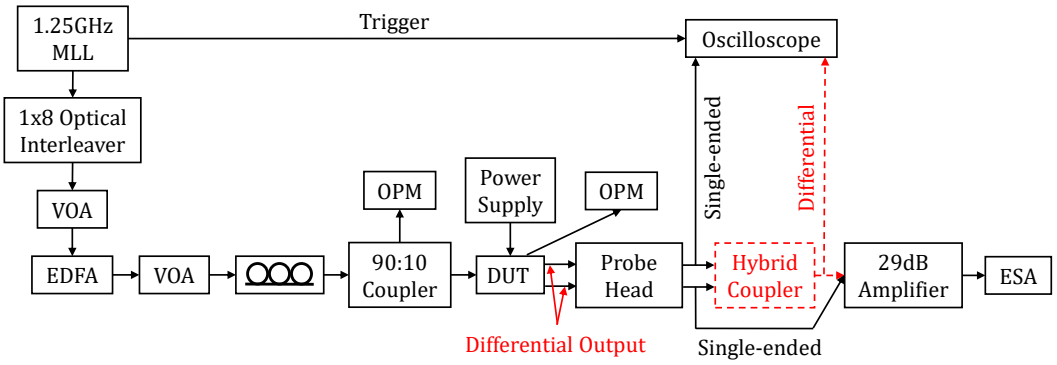

Figure 7.8: Block diagram of the measurement set-up

age of the OECC circuit was 4.5 V and the externally applied voltage had to be adjusted in regard of the voltage drop across the ohmic contacts. The actual internal voltage was measured by means of a needle placed at the corresponding contact pad of a second OECC circuit which can be seen in the camera picture in fig. 7.6(a). The power supply node of all four OECC circuits on chip was connected. Two differential OECC output signals were measured by a 67 GHz probe head. The differential signal results from the used current-mode logic [171]. The idea of using a differential signal is to suppress noise components which affect both outputs in the same way. The noise impact is strongly minimized by the difference operation. But the single-ended outputs could also be measured simultaneously. In this case, one output was measured by a 70 GHz oscilloscope which was triggered by the MLL. At the same time, a frequency measurement could be performed at the other output. Here, the signal was amplified by a 29 dB electronic amplifier. Its noise figure was 6 dB, while the maximum output power was 20 dBm, according to the data sheet. The bandwidth of the used *SHF 810 Broadband Amplifier* was 30 kHz-38 GHz. The amplifier was necessary since the measurement sensitivity of the subsequent ESA depended strongly on the signal power level. The ESA was used for spectrum and phase noise measurements. The combination of both outputs was achieved by means of a hybrid coupler. Unfortunately, its limited bandwidth broadened and distorted the combined signal. But this filter characteristic did not affect the phase noise measurement performed at the fundamental harmonic of 5 GHz of the electric square wave signal.

Before addressing the OECC performance, the photodiode output is discussed at first. A previous generation of the germanium photodiodes from [91] was used in the fabricated PIC with a responsivity of 0.5 A/W and a measured small-signal bandwidth of > 30 GHz. The photodiodes had been placed at several CDN branches as indicated in fig. 7.6(b). In this case, only one single-ended signal was measured and the probe head was connected either to the oscilloscope or to the amplifier and the ESA. The reverse bias was set to 3 V exactly

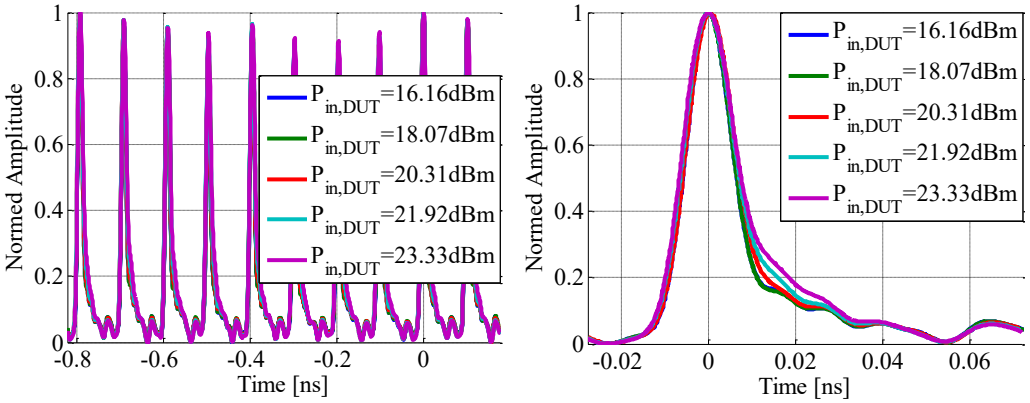

Figure 7.9: Normed PD output for varying average optical input power. An average of 1024 measurements has been used at the oscilloscope for noise suppression. The photodiode reverse bias was set to 3 V. (a) Ten pulses of the PD output (b) Zoom to a single pulse of the PD output

like in the OECC, and the chip temperature was kept constant at 25 °C. The measured output signal in the time domain is shown in fig. 7.9. Each pulse form represents an average over 1024 measurements at the oscilloscope. It was performed for noise suppression. In fig. 7.9(a), ten recorded pulses of the pulse train are shown. An amplitude variation can be seen which repeats after eight pulses. This is a consequence of the non-ideal optical interleaving for repetition rate multiplication. The tolerances of the 3 dB couplers used for splitting and combination within the optical 1x8 interleaver induce these amplitude fluctuations. Its periodicity confirms this conclusion. In fig. 7.9(b), a zoom to the first pulse of the 8-pulse sequence is shown. As can be seen, the PD begins to saturate for an average optical input power at the DUT of > 20 dBm. This corresponds to an optical power of > 5.4 dBm at the photodiode assuming a CDN loss of $\alpha_{CDN} = 14.6$ dB. Here, a splitting loss of 9 dB of the 3 MMI couplers is considered as well as 5.6 dB loss of the input grating, the waveguide loss and the fiber facet known from the CDN loss measurements by means of the optical CDN output. Furthermore, assuming a quantum efficiency of $\eta_{eff} = 0.5$ leads to a detected pulse energy of $E_{p,PD} > 173$ fJ. However, the power-dependent impulse response variation is very small and affects only the falling edge. Since the OECC circuit is triggered by the rising edge of the PD impulse response, it should not affect the OECC jitter performance. The 10 %-90 % rise time was measured as 8.5 ps, while the corresponding falling edge was 26 ps long. Clearly it is beneficial to use the rising edge of the impulse response to trigger electronic circuits. The width of the impulse response was measured as $\tau_{e,FWHM} = 13$ ps. The corresponding spectrum at the photodiode output is shown in fig. 7.10. Besides the 10 GHz fundamental harmonic, several spurs can be identified in a distance of a multiple of

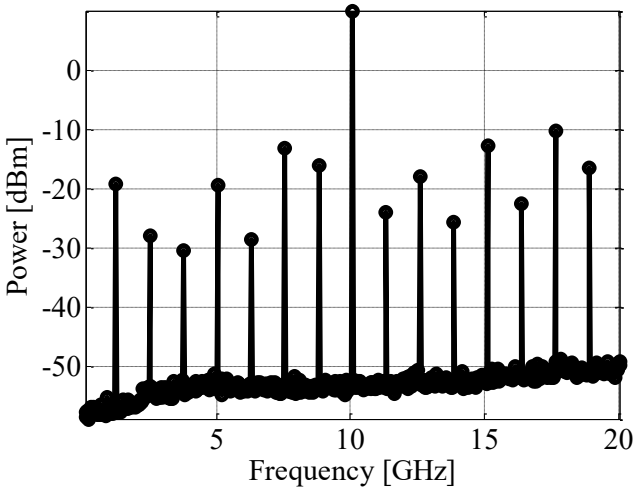

Figure 7.10: Measured photodiode output spectrum for an average optical input power of 16 dBm at the DUT. A 29 dB electronic amplifier has been used in front of the ESA.

1.25 GHz. It results again from the non-ideal optical interleaving.

Now, the measurements at the OECC circuit are addressed. Several devices from different dies and wafers were characterized with very similar results. Therefore, the results of one single representative device will be introduced in the following. Possible deviations to other devices will be stated. The OECC output in the time-domain is shown in fig. 7.11 for a varying averaged optical input power. The internal voltage was adjusted to its specified value of 4.5 V, while the supply current was in the range of 185 mA-195 mA and increased slightly for higher optical input power. Each measured single-ended output of the OECC circuit is shown in figs. 7.11(a) and 7.11(b). An average of 1024 measurements was performed by the oscilloscope for noise suppression. The electronic circuit operated for an average optical input power of > 14 dBm at the DUT input and showed only slight changes for higher input power. This corresponds to an optical power of > -0.8 dBm at the photodiode assuming again a CDN loss of $\alpha_{CDN} = 14.6$ dB. Taking a quantum efficiency of $\eta_{PD} = 0.5$ into account, leads to a detected pulse energy at the photodiode of $E_{p,PD} > 40$ fJ.

The periodic signals in fig. 7.11 correspond to the desired 5 GHz square wave form. The 10 %-90 % rise time was 16.3 ps. The difference of these single-ended outputs represents the actually wanted signal. But its measurement is very challenging since ideally there should be no phase differences between the signals during the difference operation. Unfortunately, this could not be assured during the measurement. As a matter of fact, phase-matched cables were not available and the probe head already induced a phase mismatch between the output ports. Therefore, a combination of these signals is a very critical operation and the measurement results should be handled carefully. Nevertheless, the difference operation was realized by a hybrid-coupler and the measured time response is shown in fig. 7.12(a).

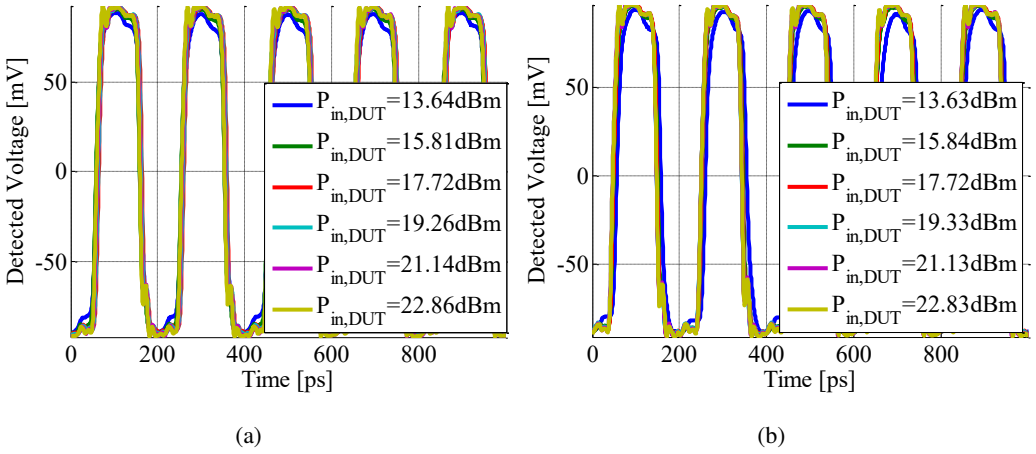

Figure 7.11: Measured single-ended outputs of the OECC circuit for varying average optical input power. An average of 1024 measurements has been used at the oscilloscope for noise suppression. (a) First single-ended OECC output signal (b) Second single-ended OECC output signal

The insertion loss and the limited bandwidth of the hybrid-coupler attenuated and distorted the signal form. Because of that, the 10 %-90 % rise time was almost doubled to 31.1 ps. The measured spectral output for an average optical input power of 15.8 dBm is shown in fig. 7.12(b). The spurs in a distance of a multiple of 1.25 GHz from the harmonics result from the non-ideal optical interleaver. This was observed already at the photodiode output in fig. 7.10.

Finally, the jitter performance was characterized by means of phase noise measurements introduced in section 3.4. The jitter can be calculated from the phase noise by eq. (3.19). The offset frequency-dependent phase noise $L_{\varphi_n}(f)$ was measured by *R&S FSUP50 Signal Source Analyzer*. An internal PLL locked to the first harmonic which was used for the phase noise measurement. The PLL bandwidth was automatically set to 1 kHz and represented the lowest measurable offset frequency. The correlation-based measurement mode was chosen for highest possible phase noise sensitivity. Averaged traces were recorded without any smoothing operations so that spurs were not suppressed. The highest measurable offset frequency for the chosen measurement mode was 30 MHz. Higher offset frequencies could not be measured with a sufficiently high sensitivity.

The measured phase noise of the differential OECC output after the hybrid-coupler is shown in fig. 7.13(a) for a varying average optical input power at the DUT. As can be seen, the phase noise did not change for an input power of > 16 dBm. In fig. 7.13(b), the phase noise of both single-ended OECC outputs is shown together with the phase noise of the differential signal after the hybrid-coupler and the phase noise of the used MLL. In the figure, the laser phase noise was reduced by 6 dB regarding the frequency division operation by the

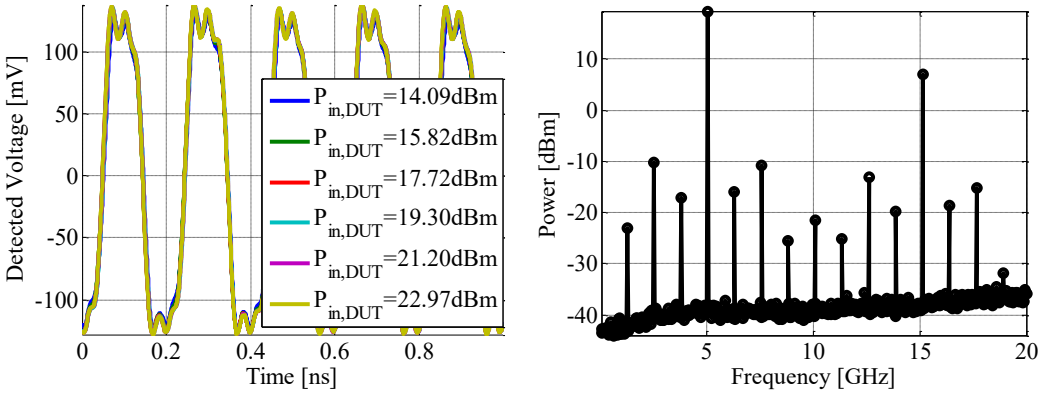

(a) (b)

Figure 7.12: Measured differential output at the hybrid-coupler: (a) Measured time response averaged over 1024 measurements at the oscilloscope for noise suppression. (b) Output spectrum of the differential signal for an average optical input power of 15.8 dBm.

OECC. As can be seen, the differential signal shows up to 3 dB less phase noise in the offset frequency range of 40 kHz-5 MHz. This might prove the noise suppression of the difference operation but it should be noted that this behavior was not observed for other devices. It might be the case that after a reconstruction of the measurement set-up, accidentally an optimum combination of cables and adapters had been chosen so that the electrical paths matched. Fig. 7.13(b) shows that the phase noise performance is completely dominated by the used MLL up to an offset frequency of 40 kHz. Only higher offset frequency phase noise can be attributed to the OECC circuit.

The jitter contribution can be divided in three regions. In the offset frequency range of 1 kHz-2 kHz, the integrated jitter results in 24 fs and stems completely from the laser. The residual measured phase noise within the offset frequency range of 2 kHz-30 MHz contributes an additional jitter of < 1 fs. The jitter contribution of higher offset frequency fluctuations can be assessed. A white phase noise level of -161 dBc/Hz was achieved for the highest offset frequencies as can be seen in fig. 7.13(a). Its origin can be referred to thermal noise within the signal measurement path as explained in the following. The phase noise measurement was performed at the 5 GHz spectral line. Its power was measured to 18.8 dBm at the ESA. Assuming 0.7 dB loss for the cable and the adapters results in 19.5 dBm output power of the used 29 dB electronic amplifier what corresponds to an input power of -9.5 dBm. The thermal noise level of a $50\,\Omega$ resistance referenced to a signal power level of 0 dBm corresponds to -174 dBc/Hz. Discarding the amplitude noise contribution leads to a relative phase noise level of -177 dBc/Hz [74]. Considering the actual input power results in a relative phase noise level of -167.5 dBc/Hz before the amplifier. Taking the amplifier noise figure of 6 dB (according to the data sheet) into account leads to

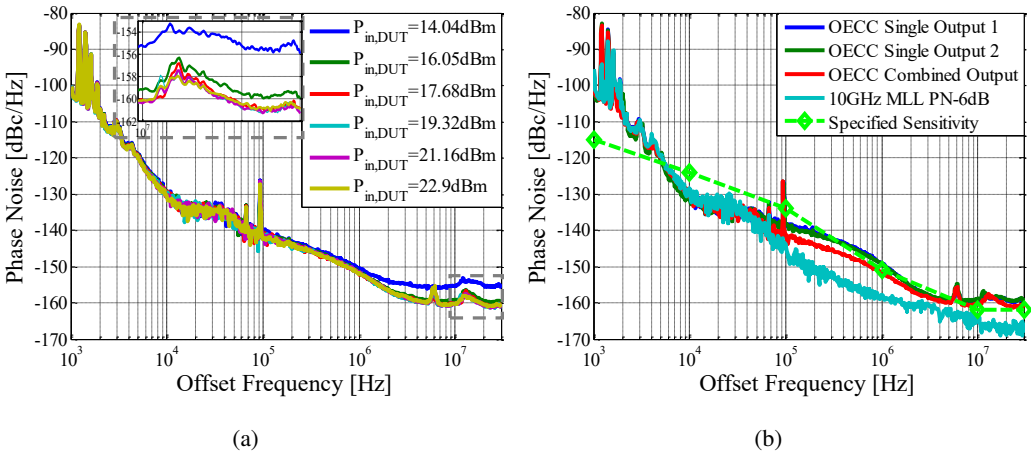

Figure 7.13: (a) Phase noise of the differential signal output after the hybrid-coupler for a varying average optical input power. (b) Phase noise of single-ended and differential OECC outputs for an average optical input power of 21 dBm. The phase noise of the used MLL is shown minus 6 dB regarding the frequency division by the OECC. Specified phase noise sensitivity of the ESA is indicated by green markers.

a phase noise level of -161.5 dBc/Hz after the amplifier, which is very close to the measured values shown in fig. 7.13. Following this discussion, the actual phase noise level of the measured device should be -167 dBc/Hz if the noise figure of the electronic amplifier is subtracted [74, 172]. Integration of this value up to the Nyquist frequency of 2.5 GHz results in an additional jitter of 10 fs. This value corresponds very well to the theoretically derived jitter performance of rising edge clocked circuits from section 6.4. Furthermore, the measured phase noise was either very close or under the specified ESA sensitivity which was taken from the data sheet and is indicated in fig. 7.13(b) by the green markers. It should be noted that the laser phase noise was measured at the doubled frequency of 10 GHz. Due to the frequency division operation by the OECC circuit, it was reduced by 6 dB in fig. 7.13(b) for better comparison. Therefore, its lowest measured phase noise level was also very close to the specified measurement sensitivity for the highest offset frequencies.

Finally, the non-linear losses were measured within the optical CDN. The results are shown in fig. 7.14. As can be seen for the ultra-short pulses of $\tau_{o,FWHM} = 300$ fs non-linear losses were negligible for an optical input power of up to 21 dBm. For the analysis, the pulses were broadened by an optical BPF placed in front of the EDFA. The resulting pulse width was $\tau_{o,FWHM} = 3.5$ ps. Again, both pulse widths resulted from a measured optical 3 dB bandwidth and an assumed Gaussian time-bandwidth product. Surprisingly, the non-linear losses were stronger for the broader pulses although the intensities within the silicon waveguides were much lower. These observations were already discussed in the non-linear pulse propagation experiments in section 7.2. All in all, this behavior was not

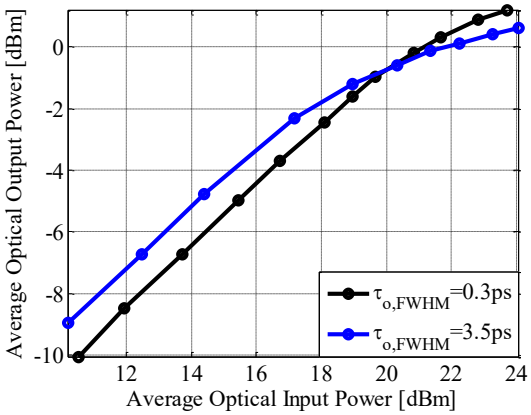

Figure 7.14: Optical output power in dependence on the optical input power for different optical pulse widths.

expected and indicates limits of the theory introduced in section 4.2.1 for ultra-short pulses. Fortunately, this effect is very beneficial for photonic ADCs since shorter pulses induce less jitter according to the analysis in chapter 6. Subtracting losses at the fiber facet, which are known from previous fiber-to-fiber transition experiments, results in typical CDN loss of $18.5\,\mathrm{dB}$ (including output grating) in the linear region. The $9\,\mathrm{dB}$ splitting loss due to the three 1x2 MMI coupler results in $0.5\,\mathrm{dB}$ waveguide loss and $4.5\,\mathrm{dB}$ grating coupler loss for the $\tau_{o,FWHM} = 300\,\mathrm{fs}$ pulses. The grating coupler loss shrinks by $0.5\,\mathrm{dB}$ for the $\tau_{o,FWHM} = 3.5\,\mathrm{ps}$ pulses since these are less affected by the grating filter function. This stems from the filter characteristic of the limited grating bandwidth which has a stronger impact on ultra-short pulses.

In summary, the main jitter contribution was generated for offset frequencies of $< 2\,\mathrm{kHz}$ and stemmed from the used laser. This is expected due to the poor jitter characteristics of MLLs for low frequency fluctuations. However, that does not have to be a serious problem for an application. For example, if the photonic ADCs are used in a real-time oscilloscope, very high sampling rates can fill the device memory within $1\,\mathrm{ms}$ and, therefore, frequency fluctuations of $< 1\,\mathrm{kHz}$ would not affect a recorded data set. And before the next data set is measured, the frequency can be adapted again. Low frequency drifts are usually filtered by a PLL with a bandwidth of up to $1\,\mathrm{kHz}$. The measured fundamental limited jitter for offset frequencies of $> 30\,\mathrm{kHz}$ corresponded to the fundamental jitter limit for the rising edge sampler in section 6.2. The assessed value of $10\,\mathrm{fs}$ from the measured phase noise value fits very well to the calculated achievable jitter performance for rising edge samplers.

Chapter 8

Summary

The sampler basics were introduced in chapter 2. Here, several important effects were presented which decrease the ADC resolution in terms of ENOB. Timing jitter, as the sampling instant uncertainty, was identified as the crucial issue if high frequency signals are sampled. Another important issue on high frequency sampling is the comparator ambiguity. But it is much less harmful since time-interleaved ADC architectures relax the device speed requirements. Such architectures are preferred to achieve high sampling rates. The evolution of electronic ADC performance was discussed as well as the problems regarding jitter performance of electronic clock generation and its distribution on chip. The focus of this thesis on photonic ADCs was motivated by the fact that no improvement has been achieved regarding the clock precision in the last decade. Here, a clock jitter of $\sim 100\,\mathrm{fs}$ was identified as a limit for electronic clock signals on chip. Furthermore, no improvement is expected in the near future simply due to physical restrictions.

In chapter 4, the silicon photonics platform was introduced and was able to integrate optics and electronics in a CMOS process. Moreover, the performance of essential devices was discussed which are relevant for the implementation of integrated photonic ADCs. Here, the focus was on the silicon photonics BiCMOS platform from [96] since it had been used to fabricate the test structures presented in chapter 7.

In chapter 5, optical pulse trains were discussed as a solution to achieve more precise clock signals. The ultra-low jitter performance of MLLs was introduced. These achieve orders of magnitude less jitter than electronic oscillators. Because of that, the potential of photonic ADCs was discussed in regard of several architectures suggested in former publications about this topic. Here, the focus was set on photonic sampling and electronic quantization since the sampling process is highly dependent on the timing precision, and the digitization can be performed well by electronics. In this context, two sampling instants were identified. Namely, the rising edge of the induced electrical pulses and the center of mass either

of the optical or the induced electrical pulses. It led to the distinction between a rising edge and a center of mass sampler architecture. The theoretical performance limits for both photonic ADC architectures were addressed in chapter 6 which represents the focus of this thesis. A quantum noise model was provided able to describe the noise impact on integrated photonic ADCs. Formulas were derived to assess the ADC performance taking shot noise, ASE noise of an optional EDFA, thermal noise, pulse-to-pulse energy fluctuations and several characteristics of the system components such as the photodiode bandwidth, the optical pulse width and others into account. For the rising edge sampler, a fundamental jitter limit of $\sim 10\,\text{fs}$ was derived. For the center of mass sampler, a fundamental jitter limit of $\sim 1\,\text{fs}$ seems possible. But in this case, the ADC resolution is limited by pulse-to-pulse energy fluctuations to $< 9\,\text{ENOB}$. These values were derived for realistic characteristics of the system components. Significantly better performance is unlikely since state-of-the-art MLLs can not provide much higher optical power. But even if this was possible to achieve, non-linearities within the silicon waveguides would deteriorate this advantage.

In chapter 7, several test structures have been characterized. Here, skew and non-linearity measurements have been performed for experimental verification of the optical CDN properties. The skew was measured to $< 100\,\text{fs}$ for delay lines up to $75\,\text{ps}$ which is much lower than in electrical CDNs. Unfortunately, the temperature dependence still necessitate a compensation of the skew. The non-linear behavior of ultra-short optical pulses in silicon waveguides deviates from the widely used model which had also been found by others [118, 121]. Nevertheless, the surprisingly lower loss for ultra-short optical pulses is beneficial for photonic ADCs since higher detected pulse energies and shorter pulses decrease the jitter.

Additionally, an OECC was fabricated and characterized as well. The precision of the generated square wave electrical signal depends on the rising edge of the detected pulses. Therefore, it corresponds to the case of a rising edge sampler. Its fundamental jitter limit was assessed by phase noise measurements to $10\,\text{fs}$ for high offset frequency fluctuations in the range of $30\,\text{MHz}$-$2.5\,\text{GHz}$. Only $1\,\text{fs}$ could be attributed to the electronic circuit within the measurable range of $1\,\text{kHz}$-$30\,\text{MHz}$, while the main jitter of $24\,\text{fs}$ resulted from the poor low frequency fluctuation characteristic of the used MLL. The fundamental jitter limit of $10\,\text{fs}$ corresponds very well to the analytically derived value and confirms the calculations. In fact, the generated ultra-low jitter square wave signal can be used to clock electronic ADCs. The formulas for center of mass jitter had been found independently and through different mathematical derivation parallel by two other authors [69, 168] if the optical amplifier and the CDN is neglected. This confirms its correctness. Recently, an actual $10\,\text{GS/s}$ electrical center of mass sampler was shown in [159] as proposed and analyzed in section

6.3. It was realized by the silicon photonics BiCMOS platform from [95] which was introduced in chapter 4. A bandwidth of $> 30\,\mathrm{GHz}$ was achieved with an SNR of $35\,\mathrm{dB}$ and a total harmonic distortion of $< -33\,\mathrm{dB}$. Here, a jitter of $< 30\,\mathrm{fs}$ was derived by means of time-domain correlation measurements of two parallel samplers. But an optical power mismatch between both samplers could have prevented better jitter results as discussed in [159]. The corresponding gain and bandwidth mismatches between both samplers prohibited complete cancellation of the impact of the signal generator used for the measurements which had a jitter of $80\,\mathrm{fs}$. Nevertheless, the results showed that low jitter values can be achieved by this principle.

In conclusion, photonic integrated ADCs are able to achieve one or two orders of magnitude better jitter performances than electronic ADCs. The silicon photonics platform already enables its implementation. However, its success strongly depends on the MLLs which have to provide ultra-low jitter pulse trains with high repetition rates, sufficiently high power and in a cost-efficient way.

Appendix A

Derivation of the Optical Pulse Train Intensity Spectrum

Applying the finite-time Fourier transform, defined in eq. (3.16), to eq. (3.34) results in

$$\begin{aligned} I_T(f) &= I_{0,T}(f) * \left[\delta(f) + \frac{1}{2\pi} A_{n,T}(f)\right] + \frac{1}{2\pi}\left[j2\pi f \cdot I_{0,T}(f)\right] * \frac{\Phi_{n,T}(f)}{2\pi f_T} \\ &= \left[I_p(f) \cdot f_T \delta_{f_T}(f)\right] * \left[\delta(f) + \frac{1}{2\pi} A_{n,T}(f)\right] + \left[jf \cdot I_p(f) \cdot f_T \delta_{f_T}(f)\right] * \frac{\Phi_{n,T}(f)}{2\pi f_T} \end{aligned} \tag{A.1}$$

where the Fourier transform relations [40, 66]

$$\mathcal{F}\left\{\frac{\mathrm{d}^n x(t)}{\mathrm{d}t^n}\right\}(f) = (j2\pi f)^n \cdot X(f), \tag{A.2}$$

$$\mathcal{F}\{x(t) * y(t)\}(f) = X(f) \cdot Y(f) \qquad \text{and} \tag{A.3}$$

$$\mathcal{F}\{x(t) \cdot y(t)\}(f) = \frac{1}{2\pi} X(f) * Y(f) \tag{A.4}$$

have been applied. Furthermore, $I_0(f)$ has been substituted by the Fourier transform of eq. (3.32) and the relation $f_T = 1/T_p$ has been used. Eq. (A.1) can be simplified to

$$\begin{aligned} I_T(f) = &\left[f_T \sum_{\mu=-\infty}^{\infty} I_p(\mu f_T) \cdot \delta(f - \mu f_T)\right] * \left[\delta(f) + \frac{1}{2\pi} A_{n,T}(f)\right] + \\ &\frac{j}{2\pi}\left[\sum_{\mu=-\infty}^{\infty} \mu f_T \cdot I_p(\mu f_T) \cdot \delta(f - \mu f_T)\right] * \Phi_{n,T}(f) \\ = f_T &\sum_{\mu=-\infty}^{\infty} I_p(\mu f_T)\left[\delta(f - \mu f_T) + \frac{1}{2\pi} A_{n,T}(f - \mu f_T) + \frac{j\mu}{2\pi} \Phi_{n,T}(f - \mu f_T)\right]. \end{aligned} \tag{A.5}$$

Amplitude and phase fluctuations can be assumed as uncorrelated and concentrated as sidebands close to each harmonic of the order μ and with negligible impact on nearby harmonics

of the orders $\mu - 1$ and $\mu + 1$. Therefore, the squared absolute value of eq. (A.5) results in

$$|I_T(f)|^2 = f_T^2 \sum_{\mu=-\infty}^{\infty} |I_p(\mu f_T)|^2 \cdot \left[\delta(f - \mu f_T) + \frac{1}{(2\pi)^2}|A_{n,T}(f - \mu f_T)|^2 + \frac{\mu^2}{(2\pi)^2} \cdot |\Phi_{n,T}(f - \mu f_T)|^2\right]. \quad \text{(A.6)}$$

The optical pulse train intensity spectrum results from eq. (3.14). Using the notations

$$S_I(f) = \lim_{T\to\infty} \frac{1}{T}|I_T(f)|^2 \quad \text{(A.7)}$$

$$S_{I_p}(f) = |I_p(f)|^2 \quad \text{(A.8)}$$

$$S_{a_n}(f) = \lim_{T\to\infty} \frac{1}{T}|A_{n,T}(f)|^2 \quad \text{(A.9)}$$

$$S_{\varphi_n}(f) = \lim_{T\to\infty} \frac{1}{T}|\Phi_{n,T}(f)|^2 \quad \text{(A.10)}$$

for the spectra of the pulse train intensity, the ideal pulse intensity envelope and the amplitude and phase fluctuations leads to eq. (3.35).

Appendix B

Derivation of the Photocurrent Spectrum of a Detected Optical Pulse Train

In this section, the photocurrent spectrum is derived which is induced by photodetection of an optical pulse train.
For this purpose, the noise model from fig. 6.1 is extended to a pulse train with the repetition rate f_{rep} by replacement of the optical field envelope of a single pulse in eqs. (6.8) and (6.9) by its periodic version

$$A(t) \rightarrow A(t) * \delta_{T_{rep}}(t) \tag{B.1}$$

where $\delta_{T_{rep}}(t)$ represents a Dirac comb with the time period $T_{rep} = 1/f_{rep}$. The resulting double-sided photocurrent PSD can be calculated by

$$\begin{aligned}
S_i(f) &= \lim_{T\to\infty} \frac{1}{T} \left\langle \left| \mathcal{F}_T \left\{ i(t) \right\} (f) \right|^2 \right\rangle \\
&= \lim_{T\to\infty} \frac{1}{T} \left(\lim_{f'\to f} \left\langle \mathcal{F}_T \left\{ i_d(t) + i_{n,opt}(t) \right\} (f) \cdot \mathcal{F}_T^* \left\{ i_d(t') + i_{n,opt}(t') \right\} (f') \right\rangle \right) \\
&= \lim_{T\to\infty} \frac{1}{T} \left(\lim_{f'\to f} \left(\mathcal{F}_T \left\{ i_d(t) \right\} (f) \cdot \mathcal{F}_T^* \left\{ i_d(t') \right\} (f') \right) \right) + \\
&\quad \lim_{T\to\infty} \frac{1}{T} \left(\lim_{f'\to f} \left\langle \mathcal{F}_T \left\{ i_{n,opt}(t) \right\} (f) \cdot \mathcal{F}_T^* \left\{ i_{n,opt}(t') \right\} (f') \right\rangle \right) + \\
&\quad \lim_{T\to\infty} \frac{1}{T} \left(\lim_{f'\to f} \left\langle \mathcal{F}_T \left\{ i_{n,opt}(t) \right\} (f) \cdot \mathcal{F}_T^* \left\{ i_d(t') \right\} (f') \right\rangle \right) + \\
&\quad \lim_{T\to\infty} \frac{1}{T} \left(\lim_{f'\to f} \left\langle \mathcal{F}_T \left\{ i_d(t) \right\} (f) \cdot \mathcal{F}_T^* \left\{ i_{n,opt}(t') \right\} (f') \right\rangle \right) \\
&= S_{i,1}(f) + S_{i,2}(f) + S_{i,3}(f) + S_{i,4}(f)
\end{aligned} \tag{B.2}$$

where the finite-time Fourier transform definition from eq. (3.16) and the PSD definition from eq. (3.14) have been used. This leads to the expression in eq. (B.2) consisting of four terms. $S_{i,1}(f)$ has only contributions from the deterministic photocurrent $i_d(t)$ and, therefore, the ensemble average is removed. $S_{i,2}(f)$ has only components from the photocurrent noise $i_{n,opt}(t)$, while $S_{i,3}(f)$ and $S_{i,4}(f)$ contain the beating between deterministic and noise currents. In the following each expression will be addressed individually. Using eq. (6.8) for the deterministic photocurrent $i_d(t)$ with the extension from a single pulse to a pulse train from eq. (B.1), the first term results in

$$\begin{aligned} S_{i,1}(f) = R_p^2 G^2 \eta_{eff}^2 \lim_{T\to\infty} \frac{1}{T} \Bigg(\lim_{f'\to f} \Big(\mathcal{F}_T \left\{ |A(t)|^2 * \delta_{T_{rep}}(t) \right\}(f) \cdot G_{PD}(f) \cdot \\ \mathcal{F}_T^* \left\{ |A(t')|^2 * \delta_{T_{rep}}(t') \right\}(f') \cdot G_{PD}^*(f') \Big) \Bigg) \\ = R_p^2 G^2 \eta_{eff}^2 \left| P_{opt}(f) \right|^2 \left| G_{PD}(f) \right|^2 \end{aligned} \tag{B.3}$$

where the PSD of the optical power envelope of the pulse train at the MLL output from eq. (6.37) and the Fourier transform relation from eq. (A.3) have been used. The deterministic photocurrent PSD $S_{i,1}(f)$ results from the optically induced current $R_p^2 G^2 \eta_{eff}^2 |P_{opt}(f)|^2$ scaled by the amplitude spectrum of the PD transfer function $|G_{PD}(f)|^2$.
The second term in eq. (B.2) can be split into the four components

$$\begin{aligned} S_{i,2}(f) = \lim_{T\to\infty} \frac{1}{T} \left(\lim_{f'\to f} \left\langle \mathcal{F}_T \left\{ i_{n,vac}(t) \right\}(f) \cdot \mathcal{F}_T^* \left\{ i_{n,vac}(t') \right\}(f') \right\rangle \right) + \\ \lim_{T\to\infty} \frac{1}{T} \left(\lim_{f'\to f} \left\langle \mathcal{F}_T \left\{ i_{n,ASE}(t) \right\}(f) \cdot \mathcal{F}_T^* \left\{ i_{n,ASE}(t') \right\}(f') \right\rangle \right) + \\ \lim_{T\to\infty} \frac{1}{T} \left(\lim_{f'\to f} \left\langle \mathcal{F}_T \left\{ i_{n,vac}(t) \right\}(f) \cdot \mathcal{F}_T^* \left\{ i_{n,ASE}(t') \right\}(f') \right\rangle \right) + \\ \lim_{T\to\infty} \frac{1}{T} \left(\lim_{f'\to f} \left\langle \mathcal{F}_T \left\{ i_{n,ASE}(t) \right\}(f) \cdot \mathcal{F}_T^* \left\{ i_{n,vac}(t') \right\}(f') \right\rangle \right) \\ = S_{i,2a}(f) + S_{i,2b}(f) + S_{i,2c}(f) + S_{i,2d}(f) \end{aligned} \tag{B.4}$$

referring to the beating terms of shot and ASE noise. Here, the last two terms are $S_{i,2c}(f) = S_{i,2d}(f) = 0$ since shot and ASE noise are not correlated. Using the expression in eq. (6.9) for the photocurrent noise $i_{n,vac}(t)$ stemming from vacuum fluctuations with the extension from a single pulse approach to a pulse train from eq. (B.1) results in

$$\begin{aligned} S_{i,2a}(f) = 4 R_p^2 G \eta_{eff} \lim_{T\to\infty} \frac{1}{T} \Bigg(\lim_{f'\to f} \Big\langle \mathcal{F}_T \left\{ \mathrm{Re}\{ [A(t) * \delta_{T_{rep}}(t)] \cdot n_{vac}(t) \} \right\}(f) \cdot \\ G_{PD}(f) \cdot \mathcal{F}_T^* \left\{ \mathrm{Re}\{ [A(t') * \delta_{T_{rep}}(t')] \cdot n_{vac}(t') \} \right\}(f') \cdot G_{PD}^*(f') \Big\rangle \Bigg). \end{aligned} \tag{B.5}$$

Assuming a real optical field envelope $A(t)$ and using the finite-time Fourier transform definition from eq. (3.16) leads to the shot noise contribution

$$\begin{aligned}
S_{i,2a}(f) &= 4R_p^2 G\eta_{eff} \lim_{T\to\infty} \frac{1}{T}\Bigg(\lim_{f'\to f} \Bigg[\int_{-\frac{T}{2}}^{\frac{T}{2}} \int_{-\frac{T}{2}}^{\frac{T}{2}} [A(t) * \delta_{T_{rep}}(t)][A(t') * \delta_{T_{rep}}(t')] \cdot \\
&\qquad \left\langle \mathrm{Re}\{n_{vac}(t)\}\, \mathrm{Re}\{n_{vac}(t')\} \right\rangle e^{-j2\pi f t} e^{j2\pi f' t'} \mathrm{d}t\mathrm{d}t' \cdot G_{PD}(f) G_{PD}^*(f') \Bigg] \Bigg) \\
&= 4R_p^2 G\eta_{eff} \frac{h\nu_c}{4} \lim_{T\to\infty} \frac{1}{T}\Bigg(\lim_{f'\to f} \Bigg[G_{PD}(f) G_{PD}^*(f') \cdot \\
&\qquad \int_{-\frac{T}{2}}^{\frac{T}{2}} [|A(t)|^2 * \delta_{T_{rep}}(t)] e^{-j2\pi(f-f')t} \mathrm{d}t \Bigg] \Bigg) \\
&= R_p^2 G\eta_{eff} h\nu_c \left|G_{PD}(f)\right|^2 P_{avg} \\
&= qI_{avg} \left|G_{PD}(f)\right|^2 . \qquad \text{(B.6)}
\end{aligned}$$

Here, the ACF of the real part of the vacuum fluctuations corresponds to half of the expression in eq. (6.4) since the PSD is equally distributed between the real and the imaginary part [101]. Furthermore, eq. (6.37) has been used. The notation $P_{avg} = P_{opt}(0)$ has been introduced and refers to the average optical power of the pulse train emitted by the MLL. Finally, after applying the relation $R_p = q/h\nu_c$, the average photocurrent from eq. (6.38) has been introduced for simplification. It results into the simple expression in eq. (B.6). The expression describes the amplitude spectrum of the shot noise for the photodetection of an optical pulse train and corresponds exactly to the case of photodetection of CW light.
The direct impact of ASE noise on the pulse center of mass position is described by $S_{i,2b}(f)$ in eq. (B.4). Its calculation is identical to the calculation of $S_{i,2a}(f)$ in eq. (B.6). Considering the additional attenuation of the ASE noise by η_{eff} and a different corresponding ACF from eq. (6.1) with the expression in eq. (6.3) leads to the ASE-noise-related photocurrent noise

$$S_{i,2b}(f) = qI_{avg}\eta_{eff}(FG-1)\left|G_{PD}(f)\right|^2 . \qquad \text{(B.7)}$$

The calculation steps for $S_{i,3}(f)$ and $S_{i,4}(f)$ from eq. (B.2) are very similar to the upper derivation of $S_{i,2}(f)$. The only difference is that the expressions for the ensemble averages reduces to the single stochastic variables which are $\langle \mathrm{Re}\{n_{vac}(t)\}\rangle$ for the vacuum fluctuations and $\langle \mathrm{Re}\{n_{ASE}(t)\}\rangle$ for the ASE noise. Since both noise sources have a zero mean value, these ensemble averages are zero so that $S_{i,3}(f) = S_{i,4}(f) = 0$. In summary, the photocurrent PSD from eq. (B.2) results into eq. (6.36) as a sum of eqs. (B.3), (B.6) and (B.7).

Appendix C

Derivation of the Single-Sideband Amplitude and Phase Noise Floor

In this section, the SSB noise floor is derived for phase or amplitude noise measurements at arbitrary harmonics induced by the photodetection of optical pulse trains.
For this purpose, the noise model from fig. 6.1 is extended to a pulse train with the repetition rate f_{rep} by the substitution from eq. (B.1) in eqs. (6.8) and (6.9). In an actual phase noise measurement system, a BPF follows the PD and filters out the μ-th harmonic of the repetition rate which is schematically shown in fig. 6.4. The remaining harmonic is demodulated to the baseband and the phase noise spectrum is measured by an ESA with the terminating resistor R_Ω. A mathematical description of the double-sided noise PSD can be written as

$$
\begin{aligned}
S_m(f) &= \lim_{T\to\infty}\frac{1}{T}\left(\left\langle \left|\mathcal{F}_T\left\{(i(t)*g_{BP}(t))\cdot\cos(2\pi\mu f_{rep}t+\phi_r)\right\}(f)\right|^2\right\rangle R_\Omega\right)\\
&= \frac{R_\Omega}{4}\lim_{T\to\infty}\frac{1}{T}\Bigg(\Bigg\langle\Bigg|\mathcal{F}_T\left\{i_d(t)*g_{BP}(t)+i_{n,opt}(t)*g_{BP}(t)\right\}(f)*\\
&\qquad\qquad\left(\delta(f-\mu f_{rep})e^{j\phi_r}+\delta(f+\mu f_{rep})e^{-j\phi_r}\right)\Bigg|^2\Bigg\rangle\Bigg)\\
&= \frac{R_\Omega}{4}\lim_{T\to\infty}\frac{1}{T}\Bigg(\lim_{f'\to f}\Bigg\langle\Bigg[\left(\mathcal{F}_T\left\{i_d(t)\right\}(f)\cdot G_{BP}(f)+\right.\\
&\quad\left.\mathcal{F}_T\{i_{n,opt}(t)\}(f)\cdot G_{BP}(f)\right)*\left(\delta(f-\mu f_{rep})e^{j\phi_r}+\delta(f+\mu f_{rep})e^{-j\phi_r}\right)\Bigg]\cdot\\
&\quad\Bigg[\left(\mathcal{F}_T^*\left\{i_d(t')\right\}(f')\cdot G_{BP}^*(f')+\mathcal{F}_T^*\{i_{n,opt}(t')\}(f')\cdot G_{BP}^*(f')\right)*\\
&\qquad\left(\delta(f'-\mu f_{rep})e^{-j\phi_r}+\delta(f'+\mu f_{rep})e^{j\phi_r}\right)\Bigg]\Bigg\rangle\Bigg)\\
&= S_{m,1}(f)+S_{m,2}(f)+S_{m,3}(f)+S_{m,4}(f).
\end{aligned}
\tag{C.1}
$$

Eq. (6.7) has been used for the induced photocurrent $i(t)$ where the thermal noise contribution has been neglected. The thermal noise contribution from a load resistance is well known. Here, the focus is set on the shot and ASE noise characteristics at the photodetection process of ultra-short optical pulse trains. In eq. (C.1), $g_{BP}(t)$ is the BPF impulse response and $G_{BP}(f)$ is its Fourier transform. ϕ_r is a constant phase offset of the local oscillator relative to the μ-th harmonic. Its value is different for phase and amplitude noise measurements which will be discussed below. It should be noted that the Dirac functions as the result of the Fourier transform of the cosine function is valid for $T \to \infty$ and is a good approximation as long as $1/T \ll f_{rep}$. Once again the finite-time Fourier transform definition from eq. (3.16) and the Fourier transform relations [40]

$$\mathcal{F}\{\cos(at)\}(f) = \frac{1}{2}\left(\delta\left(f - \frac{a}{2}\right) + \delta\left(f + \frac{a}{2}\right)\right) \tag{C.2}$$

$$\mathcal{F}\{x(t-a)\}(f) = X(f) \cdot e^{-j2\pi af} \tag{C.3}$$

have been applied so that eq. (C.1) leads to four terms. Here, the resulting deterministic term $S_{m,1}(f)$ is independent of the photocurrent noise $i_{n,opt}(t)$, while the term $S_{m,2}(f)$ does not have the deterministic photocurrent $i_d(t)$. The two terms $S_{m,3}(f)$ and $S_{m,4}(f)$ include both the noise and the deterministic photocurrent. In the following, all four expressions are derived or discussed individually. The pure deterministic part results in

$$\begin{aligned} S_{m,1}(f) = \frac{R_\Omega}{4} \lim_{T\to\infty} \frac{1}{T} \Bigg(& \lim_{f'\to f} \\ & \Big[\left(\mathcal{F}_T\left\{i_d(t)\right\}(f) \cdot G_{BP}(f)\right) * \left(\delta(f-\mu f_{rep})e^{j\phi_r} + \delta(f+\mu f_{rep})e^{-j\phi_r}\right) \Big] \cdot \\ & \Big[\left(\mathcal{F}_T^*\left\{i_d(t')\right\}(f') \cdot G_{BP}^*(f')\right) * \left(\delta(f'-\mu f_{rep})e^{-j\phi_r} + \delta(f'+\mu f_{rep})e^{j\phi_r}\right) \Big] \Bigg) \end{aligned} \tag{C.4}$$

where the ensemble average disappears since there are no stochastic variables. At first, the product of the Fourier transforms of the detected deterministic photocurrent $i_d(t)$ and the BPF impulse response $g_{BP}(t)$ is addressed. Using the substitution from eq. (B.1) in eq. (6.8) extends the single pulse to a pulse train approach and leads for the mentioned product to

$$\begin{aligned} \mathcal{F}_T\left\{i_d(t)\right\}(f) \cdot G_{BP}(f) &= R_p G \eta_{eff} \mathcal{F}_T\left\{|A(t)|^2 * \delta_{T_{rep}}(t)\right\}(f) \cdot G_{PD}(f) \cdot G_{BP}(f) \\ &= R_p G \eta_{eff} P_{opt,T}(f) \cdot \tilde{G}(f) \\ &= R_p G \eta_{eff} |P_{opt,T}(\mu f_{rep})| \cdot |\tilde{G}(\mu f_{rep})| \cdot \\ \Big(\delta(f-\mu f_{rep})e^{j(\phi_p(\mu f_{rep})+\phi_g(\mu f_{rep}))} &+ \delta(f+\mu f_{rep})e^{j(\phi_p(-\mu f_{rep})+\phi_g(-\mu f_{rep}))}\Big). \end{aligned} \tag{C.5}$$

$\tilde{G}(f) = G_{PD}(f)G_{BP}(f)$ is the Fourier transform of the concatenated PD and BPF impulse responses $g_{PD}(t) * g_{BP}(t)$ and $P_{opt,T}(f)$ is the finite-time Fourier transform of the

pulse train optical power envelope defined in eq. (6.37), while $\phi_g(f)$ and $\phi_p(f)$ are their corresponding phases. In the frequency domain $P_{opt,T}(f)$ corresponds to a Dirac comb scaled by the Fourier transform of the optical pulse power envelope. Thanks to the BPF in eq. (C.5), all Dirac functions are suppressed except the μ-th harmonic within the passband where the measurement is performed. This results into the two remaining Dirac functions of the double-sided PSD. Using eq. (C.5) in eq. (C.4) leads to

$$S_{m,1}(f) = \frac{R_\Omega}{4}\left(R_p G \eta_{eff}\right)^2 |P_{opt}(\mu f_{rep})|^2 |\tilde{G}(\mu f_{rep})|^2 \cdot \Big[\delta(f - 2\mu f_{rep}) + \delta(f + 2\mu f_{rep}) + 2\delta(f) \cdot (1 + \cos(2(\phi_p(\mu f_{rep}) + \phi_g(\mu f_{rep}) - \phi_r)))\Big] \tag{C.6}$$

where the phase condition $\phi(f) = -\phi(-f)$ has been used valid for Fourier transforms of the real functions of the pulse train optical power envelope and the PD and BPF impulse responses. Moreover, the relation $\cos(x) = (e^{jx} + e^{-jx})/2$ has been applied. The phase ϕ_r of the local oscillator is adjusted by the PLL so that the phase condition

$$\phi_p(\mu f_{rep}) + \phi_g(\mu f_{rep}) - \phi_r = \begin{cases} \pi/2, & \text{for phase noise measurements} \\ 0, & \text{for amplitude noise measurements} \end{cases} \tag{C.7}$$

is fulfilled for phase or amplitude noise measurement, respectively. Finally, using the phase noise condition in the argument of the cosine function in eq. (C.6) leads to

$$S_{m,1}(f) = \frac{R_\Omega}{4}(R_p G \eta_{eff})^2 |P_{opt}(\mu f_{rep})|^2 |\tilde{G}(\mu f_{rep})|^2 \left[\delta(f - 2\mu f_{rep}) + \delta(f + 2\mu f_{rep})\right]. \tag{C.8}$$

Thus, only the unavoidable harmonics at the frequencies $f = \pm 2\mu f_{rep}$ remain from the deterministic photocurrent due to the mixing process. These are suppressed when the ESA measures the phase noise stepwise in narrow bandwidths.

In eq. (C.8), the bandpass-filtered and down-converted noise free part of the photocurrent PSD has been derived by expanding eq. (C.1) and considering the first term $S_{m,1}(f)$ without the noise contribution $i_{n,opt}(t)$. Now the noise contribution to the photocurrent PSD is addressed. After expanding eq. (C.1), the second term corresponds to

$$S_{m,2}(f) = \frac{R_\Omega}{4} \lim_{T\to\infty} \frac{1}{T} \Bigg(\lim_{f'\to f} \Bigg\langle \Bigg(\left[\mathcal{F}_T\{i_{n,opt}(t)\}(f) G_{BP}(f)\right] * \Big[\delta(f - \mu f_{rep}) e^{j\phi_r} + \delta(f + \mu f_{rep}) e^{-j\phi_r}\Big] \Bigg) \Bigg(\left[\mathcal{F}_T^*\{i_{n,opt}(t')\}(f') G_{BP}^*(f')\right] * \Big[\delta(f' - \mu f_{rep}) e^{-j\phi_r} + \delta(f' + \mu f_{rep}) e^{j\phi_r}\Big] \Bigg) \Bigg\rangle \Bigg). \tag{C.9}$$

The photocurrent noise $i_{n,opt}(t)$ is given in eq. (6.9) and has contributions from ASE noise and vacuum fluctuations (or shot noise respectively). Beating terms between ASE and shot

noise disappear since the noise sources are not correlated. In the following, the derivation for the shot noise contribution is provided. The calculation steps are identical for the ASE noise case. Because of that, the result for the ASE noise can be simply given by adapting a few relevant factors to the shot noise case. Neglecting ASE noise and using the substitution from eq. (B.1) for the photocurrent shot noise in eq. (6.9) leads in eq. (C.9) to

$$\begin{aligned}
S_{m,2,sh}(f) = \frac{R_\Omega}{4} 4R_p^2 G\eta_{eff} \lim_{T\to\infty} \frac{1}{T} \Bigg(\lim_{f'\to f} \\
\Bigg\langle \Bigg[\Bigg(\mathcal{F}_T\{\big(A(t) * \delta_{T_{rep}}(t)\big) \cdot \mathrm{Re}\{n_{vac}(t)\}\}(f) \cdot \tilde{G}(f) \Bigg) * \\
\Big(\delta(f-\mu f_{rep}) e^{j\phi_r} + \delta(f+\mu f_{rep}) e^{-j\phi_r} \Big) \Bigg] \cdot \\
\Bigg[\Bigg(\mathcal{F}_T^*\{\big(A(t') * \delta_{T_{rep}}(t')\big) \cdot \mathrm{Re}\{n_{vac}(t')\}\}(f') \cdot \tilde{G}^*(f') \Bigg) * \\
\Big(\delta(f'-\mu f_{rep}) e^{-j\phi_r} + \delta(f'+\mu f_{rep}) e^{j\phi_r} \Big) \Bigg] \Bigg\rangle \Bigg) \\
= S_{m,2a,sh}(f) + S_{m,2b,sh}(f) + S_{m,2c,sh}(f) + S_{m,2d,sh}(f) \qquad \text{(C.10)}
\end{aligned}$$

where a real electric field envelope $A(t)$ has been assumed. The 4 terms in eq. (C.10) are

$$\begin{aligned}
S_{m,2a,sh}(f) = & R_\Omega R_p^2 G\eta_{eff} \lim_{T\to\infty} \frac{1}{T} \Bigg(\lim_{f'\to f} \tilde{G}(f-\mu f_{rep}) \tilde{G}^*(f'-\mu f_{rep}) \cdot \\
& \Big\langle \mathcal{F}_T\{\big(A(t) * \delta_{T_{rep}}(t)\big) \cdot \mathrm{Re}\{n_{vac}(t)\}\}(f-\mu f_{rep}) \cdot \\
& \mathcal{F}_T^*\{\big(A(t') * \delta_{T_{rep}}(t')\big) \cdot \mathrm{Re}\{n_{vac}(t')\}\}(f'-\mu f_{rep}) \Big\rangle \Bigg), \qquad \text{(C.11)} \\
S_{m,2b,sh}(f) = & R_\Omega R_p^2 G\eta_{eff} \lim_{T\to\infty} \frac{1}{T} \Bigg(\lim_{f'\to f} \tilde{G}(f-\mu f_{rep}) \tilde{G}^*(f'+\mu f_{rep}) \cdot \\
& \Big\langle \mathcal{F}_T\{\big(A(t) * \delta_{T_{rep}}(t)\big) \cdot \mathrm{Re}\{n_{vac}(t)\}\}(f-\mu f_{rep}) e^{2j\phi_r} \cdot \\
& \mathcal{F}_T^*\{\big(A(t') * \delta_{T_{rep}}(t')\big) \cdot \mathrm{Re}\{n_{vac}(t')\}\}(f'+\mu f_{rep}) \Big\rangle \Bigg), \qquad \text{(C.12)} \\
S_{m,2c,sh}(f) = & R_\Omega R_p^2 G\eta_{eff} \lim_{T\to\infty} \frac{1}{T} \Bigg(\lim_{f'\to f} \tilde{G}(f+\mu f_{rep}) \tilde{G}^*(f'-\mu f_{rep}) \cdot \\
& \Big\langle \mathcal{F}_T\{\big(A(t) * \delta_{T_{rep}}(t)\big) \cdot \mathrm{Re}\{n_{vac}(t)\}\}(f+\mu f_{rep}) e^{-2j\phi_r} \cdot \\
& \mathcal{F}_T^*\{\big(A(t') * \delta_{T_{rep}}(t')\big) \cdot \mathrm{Re}\{n_{vac}(t')\}\}(f'-\mu f_{rep}) \Big\rangle \Bigg), \qquad \text{(C.13)} \\
S_{m,2d,sh}(f) = & R_\Omega R_p^2 G\eta_{eff} \lim_{T\to\infty} \frac{1}{T} \Bigg(\lim_{f'\to f} \tilde{G}(f+\mu f_{rep}) \tilde{G}^*(f'+\mu f_{rep}) \cdot \\
& \Big\langle \mathcal{F}_T\{\big(A(t) * \delta_{T_{rep}}(t)\big) \cdot \mathrm{Re}\{n_{vac}(t)\}\}(f+\mu f_{rep}) \cdot \\
& \mathcal{F}_T^*\{\big(A(t') * \delta_{T_{rep}}(t')\big) \cdot \mathrm{Re}\{n_{vac}(t')\}\}(f'+\mu f_{rep}) \Big\rangle \Bigg). \qquad \text{(C.14)}
\end{aligned}$$

Once again, only the μ-th harmonic remains after the BPF and other harmonics are suppressed. The calculation steps for eqs. (C.11)-(C.14) are very similar. Therefore, a derivation will only be provided for eq. (C.11), while the results for eqs. (C.12)-(C.14) will be given without showing the identical calculations. In the next step, the finite-time Fourier transform definition from eq. (3.16) is applied so that eq. (C.11) can be written as

$$\begin{aligned}
S_{m,2a,sh}(f) =& R_\Omega R_p^2 G \eta_{eff} \lim_{T\to\infty} \frac{1}{T} \Bigg(\lim_{f'\to f} \tilde{G}(f-\mu f_{rep}) \tilde{G}^*(f'-\mu f_{rep}) \cdot \\
& \int_{-\frac{T}{2}}^{\frac{T}{2}} \int_{-\frac{T}{2}}^{\frac{T}{2}} \left[A(t) * \delta_T(t)\right] \left\langle \mathrm{Re}\{n_{vac}(t)\} \, \mathrm{Re}\{n_{vac}(t')\} \right\rangle \cdot \\
& \left[A(t') * \delta_{T_{rep}}(t')\right] e^{-j2\pi(f-\mu f_{rep})t} e^{j2\pi(f'-\mu f_{rep})t'} \mathrm{d}t \mathrm{d}t' \Bigg) \\
=& R_\Omega R_p^2 G \eta_{eff} \frac{h\nu_c}{4} \lim_{T\to\infty} \frac{1}{T} \Bigg(\lim_{f'\to f} \tilde{G}(f-\mu f_{rep}) \tilde{G}^*(f'-\mu f_{rep}) \cdot \\
& \int_{-\frac{T}{2}}^{\frac{T}{2}} \left[|A(t)|^2 * \delta_T(t)\right] e^{-j2\pi(f-f')t} \mathrm{d}t \Bigg).
\end{aligned} \tag{C.15}$$

Once again, the ACF of the real parts of the vacuum fluctuations corresponds to half of the expression in eq. (6.4) since the PSD is equally distributed between the real and imaginary parts [101]. The integral corresponds to the finite-time Fourier transform of the pulse train power envelope PSD $P_{opt,T}(f-f')$ in dependence on the frequency $(f-f')$. Finally, the evaluation of the limes operations leads to

$$S_{m,2a,sh}(f) = R_\Omega R_p^2 G \eta_{eff} \frac{h\nu_c}{4} P_{opt}(0) |\tilde{G}(f-\mu f_{rep})|^2. \tag{C.16}$$

The calculations of the other terms are identical and result in

$$S_{m,2b,sh}(f) = R_\Omega R_p^2 G \eta_{eff} \frac{h\nu_c}{4} P_{opt}(-2\mu f_{rep}) e^{2j\phi_r} \cdot \tilde{G}(f-\mu f_{rep}) \tilde{G}^*(f+\mu f_{rep}), \tag{C.17}$$

$$S_{m,2c,sh}(f) = R_\Omega R_p^2 G \eta_{eff} \frac{h\nu_c}{4} P_{opt}(2\mu f_{rep}) e^{-2j\phi_r} \cdot \tilde{G}(f+\mu f_{rep}) \tilde{G}^*(f-\mu f_{rep}), \tag{C.18}$$

$$S_{m,2d,sh}(f) = R_\Omega R_p^2 G \eta_{eff} \frac{h\nu_c}{4} P_{opt}(0) |\tilde{G}(f+\mu f_{rep})|^2. \tag{C.19}$$

The sum of eqs. (C.16)-(C.19) results in

$$\begin{aligned}
S_{m,2,sh}(f) = & R_\Omega R_p^2 G \eta_{eff} \frac{h\nu_c}{2} P_{opt}(0) |\tilde{G}(\mu f_{rep})|^2 \cdot \\
& \left[1 - \frac{|P_{opt}(2\mu f_{rep})|}{|P_{opt}(0)|} \cos\left(\phi_p(2\mu f_{rep}) - 2\phi_p(\mu f_{rep})\right) \right].
\end{aligned} \tag{C.20}$$

Here, it has been assumed that the demodulated baseband frequency is much smaller than the μ-th measured harmonic $f \ll \mu f_{rep}$ so that $\tilde{G}(f - \mu f_{rep}) \approx \tilde{G}(-\mu f_{rep})$. Moreover, the relations $\cos(\pi + \phi) = -\cos(\phi)$ and $\cos(\phi) = \cos(-\phi)$ have been applied as well as the condition from eq. (C.7) for phase noise measurements. The ASE noise contribution can be derived by identical calculation steps. Regarding the additional factor $\sqrt{\eta_{eff}}$ for the ASE-noise-induced photocurrent noise $i_{n,ASE}(t)$ compared to the shot-noise-induced photocurrent noise $i_{n,vac}(t)$ in eq. (6.9) and the different ACF from eq. (6.1), the result can be directly named as

$$S_{m,2,ASE}(f) = R_\Omega R_p^2 G \eta_{eff} \frac{h\nu_c}{2} P_{opt}(0) |\tilde{G}(\mu f_{rep})|^2 \cdot \eta_{eff}(FG-1) \cdot \left[1 - \frac{|P_{opt}(2\mu f_{rep})|}{|P_{opt}(0)|} \cos\left(\phi_p(2\mu f_{rep}) - 2\phi_p(\mu f_{rep})\right)\right]. \quad \text{(C.21)}$$

Once again, the relation from eq. (6.3) has been applied to replace the inversion factor by the more practical noise figure F. For amplitude noise measurements the phase condition in eq. (C.7) is different what would change the minus sign within the brackets of eqs. (C.20) and (C.21) into a plus sign. For simplification the average optical power $P_{opt}(0) = P_{avg}$ at the MLL output is introduced. Using the notation of the average photocurrent I_{avg} from eq. (6.38) in eqs. (C.20) and (C.21) results into the combined formula

$$S_{m,2}(f) = \frac{q I_{avg} R_\Omega}{2} \cdot (1 + \eta_{eff}(FG-1)) \cdot |\tilde{G}(\mu f_{rep})|^2 \cdot \left[1 \pm \frac{|P_{opt}(2\mu f_{rep})|}{|P_{opt}(0)|} \cos\left(\phi_p(2\mu f_{rep}) - 2\phi_p(\mu f_{rep})\right)\right] \quad \text{(C.22)}$$

where the ideal photodiode impulse response $R_p = q/h\nu_c$ has been used. As mentioned before the plus sign is valid for amplitude measurements, while the minus sign represents phase noise measurements. Note that the notation from [167] has been adapted to prove consistency with the recent publication. The last two terms $S_{m,3}(f)$ and $S_{m,4}(f)$ in eq. (C.1) can be calculated in a similar way. As a result these terms disappear since the ensemble average of the individual noise terms are $\langle \mathrm{Re}\{n_{vac}(t)\}\rangle = \langle \mathrm{Re}\{n_{ASE}(t)\}\rangle = 0$. It is the same argumentation like given in the end of the derivation in appendix B.

The SSB phase noise level is always measured relative to the harmonic power given in eq. (6.40). This results into eq. (6.39).

Acronyms

1D One-Dimensional

2D Two-Dimensional

ADC Analog-To-Digital Converter

ACF Autocorrelation Function

ASE Amplified Spontaneous Emission

BiCMOS Bipolar Complementary Metal-Oxide-Semiconductor

BPF Bandpass Filter

CDN Clock Distribution Network

CMOS Complementary Metal-Oxide-Semiconductor

CNT Carbon Nanotubes

CW Continuous Wave

DAC Digital-To-Analog Converter

DEMUX Demultiplexer

DUT Device Under Test

EDFA Erbium-Doped Fiber Amplifier

ENOB Effective Number Of Bits

ESA Electrical Spectrum Analyzer

FCA Free Carrier Absorption

FCE Free Carrier Effects

FM Frequency Modulation

FWHM Full-Width-Half-Maximum

GVD Group Velocity Dispersion

IC Integrated Circuit

ITRS International Technology Roadmap For Semiconductor

LC Inductance-Capacitance

MLL Mode-Locked Laser

MMI Multimode Interference

MUX Multiplexer

MZI Mach-Zehnder Interferometer

NPE Non-Linear Polarization Evolution

OECC Opto-Electronic Clock Converter

OPM Optical Power Meter

PD Photodetector

PIC Photonic Integrated Circuit

PLL Phase-Locked Loop

PSD Power Spectral Density

RF Radio Frequency

RIN Relative Intensity Noise

RMS Root-Mean-Square

SAR Successive Approximation

SESAM Semiconductor Saturable Absorber

SFDR Spurious-Free Dynamic Range

SNR Signal-To-Noise Ratio

SINAD Signal-To-Noise And Distortion Ratio

SOI Silicon-On-Insulator

SSB Single-Sideband

TE Transverse Electric

TM Transverse Magnetic

TIA Transimpedance Amplifier

TIADC Time-Interleaved Analog-To-Digital Converter

TPA Two-Photon Absorption

VCO Voltage-Controlled Oscillator

VLSI Very-Large-Scale-Integration

VOA Variable Optical Attenuator

List of Figures

List of Tables

Bibliography

[1] J. Hoerni, "Method of manufacturing semiconductor devices," US Patent 3 025 589, 1961.

[2] R. N. Noyce, "Semiconductor device and lead structure," US Patent 2 981 877, 1961.

[3] J. S. Kilby, "Miniaturized electronic circuits," US Patent 3 138 743, 1964.

[4] G. E. Moore, "Cramming more components onto integrated circuits," *Electronics Magazine*, vol. 38, no. 8, pp. 114–117, 1965.

[5] F. Wanlass and C. Sah, "Nanowatt logic using field-effect metal-oxide semiconductor triodes," in *IEEE International Solid-State Circuits Conference. Digest of Technical Papers*, 1963, pp. 32–33.

[6] E. G. Friedman, "Clock distribution networks in synchronous digital integrated circuits," *Proceedings of the IEEE*, vol. 89, no. 5, pp. 665–692, 2001.

[7] S. Tam, *Clocking in modern VLSI systems*. Springer US, 2009.

[8] B. Ackland, B. Razavi, and L. West, "A comparison of electrical and optical clock networks in nanometer technologies," in *IEEE Custom Integrated Circuits Conference*, 2005.

[9] A. V. Mule, E. N. Glytsis, T. K. Gaylord, and J. D. Meindl, "Electrical and optical clock distribution networks for gigascale microprocessors," *IEEE Transactions on VLSI Systems*, vol. 10, no. 5, pp. 582–594, 2002.

[10] H. Xu, V. F. Pavlidis, W. Burleson, and G. De Micheli, "The combined effect of process variations and power supply noise on clock skew and jitter," *13th International Symposium on Quality Electronic Design (ISQED)*, pp. 320–327, 2012.

[11] C. Thangaraj, R. Pownall, P. Nikkel, G. Yuan, K. L. Lear, and T. Chen, "Fully CMOS-compatible on-chip optical clock distribution and recovery," *IEEE Transactions On Very Large Scale Integration VlSI Systems*, vol. 18, no. 10, pp. 1385–1398, 2010.

[12] C. Yeh, G. Wilke, H. Chen, S. Reddy, H. Nguyen, T. Miyoshi, W. Walker, and R. Murgai, "Clock distribution architectures: a comparative study," *7th International Symposium on Quality Electronic Design (ISQED'06)*, pp. 85–91, 2006.

[13] L. Zhang, B. Ciftcioglu, M. Huang, and H. Wu, "Injection-locked clocking: a new GHz clock distribution scheme," *Proceedings of the IEEE Custom Integrated Circuits Conference*, pp. 785–788, 2006.

[14] D. Deleganes, J. Douglas, B. Kommandur, and M. Patyra, "Designing a 3 GHz, 130 nm, Intel Pentium 4 processor," *Symposium on VLSI Circuits Digest of Technical Papers*, pp. 130–133, 2002.

[15] "International technology roadmap for semiconductors," 2001, http://www.itrs2.net/itrs-reports.html.

[16] J. W. Goodman, F. I. Leonberger, S.-Y. Kung, and R. A. Athale, "Optical interconnections for VLSI systems," *Proceedings of the IEEE*, vol. 72, no. 7, pp. 850–866, 1984.

[17] H. A. Haus, "A theory of forced mode locking," *IEEE Journal of Quantum Electronics*, vol. 11, no. 7, pp. 323–330, 1975.

[18] H. A. Haus and A. Mecozzi, "Noise of mode-locked lasers," *IEEE Journal of Quantum Electronics*, vol. 29, no. 3, pp. 983–996, 1993.

[19] D. von der Linde, "Characterization of the noise in countinously operating mode-locked lasers," *Applied Physics B*, vol. 39, no. 4, pp. 201–217, 1986.

[20] R. A. Soref and J. P. Lorenzo, "Single-crystal silicon: a new material for 1.3 and 1.6 μm integrated-optical components," *Electronics Letters*, vol. 21, no. 21, pp. 953–954, 1985.

[21] R. A. Soref, J. Schmidtchen, and K. Petermann, "Large single-mode rib waveguides in GeSi-Si and Si-on-SiO2," *IEEE Journal of Quantum Electronics*, vol. 27, no. 8, pp. 1971–1974, 1991.

[22] D. A. B. Miller, "Optical interconnects to electronic chips," *Applied Optics*, vol. 49, no. 25, pp. F59–F70, 2010.

[23] R. H. Walden, "Analog-to-digital converter survey and analysis," *IEEE Journal on Selected Areas in Communications*, vol. 17, no. 4, pp. 539–550, 1999.

[24] G. C. Valley, "Photonic analog-to-digital converters," *Optics Express*, vol. 15, no. 5, pp. 1955–1982, 2007.

[25] A. Khilo, S. J. Spector, M. E. Grein, A. H. Nejadmalayeri, C. W. Holzwarth, M. Y. Sander, M. S. Dahlem, M. Y. Peng, M. W. Geis, N. A. DiLello, J. U. Yoon, A. Motamedi, J. S. Orcutt, J. P. Wang, C. M. Sorace-Agaskar, M. A. Popović, J. Sun, G.-R. Zhou, H. Byun, J. Chen, J. L. Hoyt, H. I. Smith, R. J. Ram, M. Perrott, T. M. Lyszczarz, E. P. Ippen, and F. X. Kärtner, "Photonic ADC: overcoming the bottleneck of electronic jitter," *Optics Express*, vol. 20, no. 4, pp. 4454–4469, 2012.

[26] B. Jonsson, "A/D-converter performance evolution (1974 - 2012)," ADMS Design AB, 2013, https://converterpassion.wordpress.com/documents/.

[27] L. Kull, T. Toifl, M. Schmatz, P. A. Francese, C. Menolfi, M. Braendli, M. Kossel, T. Morf, T. M. Andersen, and Y. Leblebici, "A 90 GS/s 8b 667 mW 64x interleaved SAR ADC in 32 nm digital SOI CMOS," in *IEEE International Solid-State Circuits Conference Digest of Technical Papers (ISSCC)*, 2014, pp. 378–379.

[28] L. Kull, J. Pliva, T. Toifl, M. Schmatz, P. A. Francese, C. Menolfi, M. Braendli, M. Kossel, T. Morf, T. M. Andersen, and Y. Leblebici, "A 110 mW 6 bit 36 GS/s interleaved SAR ADC for 100 GBE occupying 0.048mm^2 in 32 nm SOI CMOS," in *IEEE Asian Solid-State Circuits Conference (A-SSCC)*, 2014, pp. 89–92.

[29] J. Kim and F. X. Kärtner, "Attosecond-precision ultrafast photonics," *Laser & Photonics Reviews*, vol. 4, no. 3, pp. 432–456, 2010.

[30] M. Y. Peng, P. T. Callahan, A. H. Nejadmalayeri, S. Valente, M. Xin, L. Grüner-Nielsen, E. M. Monberg, M. Yan, J. M. Fini, and F. X. Kärtner, "Long-term stable, sub-femtosecond timing distribution via a 1.2-km polarization-maintaining fiber link: approaching 10^{-21} link stability," *Optics Express*, vol. 21, no. 17, pp. 19 982–19 989, 2013.

[31] L. Kull, J. Pliva, T. Toifl, M. Schmatz, P. A. Francese, C. Menolfi, M. Brändli, M. Kossel, T. Morf, T. M. Andersen, and Y. Leblebici, "Implementation of low-power $6-8$ b $30-90$ GS/s time-interleaved ADCs with optimized input bandwidth in 32 nm CMOS," *IEEE Journal of Solid-State Circuits*, vol. 51, no. 3, pp. 636–648, 2016.

[32] P. W. Juodawlkis, J. C. Twichell, G. E. Betts, J. J. Hargreaves, R. D. Younger, J. L. Wasserman, F. J. O'Donnell, K. G. Ray, and R. C. Williamson, "Optically sampled

analog-to-digital converters," *IEEE Transactions on Microwave Theory and Techniques*, vol. 49, no. 10, pp. 1840–1853, 2001.

[33] J. Kim, M. J. Park, M. H. Perrott, and F. X. Kärtner, "Photonic subsampling analog-to-digital conversion of microwave signals at 40-GHz with higher than 7-ENOB resolution." *Optics Express*, vol. 16, no. 21, pp. 16 509–16 515, 2008.

[34] M. Hasegawa, T. Satoh, T. Nagashima, M. Mendez, and T. Konishi, "Below 100-fs timing jitter seamless operations in 10-GSample/s 3-bit photonic analog-to-digital conversion," *IEEE Photonics Journal*, vol. 7, no. 3, pp. 1–7, 2015.

[35] F. X. Kärtner, A. Khilo, and A. Nejadmalayeri, "Progress in photonic analog-to-digital conversion," *Optical Fiber Communication Conference/National Fiber Optic Engineers Conference 2013*, p. OTh3D.5, 2013.

[36] H. Zmuda, E. N. Toughlian, G. Li, and P. LiKamWa, "A photonic wideband analog-to-digital converter," *IEEE Aerospace Conference Proceedings (Cat. No.01TH8542)*, vol. 3, pp. 3/1461–3/1472, 2001.

[37] R. Urata, R. Takahashi, V. A. Sabnis, D. A. B. Miller, and J. S. Harris, "Ultrafast optoelectronic sample-and-hold using low-temperature-grown GaAs MSM," *IEEE Photonics Technology Letters*, vol. 15, no. 5, pp. 724–726, 2003.

[38] L. Y. Nathawad, R. Urata, B. A. Wooley, and D. A. B. Miller, "A 40-GHz-bandwidth, 4-bit, time-interleaved A/D converter using photoconductive sampling," *IEEE Journal of Solid-State Circuits*, vol. 38, no. 12, pp. 2021–2030, 2003.

[39] B. Krueger, R. E. Makon, O. Landolt, E. Krune, D. Knoll, S. Lischke, and J. Schulze, "A monolithically integrated opto-electronic clock converter in photonic SiGe-BiCMOS technology," in *Proceedings of the IEEE Bipolar/BiCMOS Circuits and Technology Meeting (BCTM)*, 2015, pp. 129–132.

[40] P. Noll, "Signale und Systeme," Vorlesungsskript, Technische Universität Berlin, 2008.

[41] ——, "Quellencodierung," Vorlesungsskript, Technische Universität Berlin, 2008.

[42] F. Maloberti, *Data converters*. Springer, 2007.

[43] C. Azeredo-Leme, "Clock jitter effects on sampling: a tutorial," *IEEE Circuits and Systems Magazine*, vol. 11, no. 3, pp. 26–37, 2011.

[44] M. S. Oude Alink, A. B. J. Kokkeler, E. A. M. Klumperink, K. C. Rovers, G. J. M. Smit, and B. Nauta, "Spurious-free dynamic range of a uniform quantizer," *IEEE Transactions on Circuits and Systems II: Express Briefs*, vol. 56, no. 6, pp. 434–438, 2009.

[45] H. Pan and A. A. Abidi, "Spectral spurs due to quantization in Nyquist ADCs," *IEEE Transactions on Circuits and Systems I: Regular Papers*, vol. 51, no. 8, pp. 1422–1439, 2004.

[46] Y. M. Greshishchev, M. Besson, R. Gibbins, P. Flemke, N. Ben-Hamida, D. Pollex, P. Schvan, and S.-C. Wang, "A 40 GS/s 6 b ADC in 65 nm CMOS," in *IEEE International Solid-State Circuits Conference Digest of Technical Papers (ISSCC)*, 2010, pp. 390–392.

[47] B. Murmann, "ADC performance survey 1997-2015," [Online], 2015, http://web.stanford.edu/~murmann/adcsurvey.html.

[48] B. Razavi, "Problem of timing mismatch in interleaved ADCs," in *Proceedings of the Custom Integrated Circuits Conference*, 2012, pp. 1–8.

[49] U.-K. Moon, K. Mayaram, and J. T. Stonick, "Spectral analysis of time-domain phase jitter measurements," *IEEE Transactions on Circuits and Systems II: Analog and Digital Signal Processing*, vol. 49, no. 5, pp. 321–327, 2002.

[50] B. Razavi, "A study of phase noise in CMOS oscillators," *IEEE Journal of Solid-State Circuits*, vol. 31, no. 3, pp. 331–343, 1996.

[51] A. Hajimiri and T. H. Lee, "A general theory of phase noise in electrical oscillators," *IEEE Journal of Solid-State Circuits*, vol. 33, no. 2, pp. 179–194, 1998.

[52] A. Hajimiri, S. Limotyrakis, and T. H. Lee, "Jitter and phase noise in ring oscillators," *IEEE Journal of Solid-State Circuits*, vol. 34, no. 6, pp. 790–804, 1999.

[53] J. J. Rael and A. A. Abidi, "Physical processes of phase noise in differential LC oscillators," in *Proceedings of the IEEE Custom Integrated Circuits Conference*, 2000, pp. 569–572.

[54] E. Hegazi, H. Sjöland, and A. A. Abidi, "A filtering technique to lower LC oscillator phase noise," *IEEE Journal of Solid-State Circuits*, vol. 36, no. 12, pp. 1921–1930, 2001.

[55] E. Hegazi and A. A. Abidi, "Varactor characteristics, oscillator tuning curves, and AM-FM conversion," *IEEE Journal of Solid-State Circuits*, vol. 38, no. 6, pp. 1033–1039, 2003.

[56] A. A. Abidi, "Phase noise and jitter in CMOS ring oscillators," *IEEE Journal of Solid-State Circuits*, vol. 41, no. 8, pp. 1803–1816, 2006.

[57] D. Murphy, J. J. Rael, and A. A. Abidi, "Phase noise in LC oscillators: a phasor-based analysis of a general result and of loaded Q," *IEEE Transactions on Circuits and Systems I: Regular Papers*, vol. 57, no. 6, pp. 1187–1203, 2010.

[58] M. Moezzi and M. S. Bakhtiar, "Design of LC Resonator for low phase noise oscillators," *IEEE Transactions on Circuits and Systems I: Regular Papers*, vol. 63, no. 2, pp. 169–180, 2016.

[59] D. Ham and A. Hajimiri, "Virtual damping and Einstein relation in oscillators," *IEEE Journal of Solid-State Circuits*, vol. 38, no. 3, pp. 407–418, 2003.

[60] B. E. Jonsson, "On CMOS Scaling and A / D-Converter Performance," in *NORCHIP*, 2010, pp. 1–4.

[61] E. Portuondo-Campa, R. Paschotta, and S. Lecomte, "Sub-100 attosecond timing jitter from low-noise passively mode-locked solid-state laser at telecom wavelength," *Optics Letters*, vol. 38, no. 15, pp. 2650–2653, 2013.

[62] D. Hou, C.-C. Lee, Z. Yang, and T. R. Schibli, "Timing jitter characterization of mode-locked lasers with $< 1\,\mathrm{zs}/\sqrt{\mathrm{Hz}}$ resolution using a simple optical heterodyne technique," *Optics Letters*, vol. 40, no. 13, pp. 2985–2988, 2015.

[63] T. K. Kim, Y. Song, K. Jung, C. Kim, H. Kim, C. H. Nam, and J. Kim, "Sub-100-as timing jitter optical pulse trains from mode-locked Er-fiber lasers," *Optics Letters*, vol. 36, no. 22, pp. 4443–4445, 2011.

[64] Y. Song, C. Kim, K. Jung, H. Kim, and J. Kim, "Timing jitter optimization of mode-locked Yb-fiber lasers toward the attosecond regime," *Optics Express*, vol. 19, no. 15, pp. 14 518–14 525, 2011.

[65] D. Li, U. Demirbas, A. Benedick, A. Sennaroglu, J. Fujimoto, and F. Kärtner, "Attosecond timing jitter pulse trains from semiconductor saturable absorber mode-locked Cr:LiSAF lasers," *Optics Express*, vol. 20, no. 21, pp. 23 422–23 435, 2012.

[66] I. Bronstein, K. Semendjajew, G. Musiol, and H. Mühlig, *Taschenbuch der Mathematik*, 9th ed. Harri Deutsch, 2013.

[67] Maxim Integrated, "Random noise contribution to timing jitter - theory and practice," Tutorial App 3631, pp. 1–15, 2005. [Online]. Available: https://www.maximintegrated.com/en/app-notes/index.mvp/id/3631

[68] R. P. Scott, C. Langrock, and B. Kolner, "High-dynamic-range laser amplitude and phase noise measurement techniques," *IEEE Journal of Selected Topics in Quantum Electronics*, vol. 7, no. 4, pp. 641–655, 2001.

[69] F. Quinlan, T. M. Fortier, H. Jiang, A. Hati, C. Nelson, Y. Fu, J. C. Campbell, and S. A. Diddams, "Exploiting shot noise correlations in the photodetection of ultrashort optical pulse trains," *Nature Photonics*, vol. 7, no. 4, pp. 290–293, 2013.

[70] P. C. A. Roberts, "Understanding phase noise in RF and microwave calibration applications," in *NCSL International Workshop and Symposium*, 2008.

[71] ITU-T Recommendation G.810, "Definitions and terminology for synchronization networks," 08/96.

[72] F. H. Irons and D. M. Hummels, "The modulo time plot - a useful data acquisition diagnostic tool," *IEEE Transactions on Instrumentation and Measurement*, vol. 45, no. 3, pp. 734–738, 1996.

[73] A. Papoulis and S. U. Pillai, *Probability, random variables, and stochastic processes*, 4th ed. McGraw-Hill, 2002.

[74] A. Hati, D. Howe, F. Walls, and D. Walker, "Noise figure vs. PM noise measurements: a study at microwave frequencies," in *Proceedings of the IEEE International Frequency Control Symposium and PDA Exhibition Jointly with the 17th European Frequency and Time Forum*, 2003, pp. 516–520.

[75] W. Wendler, "Phase Noise Measurement up to 50 GHz with High Dynamic Range," Rohde & Schwarz Application Note 1EF68 0E, 2009.

[76] J. Taylor, S. Datta, A. Hati, C. Nelson, F. Quinlan, A. Joshi, and S. Diddams, "Characterization of power-to-phase conversion in high-speed P-I-N photodiodes," *IEEE Photonics Journal*, vol. 3, no. 1, pp. 140–151, 2011.

[77] W. Zhang, T. Li, M. Lours, S. Seidelin, G. Santarelli, and Y. Le Coq, "Amplitude to phase conversion of InGaAs pin photo-diodes for femtosecond lasers microwave signal generation," *Applied Physics B: Lasers and Optics*, vol. 106, no. 2, pp. 301–308, 2012.

[78] T. R. Clark, T. F. Carruthers, P. J. Matthews, and I. N. Duling III, "Phase noise measurements of ultrastable 10 GHz harmonically modelocked fibre laser," *Electronics Letters*, vol. 35, no. 9, pp. 720–721, 1999.

[79] I. Ozdur, M. Akbulut, N. Hoghooghi, D. Mandridis, S. Ozharar, F. Quinlan, and P. J. Delfyett, "A semiconductor-based 10-GHz optical comb source with sub 3-fs shot-noise-limited timing jitter and $\sim$ 500-Hz comb linewidth," *IEEE Photonics Technology Letters*, vol. 22, no. 6, pp. 431–433, 2010.

[80] E. Krune, K. Voigt, L. Zimmermann, and K. Petermann, "Jitter and skew measurements in optical clock distribution networks in silicon photonics," in *IEEE Photonics Conference (IPC)*, 2015, pp. 96–97.

[81] T. R. Schibli, J. Kim, O. Kuzucu, J. T. Gopinath, S. N. Tandon, G. S. Petrich, L. A. Kolodziejski, J. G. Fujimoto, E. P. Ippen, and F. X. Kärtner, "Attosecond active synchronization of passively mode-locked lasers by balanced cross correlation," *Optics Letters*, vol. 28, no. 11, pp. 947–949, 2003.

[82] J. Kim, J. Chen, J. Cox, and F. X. Kärtner, "Attosecond-resolution timing jitter characterization of free-running mode-locked lasers," *Optics Letters*, vol. 32, no. 24, pp. 3519–3521, 2007.

[83] H. Yang, H. Kim, J. Shin, C. Kim, S. Y. Choi, G.-H. Kim, F. Rotermund, and J. Kim, "Gigahertz repetition rate, sub-femtosecond timing jitter optical pulse train directly generated from a mode-locked Yb:KYW laser," *Optics Letters*, vol. 39, no. 1, pp. 56–59, 2014.

[84] C. Kim, K. Jung, K. Kieu, and J. Kim, "Low timing jitter and intensity noise from a soliton Er-fiber laser mode-locked by a fiber taper carbon nanotube saturable absorber," *Optics Express*, vol. 20, no. 28, pp. 29 524–29 530, 2012.

[85] R. A. Soref and B. R. Bennett, "Electrooptical effects in silicon," *IEEE Journal of Quantum Electronics*, vol. 23, no. 1, pp. 123–129, 1987.

[86] C. Gunn, "CMOS photonics for high-speed interconnects," *IEEE Micro*, vol. 26, no. 2, pp. 58–66, 2006.

[87] E. Krune, K. Jamshidi, K. Voigt, L. Zimmermann, and K. Petermann, "Jitter analysis of optical clock distribution networks in silicon photonics," *Journal of Lightwave Technology*, vol. 32, no. 22, pp. 4378–4385, 2014.

[88] E. Krune, B. Krueger, L. Zimmermann, K. Voigt, and K. Petermann, "Comparison of the jitter performance of different photonic sampling techniques," *Journal of Lightwave Technology*, vol. 34, no. 4, pp. 1360–1367, 2016.

[89] M. J. R. Heck, J. F. Bauters, M. L. Davenport, J. K. Doylend, S. Jain, G. Kurczveil, S. Srinivasan, and J. E. Bowers, "Hybrid silicon photonic integrated circuit technology," *IEEE Journal of Selected Topics in Quantum Electronics*, vol. 19, no. 4, p. 6100117, 2013.

[90] Q. Lin, O. J. Painter, and G. P. Agrawal, "Nonlinear optical phenomena in silicon waveguides: modeling and applications," *Optics Express*, vol. 15, no. 25, pp. 16 604–16 644, 2007.

[91] S. Lischke, D. Knoll, C. Mai, L. Zimmermann, A. Peczek, M. Kroh, A. Trusch, E. Krune, K. Voigt, and A. Mai, "High bandwidth, high responsivity waveguide-coupled germanium p-i-n photodiode," *Optics Express*, vol. 23, no. 21, pp. 27 213–27 220, 2015.

[92] X. Sun, J. Liu, L. C. Kimerling, and J. Michel, "Toward a germanium laser for integrated silicon photonics," *IEEE Journal on Selected Topics in Quantum Electronics*, vol. 16, no. 1, pp. 124–131, 2010.

[93] B. Jalali and S. Fathpour, "Silicon photonics," *Journal of Lightwave Technology*, vol. 24, no. 12, pp. 4600–4615, 2006.

[94] D. Liang, G. Roelkens, R. Baets, and J. E. Bowers, "Hybrid integrated platforms for silicon photonics," *Materials*, vol. 3, no. 3, pp. 1782–1802, 2010.

[95] D. Knoll, S. Lischke, R. Barth, L. Zimmermann, B. Heinemann, H. Rücker, C. Mai, M. Kroh, A. Peczek, A. Awny, C. Ulusoy, A. Trusch, A. Krüger, J. Drews, M. Fraschke, D. Schmidt, M. Lisker, K. Voigt, E. Krune, and A. Mai, "High-performance photonic BiCMOS process for the fabrication of high-bandwidth electronic-photonic integrated circuits," in *Technical Digest - International Electron Devices Meeting (IEDM)*, 2015, pp. 15.6.1–15.6.4.

[96] D. Knoll, S. Lischke, A. Awny, M. Kroh, E. Krune, C. Mai, A. Peczek, D. Petousi, S. Simon, K. Voigt, G. Winzer, R. Barth, and L. Zimmermann, "High-performance BiCMOS Si photonics platform," in *Proceedings of the IEEE Bipolar/BiCMOS Circuits and Technology Meeting (BCTM)*, 2015, pp. 88–96.

[97] K. Yamada, *Silicon photonics II: components and integration*. Springer-Verlag, 2011, ch. Silicon photonic wire waveguides: fundamentals and applications, pp. 1–29.

[98] G. Roelkens, D. Vermeulen, S. Selvaraja, R. Halir, W. Bogaerts, and D. Van Thourhout, "Grating-based optical fiber interfaces for silicon-on-insulator photonic integrated circuits," *IEEE Journal of Selected Topics in Quantum Electronics*, vol. 17, no. 3, pp. 571–580, 2011.

[99] S. Lischke, B. Wohlfeil, D. Knoll, L. Zimmermann, C. Mai, Y. Yamamoto, S. Marschmeyer, K. Voigt, and B. Tillack, "High-efficiency grating couplers for integration into a high-performance photonic BiCMOS process," in *Asia Communications and Photonics Conference*, 2013, p. AW4A.1.

[100] W. S. Zaoui, A. Kunze, W. Vogel, M. Berroth, J. Butschke, F. Letzkus, and J. Burghartz, "Bridging the gap between optical fibers and silicon photonic integrated circuits," *Optics Express*, vol. 22, no. 2, pp. 1277–1286, 2014.

[101] K. Petermann, "Einführung in die optische Nachrichtentechnik," Vorlesungsskript, Technische Universität Berlin, 2015.

[102] R. Paschotta, *Encyclopedia for laser physics and technology*, 1st ed. Wiley-VCH, 2008. [Online]. Available: https://www.rp-photonics.com/encyclopedia.html

[103] T. Barwicz and H. A. Haus, "Three-dimensional analysis of scattering losses due to sidewall roughness in microphotonic waveguides," *Journal of Lightwave Technology*, vol. 23, no. 9, pp. 2719–2732, 2005.

[104] R. Sharma, M. W. Puckett, H.-H. Lin, F. Vallini, and Y. Fainman, "Characterizing the effects of free carriers in fully-etched, dielectric-clad silicon waveguides," *Applied Physics Letters*, vol. 106, no. 24, p. 241104, 2015.

[105] G. T. Reed and A. P. Knights, *Silicon photonics: an introduction*. John Wiley & Sons Ltd, 2004.

[106] G. Cocorullo, F. G. Della Corte, and I. Rendina, "Temperature dependence of the thermo-optic coefficient in crystalline silicon between room temperature and 550 K at the wavelength of 1523 nm," *Applied Physics Letters*, vol. 74, no. 22, pp. 3338–3340, 1999.

[107] J. Komma, C. Schwarz, G. Hofmann, D. Heinert, and R. Nawrodt, "Thermo-optic coefficient of silicon at 1550 nm and cryogenic temperatures," *Applied Physics Letters*, vol. 101, no. 4, p. 041905, 2012.

[108] G. Tosik, F. Abramowicz, Z. Lisik, and F. Gaffiot, "Clock skew analysis in optical clock distribution network," in *9th International Conference - The Experience of Designing and Applications of CAD Systems in Microelectronics (CADSM)*, 2007, pp. 422–425.

[109] J. Teng, P. Dumon, W. Bogaerts, H. Zhang, X. Jian, X. Han, M. Zhao, G. Morthier, and R. Baets, "Athermal silicon-on-insulator ring resonators by overlaying a polymer cladding on narrowed waveguides," *Optics Express*, vol. 17, no. 17, pp. 14 627–14 633, 2009.

[110] S. S. Djordjevic, K. Shang, B. Guan, S. T. S. Cheung, L. Liao, J. Basak, H.-F. Liu, and S. J. B. Yoo, "CMOS-compatible, athermal silicon ring modulators clad with titanium dioxide," *Optics Express*, vol. 21, no. 12, pp. 13 958–13 968, 2013.

[111] M. Nedeljkovic, R. Soref, and G. Z. Mashanovich, "Free-carrier electrorefraction and electroabsorption modulation predictions for silicon over the 1-14-μm infrared wavelength range," *IEEE Photonics Journal*, vol. 3, no. 6, pp. 1171–1180, 2011.

[112] A. J. Sabbah and D. M. Riffe, "Femtosecond pump-probe reflectivity study of silicon carrier dynamics," *Physical Review B*, vol. 66, no. 16, p. 165217, 2002.

[113] D. Dimitropoulos, R. Jhaveri, R. Claps, J. C. S. Woo, and B. Jalali, "Lifetime of photogenerated carriers in silicon-on-insulator rib waveguides," *Applied Physics Letters*, vol. 86, no. 7, p. 071115, 2005.

[114] A. C. Turner-Foster, M. A. Foster, J. S. Levy, C. B. Poitras, R. Salem, A. L. Gaeta, and M. Lipson, "Ultrashort free-carrier lifetime in low-loss silicon nanowaveguides," *Optics Express*, vol. 18, no. 4, pp. 3582–3591, 2010.

[115] A. Gajda, L. Zimmermann, J. Bruns, B. Tillack, and K. Petermann, "Design rules for p-i-n diode carriers sweeping in nano-rib waveguides on SOI," *Optics Express*, vol. 19, no. 10, pp. 9915–9922, 2011.

[116] N. M. Wright, D. J. Thomson, K. L. Litvinenko, W. R. Headley, A. J. Smith, A. P. Knights, J. H. B. Deane, F. Y. Gardes, G. Z. Mashanovich, R. Gwilliam, and G. T. Reed, "Free carrier lifetime modification for silicon waveguide based devices," *Optics Express*, vol. 16, no. 24, pp. 19 779–19 784, 2008.

[117] A. R. Motamedi, A. H. Nejadmalayeri, A. Khilo, F. X. Kärtner, and E. P. Ippen, "Ultrafast nonlinear optical studies of silicon nanowaveguides," *Optics Express*, vol. 20, no. 4, pp. 4085–4101, 2012.

[118] J. Müller, "Charakterisierung integriert-optischer Silizium-Wellenleiter," Ph.D. dissertation, Technische Universität Hamburg-Harburg, 2013.

[119] C. Koos, L. Jacome, C. Poulton, J. Leuthold, and W. Freude, "Nonlinear silicon-on-insulator waveguides for all-optical signal processing," *Optics Express*, vol. 15, no. 10, pp. 5976–5990, 2007.

[120] Q. Lin, J. Zhang, G. Piredda, R. W. Boyd, P. M. Fauchet, and G. P. Agrawal, "Dispersion of silicon nonlinearities in the near infrared region," *Applied Physics Letters*, vol. 91, no. 2, p. 021111, 2007.

[121] A. Cowan, G. Rieger, and J. Young, "Nonlinear transmission of $1.5\,\mu$m pulses through single-mode silicon-on-insulator waveguide structures," *Optics Express*, vol. 12, no. 8, pp. 1611–1621, 2004.

[122] L. B. Soldano and E. C. M. Pennings, "Optical multi-mode interference devices based on self-imaging: principles and applications," *Journal of Lightwave Technology*, vol. 13, no. 4, pp. 615–627, 1995.

[123] K. Voigt, L. Zimmermann, G. Winzer, H. Tian, B. Tillack, and K. Petermann, "C-band optical 90° hybrids in silicon nanowaveguide technology," *IEEE Photonics Technology Letters*, vol. 23, no. 23, pp. 1769–1771, 2011.

[124] W. Bogaerts, S. K. Selvaraja, P. Dumon, J. Brouckaert, K. De Vos, D. Van Thourhout, and R. Baets, "Silicon-on-insulator spectral filters fabricated with CMOS technology," *IEEE Journal on Selected Topics in Quantum Electronics*, vol. 16, no. 1, pp. 33–44, 2010.

[125] K. Voigt, L. Zimmermann, G. Winzer, and K. Petermann, "New design approach to MMI-couplers in photonic wire substrates," in *Proceedings ECIO Cambridge*, 2010, pp. 6–9.

[126] A. Samani, M. Chagnon, D. Patel, V. Veerasubramanian, S. Ghosh, M. Osman, Q. Zhong, and D. V. Plant, "A low-voltage 35-GHz silicon photonic modulator-enabled 112-Gb/s transmission system," *IEEE Photonics Journal*, vol. 7, no. 3, p. 7901413, 2015.

[127] L. Yang, H. Chen, and J. Ding, "12.5 Gb/s carrier-injection silicon Mach-Zehnder optical modulator with high optical bandwidth," in *The 9th International Conference on Group IV Photonics (GFP)*, 2012, pp. 129–131.

[128] D. Patel, S. Ghosh, M. Chagnon, A. Samani, V. Veerasubramanian, M. Osman, and D. V. Plant, "Design, analysis, and transmission system performance of a 41 GHz silicon photonic modulator," *Optics Express*, vol. 23, no. 11, pp. 14 263–14 287, 2015.

[129] K. Goi, A. Oka, H. Kusaka, Y. Terada, K. Ogawa, T.-Y. Liow, X. Tu, G.-Q. Lo, and D.-L. Kwong, "Low-loss high-speed silicon IQ modulator for QPSK/DQPSK in C and L bands," *Optics Express*, vol. 22, no. 9, pp. 10 703–10 709, 2014.

[130] M. Webster, P. Gothoskar, V. Patel, D. Piede, S. Anderson, R. Tummidi, D. Adams, C. Appel, P. Metz, S. Sunder, B. Dama, and K. Shastri, "An efficient MOS-capacitor based silicon modulator and CMOS drivers for optical transmitters," in *11th International Conference on Group IV Photonics (GFP)*, 2014, pp. 1–2.

[131] X. Xie, Q. Zhou, E. Norberg, M. Jacob-Mitos, Y. Chen, A. Ramaswamy, G. Fish, J. E. Bowers, J. Campbell, and A. Beling, "Heterogeneously integrated waveguide-coupled photodiodes on SOI with 12 dBm output power at 40 GHz," in *Optical Fiber Communications Conference and Exhibition (OFC)*, 2015, pp. 1–3.

[132] C. Jacoboni, F. Nava, C. Canali, and G. Ottaviani, "Electron drift velocity and diffusivity in germanium," *Physical Review B*, vol. 24, no. 2, pp. 1014–1026, 1981.

[133] W. Sun, F. Quinlan, T. M. Fortier, J.-D. Deschenes, Y. Fu, S. A. Diddams, and J. C. Campbell, "Broadband noise limit in the photodetection of ultralow jitter optical pulses," *Physical Review Letters*, vol. 113, no. 20, p. 203901, 2014.

[134] L. Reggiani, C. Canali, F. Nava, and G. Ottaviani, "Hole drift velocity in germanium," *Physical Review B*, vol. 16, no. 6, pp. 2781–2791, 1977.

[135] M. V. Fischetti, "Monte Carlo simulation of transport in technologically significant semiconductors of the diamond and zinc-blende structures - part I: homogeneous transport," *IEEE Transactions on Electron Devices*, vol. 38, no. 3, pp. 634–649, 1991.

[136] P. J. Delfyett, D. H. Hartman, and S. Z. Ahmad, "Optical clock distribution using a mode-locked semiconductor laser diode system," *Journal Of Lightwave Technology*, vol. 9, no. 12, pp. 1646–1649, 1991.

[137] O. V. Sinkin, R. Holzlöhner, J. Zweck, and C. R. Menyuk, "Optimization of the split-step Fourier method in modeling optical-fiber communications systems," *Journal of Lightwave Technology*, vol. 21, no. 1, pp. 61–68, 2003.

[138] H. F. Taylor, "An optical analog-to-digital converter - design and analysis," *IEEE Journal of Quantum Electronics*, vol. 15, no. 4, pp. 210–216, 1979.

[139] A. J. Metcalf, F. Quinlan, T. M. Fortier, S. A. Diddams, and A. M. Weiner, "Broadly tunable, low timing jitter, high repetition rate optoelectronic comb generator," *Electronics Letters*, vol. 51, no. 20, pp. 1596–1598, 2015.

[140] H. A. Haus, J. G. Fujimoto, and E. P. Ippen, "Structures for additive pulse mode locking," *Journal of the Optical Society of America B*, vol. 8, no. 10, pp. 2068–2076, 1991.

[141] L. Hou, M. Haji, J. Akbar, B. Qiu, and A. C. Bryce, "Low divergence angle and low jitter $40\,\mathrm{GHz}$ AlGaInAs/InP $1.55\,\mu\mathrm{m}$ mode-locked lasers," *Optics Letters*, vol. 36, no. 6, pp. 966–968, 2011.

[142] M. E. Grein, H. A. Haus, Y. Chen, and E. P. Ippen, "Quantum-limited timing jitter in actively modelocked lasers," *IEEE Journal of Quantum Electronics*, vol. 40, no. 10, pp. 1458–1470, 2004.

[143] A. Schlatter, B. Rudin, S. C. Zeller, R. Paschotta, G. J. Spühler, L. Krainer, N. Haverkamp, H. R. Telle, and U. Keller, "Nearly quantum-noise-limited timing jitter from miniature Er:Yb:glass lasers," *Optics Letters*, vol. 30, no. 12, pp. 1536–1538, 2005.

[144] R. Paschotta, "Timing jitter and phase noise of mode-locked fiber lasers," *Optics Express*, vol. 18, no. 5, pp. 5041–5054, 2010.

[145] F. Rana, H. L. T. Lee, R. J. Ram, M. E. Grein, L. A. Jiang, E. P. Ippen, and H. A. Haus, "Characterization of the noise and correlations in harmonically mode-locked lasers," *Journal of the Optical Society of America B*, vol. 19, no. 11, pp. 2609–2621, 2002.

[146] L. A. Jiang, M. E. Grein, H. Haus, and E. P. Ippen, "Noise of mode-locked semiconductor lasers," *IEEE Journal on Selected Topics in Quantum Electronics*, vol. 7, no. 2, pp. 159–167, 2001.

[147] D. Arsenijević, M. Kleinert, and D. Bimberg, "Phase noise and jitter reduction by optical feedback on passively mode-locked quantum-dot lasers," *Applied Physics Letters*, vol. 103, no. 231101, pp. 1–4, 2013.

[148] R. Paschotta, "Noise of mode-locked lasers (part I): numerical model," *Applied Physics B - Lasers and Optics*, vol. 79, no. 2, pp. 153–162, 2004.

[149] ——, "Noise of mode-locked lasers (part II): timing jitter and other fluctuations," *Applied Physics B - Lasers and Optics*, vol. 79, no. 2, pp. 163–173, 2004.

[150] A. Haboucha, W. Zhang, T. Li, M. Lours, A. N. Luiten, Y. Le Coq, and G. Santarelli, "Optical-fiber pulse rate multiplier for ultralow phase-noise signal generation," *Optics Letters*, vol. 36, no. 18, pp. 3654–3656, 2011.

[151] S. A. Diddams, M. Kirchner, T. Fortier, D. Braje, A. M. Weiner, and L. Hollberg, "Improved signal-to-noise ratio of 10 GHz microwave signals generated with a mode-filtered femtosecond laser frequency comb," *Optics Express*, vol. 17, no. 5, pp. 3331–3340, 2009.

[152] J. Azaña and M. A. Muriel, "Temporal self-imaging effects: theory and application for multiplying pulse repetition rates," *IEEE Journal on Selected Topics in Quantum Electronics*, vol. 7, no. 4, pp. 728–744, 2001.

[153] R. Maram, L. Cortes, and J. Azaña, "Programmable fiber-optics pulse repetition-rate multiplier," *IEEE/OSA Journal of Lightwave Technology*, vol. 34, no. 2, pp. 448–455, 2016.

[154] D. Pudo and L. Chen, "Simple estimation of pulse amplitude noise and timing jitter evolution through the temporal Talbot effect," *Optics Express*, vol. 15, no. 10, pp. 6351–6357, 2007.

[155] M. A. Preciado and M. A. Muriel, "All-pass optical structures for repetition rate multiplication," *Optics Express*, vol. 16, no. 15, pp. 11 162–11 168, 2008.

[156] M. Pu, H. Ji, L. H. Frandsen, M. Galili, L. K. Oxenløwe, and J. M. Hvam, "High-Q microring resonator with narrow free spectral range for pulse repetition rate multiplication," in *Conference on Lasers and Electro-Optics (CLEO)*, 2009, p. CThBB7.

[157] Y. Borokhovych, H. Gustat, and C. Scheytt, "4-bit, 16 GS/s ADC with new parallel reference network," in *IEEE International Conference on Microwaves, Communications, Antennas and Electronics Systems (COMCAS)*, 2009.

[158] P. W. Juodawlkis, J. C. Twichell, J. L. Wasserman, G. E. Betts, and R. C. Williamson, "Measurement of mode-locked laser timing jitter by use of phase-encoded optical sampling," *Optics Letters*, vol. 26, no. 5, pp. 289–291, 2001.

[159] B. Krueger, R. E. Makon, O. Landolt, O. Hidri, T. Schweiger, E. Krune, D. Knoll, S. Lischke, and J. Schulze, "A monolithically integrated, optically clocked 10 GS/s sampler with a bandwidth of > 30 GHz and jitter of < 30 fs in photonic SiGe BiCMOS technology," in *IEEE Custom Integrated Circuits Conference (CICC)*, 2017.

[160] K. Jamshidi, E. Krune, K. Voigt, K. Petermann, and L. Zimmermann, "Timing jitter of optical clock distribution induced by photodetection," in *IEEE Optical Interconnects Conference*, 2013, pp. 84–85.

[161] G. P. Agrawal, *Lightwave technology: Telecommunication systems*. Wiley, 2005.

[162] J. P. Gordon and H. A. Haus, "Random walk of coherently amplified solitons in optical fiber transmission," *Optics Letters*, vol. 11, no. 10, pp. 665–667, 1986.

[163] V. S. Grigoryan, C. R. Menyuk, and R.-M. Mu, "Calculation of timing and amplitude jitter in dispersion-managed optical fiber communications using linearization," *Journal of Lightwave Technology*, vol. 17, no. 8, pp. 1347–1356, 1999.

[164] S. C. Terry, B. J. Blalock, J. M. Rochelle, M. N. Ericson, and S. D. Caylor, "Time-domain noise analysis of linear time-invariant and linear time-variant systems using MATLAB and HSPICE," *IEEE Transactions on Nuclear Science*, vol. 52, no. 3, pp. 805–812, 2005.

[165] B. E. A. Saleh and M. C. Teich, *Fundamentals of photonics*, 2nd ed. Wiley Series in Applied Optics, 2007.

[166] V. Giovannetti, S. Lloyd, and L. Maccone, "Quantum-enhanced positioning and clock synchronization," *Nature*, vol. 412, pp. 417–419, 2001.

[167] F. Quinlan, T. M. Fortier, H. Jiang, and S. A. Diddams, "Analysis of shot noise in the detection of ultrashort optical pulse trains," *Journal of the Optical Society of America B*, vol. 30, no. 6, pp. 1775–1785, 2013.

[168] J.-D. Deschênes, "Non-stationary photodetection shot noise in frequency combs : a signal processing perspective," Ph.D. dissertation, Université Laval, 2014.

[169] D.-X. Xu, P. Cheben, D. Dalacu, A. Delâge, S. Janz, B. Lamontagne, M.-J. Picard, and W. N. Ye, "Eliminating the birefringence in silicon-on-insulator ridge waveg-

uides by use of cladding stress," *Optics Letters*, vol. 29, no. 20, pp. 2384–2386, 2004.

[170] M. Huang and X. Yan, "Thermal-stress effects on the temperature sensitivity of optical waveguides," *Journal of the Optical Society of America B*, vol. 20, no. 6, pp. 1326–1333, 2003.

[171] O. Landolt, "Electronic circuit for optical control of a flip-flop," US Patent 13/807,821, 2013.

[172] J. Breitbarth and J. Koebel, "Additive (residual) phase noise measurement of amplifiers, frequency dividers and frequency multipliers," *Microwave Journal*, vol. 51, no. 6, pp. 66–82, 2008.